Nuclear Magnetic Resonance Relaxometry and Diffusometry Study of Bulk and Confined Complex Liquids

Dissertation

zur Erlangung des akademischen Grades
Doctor rerum naturalium (Dr. rer. nat.)

von

M.Sc. Amin Ordikhani-Seyedlar

1. Gutachter: Prof. Dr. rer. nat. habil. S. Stapf
2. Gutachter: Prof. Dr. rer. nat. habil. Dr. h.c. A. Bund
3. Gutachter: Prof. Dr. M. Schönhoff

Tag der Einreichung der Dissertation: 19.01.2016
Tag der wissenschaftlichen Aussprache:
- nichtöffentlicher Teil (Rigorosum) : 20.04.2016
- öffentlicher Teil (Verteidigung) : 27.04.2016

urn:nbn:de:gbv:ilm1-2016000207

Abstract

The nuclear magnetic resonance (NMR) was used as a core method to tackle the molecular dynamic problems of complex liquids: ionic liquids and crude oil compounds. The NMR relaxation studies at the large range of magnetic field strengths covering from the proton Larmor frequency of ~10 kHz to 300 MHz enable the identification of dynamics of molecules at a large timescale. Thermal and NMR studies of five ionic liquids were considered in this investigation: Emim Tf2N and Bmim Tf2N; Emim Br, Bmim Br, and Hmim Br. The focus has been on the supercooled temperature regimes where the motion of ions become slower. The nano-meter geometrical restriction effects were studied by preparing Bmim Tf2N inside a porous glass of 4 nm pore-size. A comparative study of crude oils were done to identify and determine the maltene-asphaltene interactions.

Differential scanning calorimetry method provided the supercooled temperature regimes for each ionic liquid. The frequency dependent T_1 relaxation times were measured at supercooled temperatures for bulk ionic liquids. A relaxation model assuming rotational and translational dynamics for the ions was employed and the corresponding correlation times were quantified. Different fitting procedures based on the relaxation model were considered and the outcome of each procedure was discussed. The temperature dependence of translational dynamics showed generally non-Arrhenius behaviours while the rotational dynamics followed Arrhenius trends for the measured temperature ranges. Independent pulsed field gradient NMR self-diffusion measurements confirmed the relaxation model. A unique property was observed for the ionic liquids approaching their glass transition temperatures that the temperature dependence trends were deviated at a certain temperature around $1.2\,T_\mathrm{g}$. This temperature was identified as the crossover temperature T_c which had been reported to be a unique feature of glass forming molecular liquids. The observation of such a transition for some of the ionic liquids in this study has not been reported to date. Furthermore, degrees of cooperativity of the ionic translational motions were quantified from the frequency dependent relaxation studies.

The T_1 frequency dependent measurements of the confined ionic liquid, Bmim Tf2N, in nano-porous glass were analysed by considering the dynamics of the bulk ionic liquid obtained previously. Several molecular dynamics mechanisms were considered for the molecules on the pore surface in the frame of the RMTD (Reorientations Mediated by Translational Displacements) mechanism. The long-range surface displacement mechanism was found to be the main reason of the power law ($\sim \nu^{0.6}$) T_1 relaxation dispersion between 0.1 MHz and 10 MHz of proton Larmor frequency. Similar dynamics were observed for the cation and anion of the ionic liquid in the bound phase.

The interaction of asphaltene – present in heavy crude oils – with the maltene molecules was investigated by introducing small concentrations of fluorinated aromatic and aliphatic molecules. The interaction strength and timescale could be revealed by studying the ^{19}F-T_1 and -T_2 relaxation times of the tracer molecules and by comparing the T_1/T_2 ratios. Asphaltene solutions with varying concentration were also prepared and the concentration dependent studies were carried out. It was found that the T_1/T_2 ratios of the aromatic tracers were largely affected by the presence of asphaltene and the ratio followed a linear dependence with the asphaltene concentration. Different relaxation mechanisms are discussed in this respect. The application of this method could be an alternative and sensitive method for the determination of the heavy fractions of crude oils in industrial sections.

Kurzfassung

Mittels Kernspinresonanz (NMR) als grundlegender Messmethode wurden molekulardynamische Fragestellungen für zwei komplexe, flüssige Systeme untersucht: Ionische Flüssigkeiten und Rohölproben. Ein Schwerpunk lag hierbei auf der Untersuchung von Kernspin-Relaxationsprozessen über einen breiten Bereich magnetischer Feldstärken, welcher Kernspin-Larmorfrequenzen von etwa 10 kHz bis 300 MHz abdeckt. Dies ermöglicht Aussagen über molekulardynamische Prozesse über eine große Spanne verschiedener Zeitskalen. Für fünf ionische Flüssigkeiten wurden außerdem NMR- mit kalorimetrischen Messungen kombiniert: Emim Tf2N und Bmim Tf2N, Emim Br, Bmim Br und Hmim Br. Hierbei lag das Hauptaugenmerk auf einem Temperaturbereich, bei dem ein unterkühlter Zustand mit deutlich verringerter Ionenmobilität vorliegt. Darüber hinaus wurden für Bmim Tf2N Effekte nanoskaliger, geometrischer Begrenzungen in porösem Glas mit 4 nm Porengröße untersucht. Weiterhin wurden auf Grundlage einer vergleichenden Studie mit mehreren Rohölproben Malten-Asphalten-Wechselwirkungen untersucht.

Für jede ionische Flüssigkeit wurde der Temperaturbereich, bei dem ein unterkühlter Zustand vorliegt, mittels dynamische Differenzkalorimetrie (DSC) bestimmt. In diesem Temperaturbereich wurde daraufhin die Frequenzabhängigkeit der T_1-Relaxationszeiten für alle ionische Flüssigkeiten ohne Begrenzungen (Bulk-Proben) gemessen. Ein Relaxationsmodell, welches Beiträge von Rotations- und Translationsdynamik beinhaltet, wurde an die Daten angepasst und daraus entsprechende Korrelationszeiten bestimmt. Hierbei wurden verschiedene Regressionsmethoden getestet und bewertet. Während die Temperaturabhängigkeit der Translationsdynamik kein Arrhenius-Verhalten zeigte, konnte die Temperaturabhängigkeit der Rotationsdynamik im untersuchten Bereich mit einem Arrhenius-Modell beschrieben werden. Gesonderte Selbstdiffusionsmessungen mittels Feldgradienten-NMR konnten die Ergebnisse der Relaxationsmessungen bestätigten. In der Nähe der Glasüber-gangs-Temperatur wurde eine Abweichung der Temperaturabhängigkeit der Translationsdynamik vom Arrhenius-Modell beobachtet. Dieses Phänomen, welches ab einer Übergangstemperatur T_c von etwa $1,2\,T_\mathrm{g}$ auftritt, ist eine besondere Eigenschaft glasformender Flüssigkeiten und ist von anderen Systemen bekannt. Für ionische Flüssigkeiten jedoch wurde ein solches Verhalten bisher nicht beschrieben. Mit Hilfe der frequenzabhängigen Relaxationsmessungen wurde außerdem der Grad der Kooperativität ionischer Translationsbewegungen bestimmt.

Auf Grundlage der für Bulk-Proben gewonnenen Ergebnisse wurden frequenzabhängige T_1-Messungen an ionischen Flüssigkeiten in nanoporösen Gläsern interpretiert und verglichen. Für die Molekulardynamik in der Nähe der Porenoberfläche wurden, basierend auf dem RMTD-Mechanismus (Reorientations mediated by Translational Displacements), verschiedene Modelle betrachtet. Die gemessene T_1-Relaxationsdispersion, welche im Bereich von 0,1 MHz bis 10 MHz einem Potenzgesetz ($\propto \nu^{0,6}$) folgt, konnte unter Berücksichtigung langreichweitiger Bewegungsprozesse entlang der Porenoberfläche interpretiert werden. Für Kationen und Anionen wurden dabei ähnliche molekulardynamische Eigenschaften beobachtet.

In Rohölproben wurde die Wechselwirkung zwischen Malten- und Asphalten-Molekülen mit Hilfe von fluorierten aromatischen und aliphatischen Tracermolekülen untersucht. Die Stärke und Zeitskala dieser Wechselwirkungen konnte mit Hilfe von T_1- und T_2-Relaxationsmessungen an ^{19}F-Kernspins, sowie dem Verhältnis T_1/T_2 bestimmt werden. Außerdem wurden konzentrationsabhängige ^{19}F-Relaxationsmessungen an Asphalten-Lösungen mit den entsprechenden Tracermolekülen durchgeführt. Es konnte gezeigt werden, dass das Verhältnis T_1/T_2 stark durch die Wechselwirkungen mit Asphalten beeinflusst wird und proportional zur Asphalten-Konzentration ist. In diesem Zusammenhang wurden verschiedene Relaxationsmechanismen diskutiert. Im Rahmen einer industriellen Anwendung können diese Ergebnisse die Grundlage für eine alternative, empfindliche Methode zur Quantifizierung der Schwerfraktionen in Rohöl sein.

Contents

List of Figures

List of Tables

Glossary

T_c	Crossover temperature.
T_g	Glass transition temperature.
T_m	Melting temperature.
T_1	Longitudinal or spin-lattice relaxation time.
T_2	Transverse or spin-spin relaxation time.
Bmim	1-Butyl-3-methylimidazolium.
BPP	Bloembergen–Purcell–Pound.
CPMG	Car-Purcell-Meiboom-Gill.
DSC	Differential Scanning Calorimetry.
Emim	1-Ethyl-3-methylimidazolium.
EPR	Electron Paramagnetic Resonance.
FFC	Fast Field-Cycling.
Hmim	1-Hexyl-3-methylimidazolium.
IL	Ionic Liquid.
MSD	Mean Square Displacement.
NE	Nernst-Einstein.
NMR	Nuclear Magnetic Resonance.
PFG	Pulsed Field Gradient.
RMTD	Reorientations Mediated by Translational Displacement.
RTIL	Room Temperature Ionic Liquid.
SARA	Saturate, Aromatic, Resin and Asphaltene.
STE	Stimulated Echo.

Tf2N	Bis(trifluoromethylsulphonyl) imide.
VFT	Vogel-Fulcher-Tammann.
VO-78	Violanthrone-78.

Chapter 1

Introduction

1.1 Motivation

The introduction of new classes of materials into the application fields is possible through well understanding of their physicochemical properties. The potential applications of ionic liquids ignited the research on this field from the beginning of the current century. Ionic liquids were successfully used as extraction solvents in the organic synthesis and probably the most important properties to consider in this case would be to regulate their solubility, reactivity, and reproducibility. On the other hand, for applications where the molecular dynamics and transport properties play a key role, one would expect a deeper understanding of the dynamics of ions in the molecular level. Of many of such applications, the main motivating application in mind was the electrochemical storage and conversion devices. The molecular dynamics and transport properties of ions in this case define the ionic motions/interactions and therefore, ionic conductivity. It is clear that ionic liquids in the pure liquid form are not directly applicable to the energy storage devices and some ions, e.g. alkali metals, should be included in the matrix. However, the molecular dynamics of the neat ionic liquids are yet not completely comprehended especially at the supercooled temperature regime. More knowledge of dynamics of ions at the molecular scale will furnish the road towards the electrochemical devices operable efficiently at much lower temperatures than the ambient conditions. To this aim, the molecular dynamics of bulk ionic liquids are investigated at supercooled temperature region down to near the glass transition temperature. Since the ionic liquids for electrochemical device applications are usually involved in some matrix structures, the confinement effect on the dynamics of ionic liquids was investigated by confining an ionic liquid inside a nano-meter scaled porous glass. The low-field nuclear magnetic resonance (NMR) provides a reasonable tool to investigate the dynamics of molecules with slow tumbling rates while the high-field NMR methods reveal faster motions of molecules. A combination of these methods provides a wide spectral density information for the molecule.

The second subtopic of this thesis has a focus on a long standing challenge in the crude oil industry. The heavy crude oils contain large amounts of polycyclic macromolecules in general known as asphaltene. The asphaltene deposition around the well bores, flow lines, separator pumps and etc. has been threatening the oil industries economically. The need to predict the concentration of asphaltene in crude oils at the extraction site rises the motivation of this study. An effort has been made to develop an analytical method to predict the asphaltene concentration by observing its interaction mechanism with the fluorine labelled maltene solutions by means of NMR. This project has been done in collaboration with the Schlumberger-Doll Research.

1.2 Ionic Liquids

Ionic liquids (ILs) are a class of salts with very low melting temperatures. The first modern physicochemical study of ILs was done in 1924 by Paul Walden where he studied the viscosity dependence of ionic conductivity of ethylammonium nitrate. The developments in the field of ionic liquids remained mainly empirical thereafter and the physics behind remained unknown. It was only in the recent decade that physicochemical investigations on this class of molten salts started which was mainly due to their interesting and unusual properties compared with molecular liquids.

Room temperature ionic liquids (RTILs) are nonvolatile, thermally stable, and flame retardant. As it is clear from the name, ionic liquids are composed of solely ions. So they have high ion density and hence, high ionic conductivity[1]. The room temperature or better to say the ambient temperature in this case means that the melting point is not too much higher than the glass transition temperature, T_g, which brings the natural base for the liquid-like behaviour[1]. Ionic liquids generally melt within the range that it is referred to as the low-temperature regime[2–4]. Room temperature ionic liquids are usually composed of an organic cation and inorganic or organic anion. This makes their structure easily designable while different kinds of ions can form various ionic liquids. There are unlimited possibilities for the preparation of ionic liquids by just varying the organic structure of the compounds. Ionic liquids show completely different properties compared to the ordinary molecular liquids. Interestingly, every ionic liquid shows distinct properties compared to even structurally similar ionic liquids. It is important to have a good understanding of the physicochemical properties of these multi-purpose materials. Probably the most successful industrial application of ILs so far is in the BASIL (Biphasic Acid Scavenging utilizing Ionic Liquids) process which is used by BASF commercially[5]. The methyl imidazolium is used in this reaction as a replacement of the formerly used triethylamine to scavenge the acid formed in the production of alkoxy-phenylphosphine, Fig. 1.1. The reaction product of triethylamine with HCl is aqueous and difficult to separate from the main product while the formed IL in this process is separated as a discrete phase.

One of the main applications of ionic liquids is in electrochemistry. Although the water-based electrolytes might be the best electrochemical solutions, the volatility of water limits its application range. An alternative for the water-based electrolytes, which is not volatile, is polymer electrolytes. Polymers, in comparison, do not vaporize. On the other hand, they decompose at higher temperatures. Although the polymer electrolytes are considered as a top class electrolytes, their low ionic con-

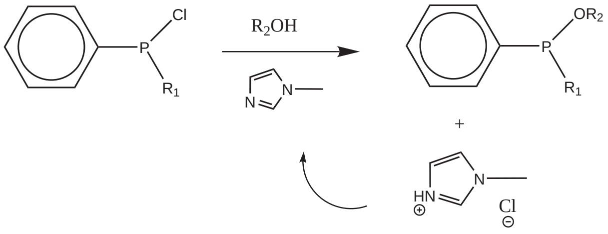

Figure 1.1: Acid scavenging in the alkoxy-phenylphosphine production making use of the phase separation of the ionic liquid in the aqueous solution, known as BASIL reaction.

ductivity has been the main drawback. Ionic liquids being almost nonvolatile at a wide temperature range, they are good proton conductors at temperatures higher than 100 °C where the water-based electrolytes fail to operate due to evaporation. Therefore, the nonvolatility and ionic conductivity are the essential properties for ILs' application in electrolyte solution in safe energy storage systems for the outdoor use. However since ILs are composed of organic compounds, their degradation starts at the weakest covalent bond by heating. Nevertheless, ionic liquids are stable enough for ordinary usage until temperatures around 200 °C to 300 °C[1]. On the other hand, the high stability may bring some issues for their decomposition when their role is finished. Since ionic liquids are designable, it is not difficult to manipulate novel ionic liquids that can be decomposed at a certain temperature or by a certain trigger.

Ionic liquids, as organic solvents, can be categorized as polar/nonpolar or protic/aprotic solvents. The polarity of a molecule depends on the electronegativity of its atoms and their spatial orientation relative to each other. However, being protic or aprotic depends on the ability of molecule to exchange protons. Protic ionic liquids are usually formed by a proton transfer from a Brønsted acid to a Brønsted base, e.g. ethylammonium nitrate and pyridinium chloride. The ionicity of these ILs can be adjusted by altering the driving forces for the proton transfer process. Aprotic ionic liquids, however, are not synthesized by a simple acid-base reaction and do not contain exchangeable protons[6]. Aprotic ILs are usually charge compensated by anions with oxidic character. Examples of this class are alkyl pyridinium and dialkylimidazolium cations. Some of the most common ionic liquids of this class are shown in Fig. 1.2.

The structure of ionic liquids is highly dominated by strong and long-ranged ion-ion interactions. This makes ionic liquids to be considered as structured liquids in some cases[7]. To compare ILs with inorganic salts: Alkali halides, as an example of fused salts, retain their solid structure after melting and only the cation-anion distances increase due to decrease of the coordination number from 6 to about 4[7]. In such a case, the configuration of the molten salt is much similar to the solid structure but with higher population of defects and voids. Although ILs are composed of much larger ions, radial distribution function simulations showed that they still show the charge ordering structure similar to fused salts with small ions[8,9]. Molecular dynamics simulations showed some long lived local structures, yet no clear pairing has

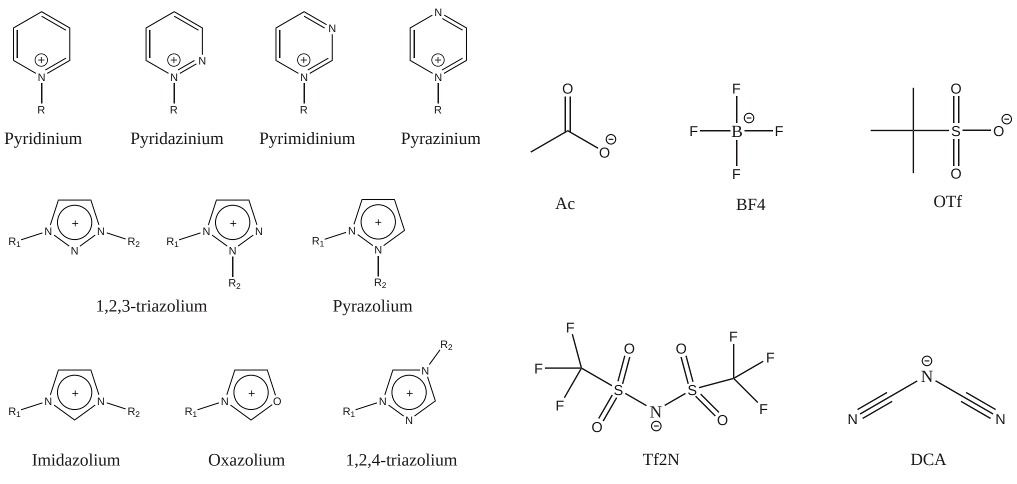

(a) (b)

Figure 1.2: Most common cations and anions of aprotic ionic liquids.

been observed[10]. Cations remain associated on roughly equal terms with multiple anions and vice versa. The dynamics of ILs was found to be dominated by collective motions[11–13] and the aliphatic chains of cations are responsible for the low polarity domain which can be responsible for the structural inhomogeneity on microscopic length scales[7].

The extended liquid-state behaviour is an important feature of ionic liquids. This necessitates the understanding of different liquid properties at varying temperatures. It is important to bear in mind that ionic liquids are single-component systems in which the cations and anions may play different and independent roles in determining the liquid behaviour[14]. The microscopic properties of some selected ILs have been investigated recently using optical and dielectric spectroscopy[15], multidimensional NMR spectroscopy[16], high-field NMR relaxometery[17,18], and other technique[19–21]. However, few investigations were carried out on ILs in supercooled states. Nevertheless, a common theoretical description is not fully available in part because of the asymmetric charge distribution in the molecular ions that determines the electrostatic interaction potential and coulomb forces. ILs are in their majority glass-forming systems[22,23]. A fundamental question is how the structure and molecular dynamics of this kind of solvents will be affected when they are supercooled. Close to the glass transition temperature they exhibit a non-exponential structural relaxation due to the collective nature of their dynamics. The characteristic relaxation times often have non-Arrhenius temperature dependences[24,25]. This departure from the Arrhenius behaviour is found for most of the glass forming systems in properties like diffusivity and viscosity[14,15,26].

Obtaining quantitative molecular dynamic information from NMR relaxation experiments is feasible by understanding the relationship between NMR relaxation times and spectral densities of the motion. To this aim, several ionic liquids composed of different cations (Emim, Bmim, Hmim) and anions (Tf2N and Br) will be studied by NMR relaxometry and diffusometry at varying temperatures. The choice of cations is to consider the effect of imidazolium based cationic molecule with increasing alkyl chain. The anions' selection was to consider the effect of different polarizability and symmetry. At last, the dynamics of a selected ionic liquid will be investigated under nano-porous confinement at varying temperatures.

1.3 Crude Oils

Crude oil is an example of complex fluids and generally consists of mixtures of different hydrocarbons and heavy organics. A large fraction of these compounds consists of linear or almost linear alkanes. Since the molecular composition of a fluid determines its properties such as viscosity and phase behaviour, the successful recovery of useful organic products from the crude oil necessitates understanding its physicochemical properties. Oils from different geographic regions consist of various quantities of organic compounds such as asphaltenes, asphaltogenic acids, diamondoids, mercaptans, organometallics, paraffine/wax, and resins[27,28]. Some of these compounds are shown in Fig. 1.3 . These compounds may separate from the crude oil solution via different mechanisms due to variations in temperature, pressure, composition, pH, flow regime, wall effect, and electrokinetic phenomena. Heavy organic molecules in the oil bring complexities to the petroleum industries due to their untimely depositions that cause arterial blockage in wells or pipelines of the processing facilities. Asphaltenes are highly polar compounds and generally act as glue and mortar in hardening the deposits[29]. When several heavy organics exist in the oil their interactions and therefore collective deposition mechanisms also play a role. In this respect, the determination of composition of heavy organics in the oil turns out to be very important. The molecular weight of asphaltenes can be determined by several techniques such as vapour pressure osmometry, mass spectroscopy, and gel permeation chromatography[30]. Asphaltenes form small aggregates of several molecules under reservoir conditions which can be detected by X-ray and neutron scattering techniques[31–33]. However, all methods are influenced by the analysis conditions, e.g. temperature and asphaltene concentration. In general, no method has proven to give absolute molecular weight information of asphaltenes.

The large variety of heavy organic compounds with complex structures add to the difficulty of identification of the heavy fraction in the crude oil. The characterization methods rely on solubility and different chromatographic techniques. The SARA procedure separates the oil to four classes of compounds: Saturates, aromatics, resins, and asphaltenes[35]. The saturate fraction includes paraffins and diamondoids that is a viscous whitish translucent liquid. This is the only fraction which is easily distinguishable after the separation from the rest of the oil. The aromatic fraction is a reddish viscous liquid composed of aromatic hydrocarbons with different degrees of condensation, alkyl-substitutions, and heteroatoms of sulphur, oxygen, and nitrogen, Fig. 1.3. This fraction covers a continues range of polarity and molecular weight. The resin fraction is a dark brown thick viscous liquid to semi-solid with a higher degree of condensation and heteroatom content than aromatics. The asphal-

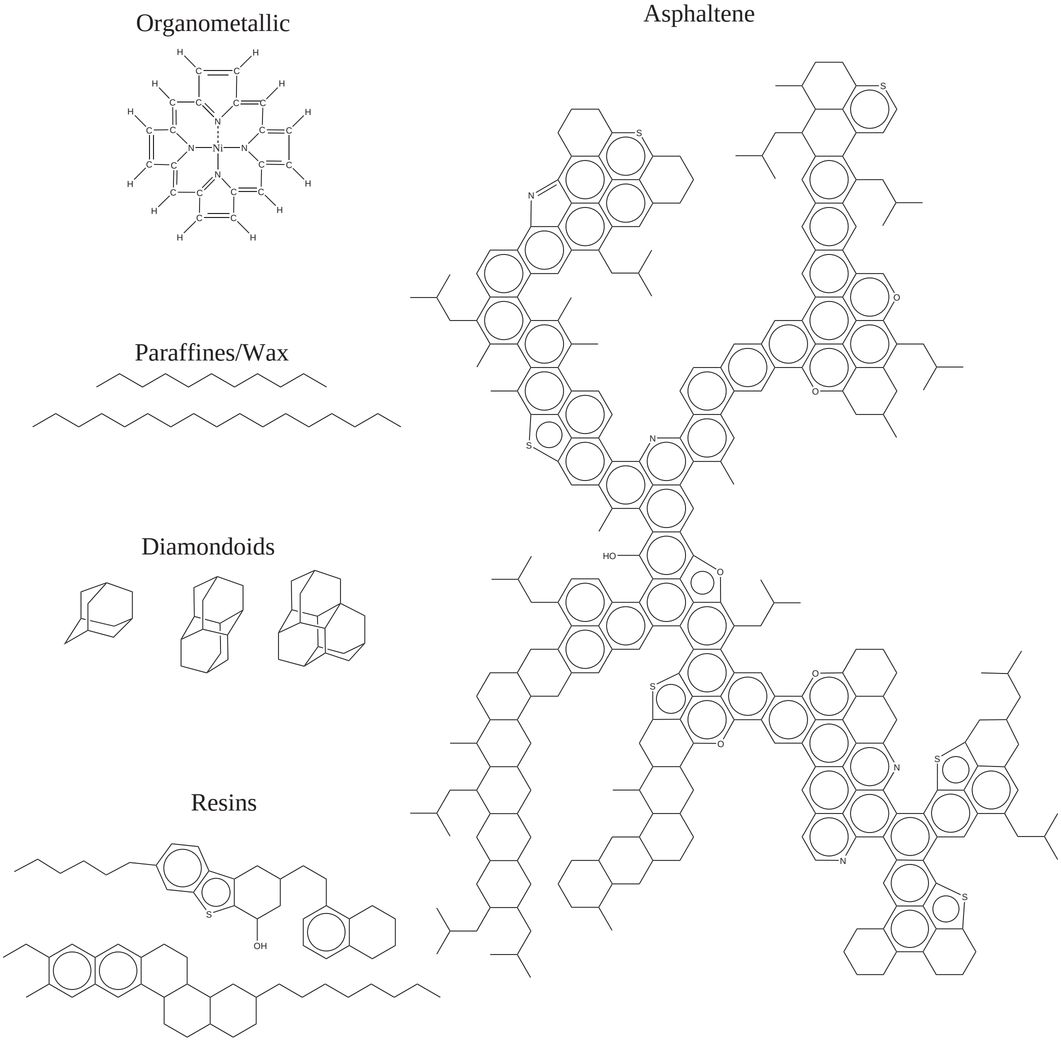

Organometallic

Asphaltene

Paraffines/Wax

Diamondoids

Resins

Figure 1.3: Chemical compounds and their structures generally present in crude oils.

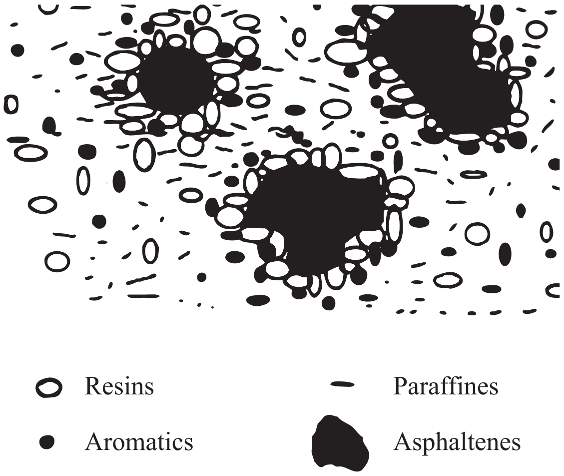

Figure 1.4: A model representing the composition of crude oils where the peptization of asphaltenes by resins is shown[34].

tene fraction is a dark brown to black amorphous solid. Resins and asphaltenes are structurally similar, but asphaltenes are formed by more complex polymeric structures with a large variety of repeating blocks. The heavy organics in the oil are largely polydisperse and usually overlap between different fractions. Therefore, the distinction among them cannot be exact[28,30,36]. Heavy oils may have much higher amount of asphaltenes than resins. Resins are important in the sense that they are the main factor by which the asphaltenes remain dispersed in the heavy crude oil[29]. A physical model of asphaltene piptization is shown in Fig. 1.4 which is based on the thermodynamic-colloidal model of Leontaritis-Mansoori[37]. According to this model, if the adsorption equlibrium of the resins between solid and liquid phases is disturbed for example by adding a paraffin solvent, the asphaltene particles flocculate irreversibly[30]. The flocculated asphaltenes can be re-dissolved in a good solvent (benzene or toluene), however, in the absence of enough resin molecules the asphaltenes start to grow in size. In many cases a complete separation of resins from asphaltenes is impossible. The peptizing effect of resin molecules prevent asphaltene molecules to form self-aggregations[38].

Asphaltenes are considered as unit sheets with an aromatic polycyclic centre. In polar or aromatic solvents asphaltenes may interact with each other to form micelles consisting of several layers via $\pi - \pi$ association of heteroatom coordination[39]. In general, the identification and quantification of asphaltenes without the time-consuming and laboratory based SARA analysis is a difficult task. However, it would be desirable to provide an in situ technique for detecting asphaltenes in order to be able to react in due time to a fluctuation of their concentration. An effort in this respect will be taken to identify the concentration and molecular dynamics of asphaltene in different natural crude oils as well as in asphaltene and model molecule solutions.

Chapter 2

Theoretical Overview

2.1 Basics of NMR

The nucleus of an atom is described by some fundamental physical parameters such as mass, size, charge, spin, magnetic dipole moment and electric quadrupole moment. Of these properties the nuclear magnetic resonance (NMR) mostly considers the nuclear spin, magnetic dipolar and electric quadrupolar moments. The spin angular momentum was recognized in the 1920's and following the ambiguity in explaining the fine structures in the atomic spectra of electrons and some atomic nuclei without considering the existence of another intrinsic angular momentum[40].

The spin is a purely quantum mechanical concept. But the concept of spin angular momentum, and in general fundamentals of NMR, can be reasonably explained by classical mechanics. Each nuclear spin is associated with a magnetic moment $\boldsymbol{\mu}$. In the presence of an external magnetic field $\mathbf{B_0}$, the magnetic moment experiences a torque of

$$\mathbf{\Gamma} = \boldsymbol{\mu} \times \mathbf{B_0}. \tag{2.1}$$

This torque tends to line up the magnetic moment with the external magnetic field so that to reach its lowest energy configuration. But for a non-static magnetic moment, which is the case for atomic nuclear spins similar to the electric current loop in $\mathbf{B_0}$, the magnetic moment $\boldsymbol{\mu}$ is proportional to the angular momentum $\mathbf{I}$ of spin, Fig. 2.1. In this case, the exerted torque produces a change of the angular momentum dI in the same direction (not magnitude) as the torque and perpendicular to the angular momentum $\mathbf{I}$ and magnetic moment $\boldsymbol{\mu}$. This consequently leads to the precession of the nuclear magnetic moment around the axis (anti-)parallel to the $\mathbf{B_0}$[41]. This is exactly similar to the precession of a top with a difference that the torque produced in a top is because of the action of gravity field of the earth, while in NMR the precession is because of the action of external magnetic field. The torque can be represented as the rate of change of the nuclear spin angular moment and from Eq. (2.1) we get

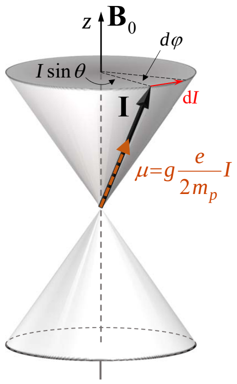

Figure 2.1: A classical picture of the interaction of a magnetic moment $\boldsymbol{\mu}$ with an external magnetic field $\mathbf{B_0}$. The torque (not shown here) is parallel to the change of angular momentum dI and in the direction of the precession.

$$\begin{gathered}\Gamma = \frac{dI}{dt} = I\sin\theta\,\overbrace{\frac{d\phi}{dt}}^{\omega_0} = \mu B_0\sin\theta = g\frac{e}{2m_p}IB_0\sin\theta, \\ \omega_0 = g\frac{e}{2m_p}B_0 = \gamma B_0,\end{gathered} \tag{2.2}$$

where ω_0 is the angular precession velocity or the Larmor frequency, g is the g-factor of the nucleus, e is the elementary charge, and m_p is the proton rest mass. γ is the gyromagnetic ratio and can be positive (e.g. ^{1}H, ^{19}F, ^{13}C) or negative (e.g. ^{15}N, ^{17}O), which defines the sense of precession of the magnetic moment with respect to the $\mathbf{B_0}$ field being clockwise and counterclockwise, respectively. In other words, the spin angular momentum $\mathbf{I}$ and the magnetic moment $\boldsymbol{\mu}$ are in the same direction for $\gamma > 0$, and vice versa.

The operator which represents the energy, the observable quantity, in quantum mechanics is the Hamiltonian $\hat{H}$[42]. For a nuclear spin in a magnetic field of strength B_0 along the z-axis the Hamiltonian which represents the energy of interaction between one spin and the magnetic field is

$$\hat{H} = -\gamma B_0 \hat{I}_z, \tag{2.3}$$

where $\hat{I}_z$ is the z-component of the nuclear spin angular momentum. $\hat{I}_z$ can have different eigenvalues $(2I+1)$ depending on the spin of the nucleus which is specified by the nuclear spin angular momentum quantum number I or in short, spin quantum number. I can take integer and half-integer values. Every atomic nucleus possesses a fixed I and only those with $I > 0$ are NMR active. As an example, the proton ^{1}H nucleus has spin $I = 1/2$ and it has two eigenfunctions with eigenvalues $\pm 1/2$.

The energy of interaction between a single spin-½ with an external magnetic field $\mathbf{B_0}$ along z-direction is given by

$$E = -\boldsymbol{\mu}\cdot\mathbf{B_0} = -B_0\mu_z. \tag{2.4}$$

Knowing the relationship between $\boldsymbol{\mu}$ and $\mathbf{I}$, Fig. 2.1 and Eq. (2.2), the energy in terms of operators is obtained as[42]

$$\hat{H} = -\gamma \hat{I}_z B_0 = \omega_0 \hat{I}_z. \tag{2.5}$$

The proportionality of $\hat{H}$ and $\hat{I}$ indicates that both operators have the same eigenfunctions. Therefore, the energy of states in angular frequency unit is

$$\begin{aligned} \hat{H} \left|\psi\right\rangle &= E \left|\psi\right\rangle, \\ E &= \pm\frac{1}{2}\gamma B_0. \end{aligned} \tag{2.6}$$

This is the case for nuclei with spin-½ (like ^{1}H, ^{19}F, and ^{13}C). For a transition to happen between two energy levels, the change in the spin quantum number (Δm) must be equal to $+1$ or -1. Additionally, the energy difference between the levels must be equal to the frequency of the radio frequency pulse.

2.2 Stochastic Processes

Because of the stochastic nature of the molecular motion and collisions, the local fields generated by every spin will be randomly oscillating. In isotropic liquids where there is an equal probability for a molecule to reorient in any direction, the molecules are not free to reorient due to collisions and viscosity of molecules. Every collision only slightly changes the orientation of the molecule and actually several collisions are needed for a full rotation of the molecule. The tumbling of molecules (rotation or translation) cause changes in the magnitude and direction of the magnetic field exerted by one spin on the other spins (Fig 2.2). The local field fluctuations expose a time dependent transverse magnetization $\mathbf{B}_x(t)$ which is different for every spin. The fluctuating transverse fields have zero average $\langle B_x(t) \rangle = 0$ but a non-zero magnitude $\langle B_x^2(t) \rangle \neq 0$, where brackets show ensemble average over all spins. By taking the model of hard molecules of radius r with spherical symmetry, it is assumed that the rotation of a molecule in a medium with viscosity η can be described by a diffusion equation of form[43]

$$\frac{\partial \Psi(\mathbf{r}, t)}{\partial t} = D \Delta \Psi, \tag{2.7}$$

where Δ is the Laplace operator on the surface of the hard sphere and D is the diffusion constant which for rotational diffusion D_s is given by the Stokes-Einstein relation

$$D_\mathrm{s} = \frac{kT}{b\pi r \eta}, \tag{2.8}$$

where b takes values between 4 and 6 (known as *slip* and *stick* conditions) but it is not bound to this range in experimental conditions. The time dependence of reorientational motion of such molecule can be expressed by spherical harmonics. Therefore, the autocorrelation function can be calculated[43,44] which is

$$G(\tau) = \langle B_\mathrm{x}(t) B_\mathrm{x}(t+\tau) \rangle = \langle B_\mathrm{x}^2 \rangle \, e^{-|\tau|/\tau_\mathrm{c}}, \tag{2.9}$$

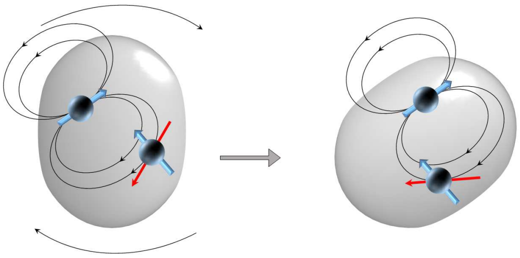

Figure 2.2: Modulation of the local dipolar field as a result of molecular rotation. The blue vectors are the nuclear magnetic moments and the red vectors show the direction of the local fields of one spin sensed by the other spin at two instances of a rotational motion. The change in direction of the red vector resembles a simple case of the fluctuation of local fields due to the reorientation of a molecule.

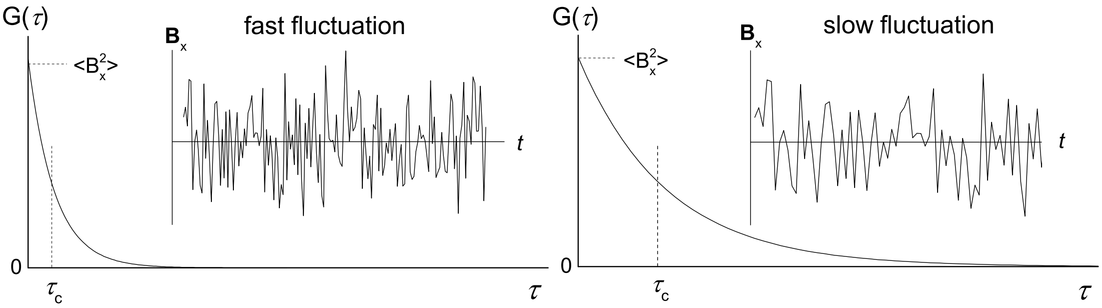

(a) (b)

Figure 2.3: Fast and slow fluctuations of transverse magnetic fields and the corresponding short and long decay of autocorrelation functions, respectively. Refer to text for explanation.

where τ is the time interval, $\langle B_{\mathrm{x}}^2 \rangle$ is the magnitude of the local field at time zero, and τ_{c} is the correlation time of the motion. Autocorrelation functions describe the time dependence of random motions or how rapidly the local field fluctuates in a stochastic processes. Figure 2.3 illustrates the autocorrelation function and the transverse magnetic field fluctuations for slow and fast stochastic motions.

The quantification of the magnitude of fluctuating local fields at different (Larmor) frequencies necessitates the Fourier transformation of the autocorrelation function which gives the spectral density $\mathbb{J}(\omega)$ function for the rotational diffusion

$$\mathbb{J}(\omega) = 2\int_0^\infty G(\tau)e^{-i\omega\tau_{\mathrm{R}}}d\tau = 2\,\langle B_{\mathrm{x}}^2\rangle\,\frac{\tau_{\mathrm{R}}}{1+\omega^2\tau_{\mathrm{R}}^2}. \tag{2.10}$$

The spectral density in Eq. (2.10) is dependent on the source of the local fields and therefore, scales the spectral density accordingly[44]. The reduced spectral density, $J(\omega)$, is defined as Eq. (2.11) to be independent of the source and magnitude of the local fields. For the rest of the text, the term *spectral density* will refer to the *reduced*

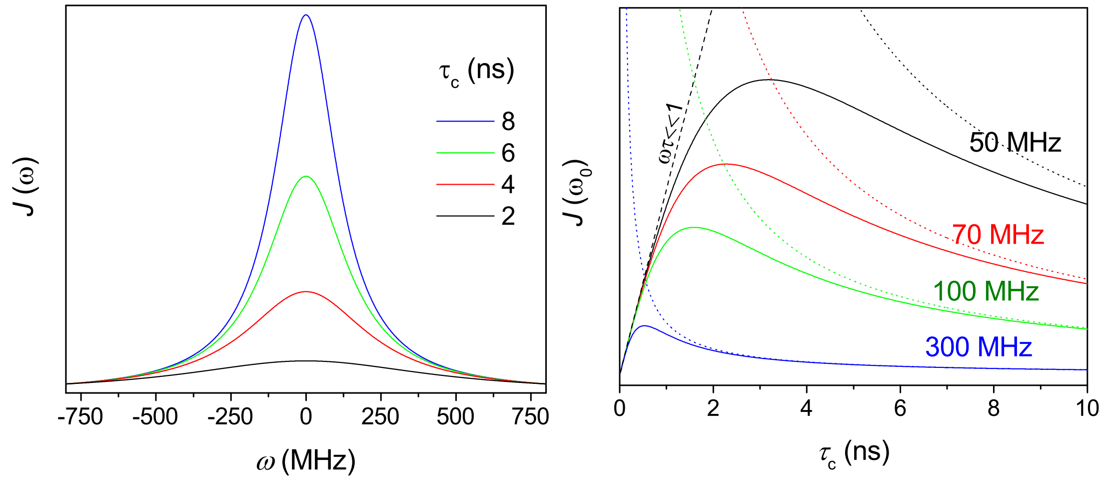

(a) (b)

Figure 2.4: Spectral density function simulations at a) constant correlation times with varying frequency, and at b) constant Larmor frequencies with varying correlation times. See text for more explanation.

spectral density.

$$J_{\mathrm{R}}(\omega) = \frac{\mathbb{J}(\omega)}{\langle B_{\mathrm{x}}^2 \rangle} = \frac{2\tau_{\mathrm{R}}}{1+\omega^2\tau_{\mathrm{R}}^2}. \tag{2.11}$$

The simulation of spectral density functions at four correlation times is shown in Fig. 2.4a. The spectral density decays at larger frequencies with a rate of decay proportional to the τ. The peak hight of $J(\omega)$ is higher for larger τ whereas $J(\omega)$ spreads to higher frequencies with less total intensity for shorter τ_{c}. The variation of $J(\omega)$ with correlation time at some fixed frequencies is shown in Fig. 2.4b. The maximum of $J(\omega)$ appears at $\tau = 1/\omega_0$. In molecular dynamics studies by NMR it is usually useful to compare the Larmor frequency and the correlation time of the molecule. Two extreme (motional) cases are introduced: the fast motion limit (or extreme narrowing condition) and slow motion limit (or spin diffusion condition). The fast motion limit is usually true for small molecules in a non-viscous medium where the τ is so short that $\omega\tau << 1$ and $1 + \omega^2\tau^2 \approx 1$. Therefore the spectral density function becomes independent of the Larmor frequency,

$$J(\omega) = 2\tau. \tag{2.12}$$

The linear dependence of $J(\omega)$ to τ is shown in Fig. 2.4b by a black dashed line. The slow motion case is usually seen for macromolecules in highly viscous medium where τ is so long that $\omega\tau >> 1$ and $1 + \omega^2\tau^2 \approx \omega^2\tau^2$. Therefore

$$J(\omega) = \frac{2}{\omega^2\tau}. \tag{2.13}$$

The simulation of Eq. (2.13) is shown in Fig. 2.4b by dotted lines for every frequency.

To describe the spin-spin interactions of spins on different molecules the translational motion of the molecules should be considered. Here again it is assumed that the diffusion equation, Eq. (2.7), is valid. The solution of the diffusion equation in spherical harmonics assuming a molecular jump distance of d leads to the correlation function[43]

$$G(t) = \frac{N}{d^3}\int_0^\infty \left[J_{3/2}(\rho d)\right]^2 \exp\left(\frac{-2D}{d^2}(\rho d)^2 t\right)\frac{d(\rho d)}{\rho d} \tag{2.14}$$

where N is the number density of spins, $J_{3/2}$ is the Bessel function of order $3/2$, and ρ is the reciprocal of the distance vector in its Fourier space. By assuming the jump distance equal to the minimum distance of approach of molecule ζ which is equal to the molecular diameter, and taking the dimensionless integration variable as $\rho d = u$, and the effective diffusion coefficient as $D = \zeta^2/2\tau_{\mathrm{T}}$, the Fourier transformation gives the spectral density for the translational motion

$$J_{\mathrm{T}}(\omega) = \frac{2N\tau_{\mathrm{T}}}{\zeta^3}\int_0^\infty \left[J_{3/2}(u)\right]^2 \frac{u}{u^4+\omega^2\tau_{\mathrm{T}}^2}du. \tag{2.15}$$

τ_{T} is the translational correlation time and is defined as the average time necessary for a molecule to make a single random molecular jump distance of ζ. Similar motional conditions in Eq. (2.12) and Eq. (2.13) also apply for Eq. (2.15).

2.3 Nuclear Spin Relaxation: Two Spin Case

An undisturbed spin system, a sample in the magnetic field, reaches a state of thermal equilibrium after a certain time. For spins-½, it is understood from Eq. (2.6) that the external magnetic field needed to generate an energy level difference of ΔE in the order of the room temperature thermal energy, $k_{\mathrm{B}}T$, would be $B_0 \approx 10^5\,\mathrm{T}$, which is nearly impossible. Therefore, the nuclear magnetic moments align almost randomly in $\mathbf{B_0}$ field of available NMR devices ($B_0 \approx$ or $< 30\,\mathrm{T}$). However, due to the large number of magnetic moments which is proportional to the Avogadro number N_{A} according to the Boltzmann distribution $\frac{N_-}{N_+} = e^{-\gamma\hbar B_0/k_{\mathrm{B}}T}$, there is a slight statistical preference for the spin population to align with the $\mathbf{B_0}$ field. As a result, an equilibrium macroscopic magnetization $\mathbf{M_0}$ is generated along $\mathbf{B_0}$ field that precesses around it with the Larmor frequency of ω_0, as shown in Eq. (2.2).

In a quantum mechanical description, spins possess some magnetic energy as a result of interaction of magnetic moments of spins $\boldsymbol{\mu}$ with the magnetic field $\mathbf{B_0}$. At equilibrium this energy is the lowest ($\boldsymbol{\mu}$ aligned with $\mathbf{B_0}$) because of the slightly statistically higher population of the lower energy state. An rf pulse of Larmor frequency disturbs the equilibrium and causes spins of lower state to absorb the necessary transition energy from the thermal motion of the surrounding molecules. These spins tend to lose the extra energy back to the surrounding. The flow of energy between spins and the surrounding is facilitated by the local field fluctuations. Different sources of local-field fluctuating are called relaxation mechanisms. The thermal motion of molecules in a medium (and molecular collisions) is the main source of local field fluctuations for spin-½ nuclei[44]. In the following, the relaxation theory will be developed for a simple but practical case of two nuclear spins-½: **1** and **2**, shown in Fig. 2.2. The spin interactions in general can be intramolecular and intermolecular.

2.3.1 Longitudinal Relaxation

The system assumed here is composed of numerous isolated pairs of spin-½ nuclei and no pair has any effect on the other pairs. The Zeeman Hamiltonian representing the interaction of the nuclear moment of two spins with the external magnetic field is given by

$$\hat{H} = \omega_1 \hat{I}_{1\mathrm{z}} + \omega_2 \hat{I}_{2\mathrm{z}}, \tag{2.16}$$

where ω_1 and ω_2 are the Larmor frequencies and $\hat{I}_{1\mathrm{z}}$ and $\hat{I}_{2\mathrm{z}}$ are the z-components of the spin angular momentums of spins **1** and **2**, respectively. Two eigenfunctions describe the state of each spin-½, shown here by $|\alpha\rangle$ and $|\beta\rangle$. For two coupled spins-½, the product of eigenfunctions of individual spins form four eigenfunctions. Figure 2.5a shows the Zeeman energy levels and the transition Probabilities (W) of a spin-½ pair. The relaxation equations can be obtained in terms of population and transition probabilities between energy states through calculating the rate of change of population of each state. The z-magnetizations of spin **1** and spin **2** are proportional to the expectation or average values of the z-components of the spin angular momentum operators $\langle\hat{I}_{1\mathrm{z}}\rangle$ and $\langle\hat{I}_{2\mathrm{z}}\rangle$ as following[44]

$$\begin{aligned} \langle\hat{I}_{1\mathrm{z}}\rangle &= (n_{\alpha\alpha} - n_{\beta\alpha}) + (n_{\alpha\beta} - n_{\beta\beta}), \\ \langle\hat{I}_{2\mathrm{z}}\rangle &= (n_{\alpha\alpha} - n_{\alpha\beta}) + (n_{\beta\alpha} - n_{\beta\beta}), \end{aligned} \tag{2.17}$$

where, for example, $n_{\alpha\alpha}$ represents the population of spins in $|\alpha\alpha\rangle$ state. The longitudinal relaxation, by definition, is described by the rate of change of $\langle\hat{I}_{1\mathrm{z}}\rangle$ and $\langle\hat{I}_{2\mathrm{z}}\rangle$ as below

$$\begin{aligned} \frac{d\,\langle\hat{I}_{1\mathrm{z}}\rangle}{dt} &= -R_1\Big(\langle\hat{I}_{1\mathrm{z}}\rangle - \langle\hat{I}_{1\mathrm{z}}\rangle^{\mathrm{eq}}\Big) - \sigma_{12}\Big(\langle\hat{I}_{2\mathrm{z}}\rangle - \langle\hat{I}_{2\mathrm{z}}\rangle^{\mathrm{eq}}\Big), \\ \frac{d\,\langle\hat{I}_{2\mathrm{z}}\rangle}{dt} &= -\sigma_{12}\Big(\langle\hat{I}_{1\mathrm{z}}\rangle - \langle\hat{I}_{1\mathrm{z}}\rangle^{\mathrm{eq}}\Big) - R_2\Big(\langle\hat{I}_{2\mathrm{z}}\rangle - \langle\hat{I}_{2\mathrm{z}}\rangle^{\mathrm{eq}}\Big), \end{aligned} \tag{2.18}$$

where

$$\begin{aligned} R_1 &= W_0 + 2W_1^1 + W_2, \\ R_2 &= W_0 + 2W_1^2 + W_2, \\ \sigma_{12} &= W_2 - W_0. \end{aligned} \tag{2.19}$$

R_1 and R_2 are the longitudinal relaxation rates for spins **1** and **2**, respectively, and σ_{12} is the cross-relaxation rate which describes the rate spin **1** magnetization is transferred to spin **2** by the relaxation process. The subscripts of the transition probabilities $W^i_{\Delta\mathrm{m}}$ indicate the change in the total magnetic quantum number, m, and the superscripts show the spin whose eigenstate is changing.

The solutions of differential equations in Eq. (2.18) are linear combinations of two exponential functions. For practical applications, they are reduced to a single exponential function through two assumptions that spins **1** and **2** are **a)** homonuclear, **b)** heteronuclear with different relaxation rates.

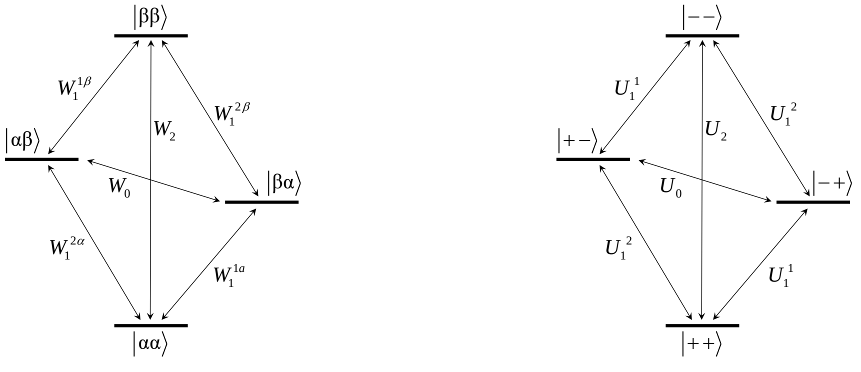

(a) (b)

Figure 2.5: a) The energy levels and transition probabilities W for the Zeeman Hamiltonian and b) eigenfunctions of $\hat{I}_{\mathrm{x}}$ and the transition probabilities U, for a two spin-½ case.

a) Homonuclear Spins In this case, $\omega_1 = \omega_2$, therefore $W_1^1 = W_1^2 = W_1$ and the observed value will be the sum of expectation values of two spins. Note that any possible chemical shift, that can cause deviation of the Larmor frequencies, has been ignored here. The equation of motion for the observable quantity can be written as[45]

$$\frac{d\Big(\langle \hat{I}_{1\mathrm{z}}\rangle + \langle \hat{I}_{2\mathrm{z}}\rangle\Big)}{dt} = -\big(2W_1 + 2W_2\big)\bigg(\langle \hat{I}_{1\mathrm{z}}\rangle + \langle \hat{I}_{2\mathrm{z}}\rangle - \Big(\langle \hat{I}_{1\mathrm{z}}\rangle^{\mathrm{eq}} + \langle \hat{I}_{2\mathrm{z}}\rangle^{\mathrm{eq}}\Big)\bigg), \tag{2.20}$$

and solving the above equation gives

$$\langle \hat{I}_{\mathrm{z}}\rangle (t) = \Big(\langle \hat{I}_{1\mathrm{z}}\rangle + \langle \hat{I}_{2\mathrm{z}}\rangle\Big)(t) = \Big(\langle \hat{I}_{\mathrm{z}}\rangle (0) - \langle \hat{I}_{\mathrm{z}}\rangle^{\mathrm{eq}}\Big)\exp(-{}^{t}\!/\!_{T_1}) + \langle \hat{I}_{\mathrm{z}}\rangle^{\mathrm{eq}}, \tag{2.21}$$

where T_1 in this case is given by

$$\frac{1}{T_1} = 2W_1 + 2W_2. \tag{2.22}$$

The calculation of transition probabilities W necessitates information about the perturbation Hamiltonian. By considering the dipole-dipole mechanism for the relaxation (the most dominant mechanism for spin-½ nuclei) the local fields are generated by spin fluctuations. Therefore, the net magnetic field experienced by spin **1** is the sum of external magnetic field and the local magnetic field of spin **2** at the site of spin **1**, and vice versa. The local field strength experienced by spin **1** is proportional to the gyromagnetic ratio of both spins (larger $\gamma \Rightarrow$ larger magnetic moment $\Rightarrow$ stronger local field) and inversely proportional to the distance between them. The classical energy of interaction for two magnetic moments $\boldsymbol{\mu}_1$ and $\boldsymbol{\mu}_2$ is given by

$$E = \frac{\mu_0}{4\pi}\left(\frac{\boldsymbol{\mu}_1 \cdot \boldsymbol{\mu}_2}{r^3} - 3\frac{(\boldsymbol{\mu}_1 \cdot \mathbf{r})(\boldsymbol{\mu}_2 \cdot \mathbf{r})}{r^5}\right), \tag{2.23}$$

where μ_0 is the magnetic permeability of the vacuum ($= 4\pi \times 10^{-7}\,\mathrm{H\,m^{-1}}$) and r is the dipole-dipole distance. By substituting $\boldsymbol{\mu} = \gamma \hat{I}$, the dipolar Hamiltonian $\hat{H}_\mathrm{D}$ can be written as following[43]

$$\hat{H}_\mathrm{D} = -\frac{\mu_0 \gamma_1 \gamma_2}{4\pi r^3}\left(3\frac{(\hat{I}_1 \cdot \mathbf{r})(\hat{I}_2 \cdot \mathbf{r})}{r^2} - \hat{I}_1 \cdot \hat{I}_2\right). \tag{2.24}$$

The local magnetic field generated by nuclear spins-½ is much smaller in comparison to the external magnetic field strength. Therefore the perturbation theory approximation can be used to calculate the dipolar Hamiltonian in spherical coordinates

$$\hat{H}_\mathrm{D} = d_{12}\Big[\hat{A} + \hat{B} + \hat{C} + \hat{D} + \hat{E} + \hat{F}\Big], \tag{2.25}$$

where $\hat{A}$ to $\hat{F}$ are the dipolar alphabets in terms of second degree spherical harmonics and d_{12} is the coupling constant between spins **1** and **2**[46]. By calculation of the matrix elements of the dipolar Hamiltonian in the eigenstates of the Zeeman Hamiltonian shown in Fig. 2.5a the transition probabilities can be calculated. By considering the spectral density for the intramolecular interaction (rotational diffusion) in Eq. (2.11) the intramolecular homonuclear spin-lattice relaxation rate gets the form of the BPP (Bloembergen–Purcell–Pound) equation[47]

$$\frac{1}{T_{1,\,\mathrm{R}}^{\mathrm{homo}}(\omega)} = \frac{3}{10}\left(\frac{\mu_0}{4\pi}\right)^2 \frac{\gamma^4 \hbar^2}{r^6}\Big(\frac{\tau_\mathrm{R}}{1+\omega^2\tau_\mathrm{R}^2} + \frac{4\tau_\mathrm{R}}{1+4\omega^2\tau_\mathrm{R}^2}\Big). \tag{2.26}$$

In a similar process the homonuclear intermolecular (translational diffusion) relaxation rate can be written as

$$\frac{1}{T_{1,\,\mathrm{T}}^{\mathrm{homo}}(\omega)} = \frac{3\pi}{10}\left(\frac{\mu_0}{4\pi}\right)^2 \gamma^4 \hbar^2 \Big(J_\mathrm{T}(\omega) + 4J_\mathrm{T}(2\omega)\Big), \tag{2.27}$$

where the $J_\mathrm{T}(\omega)$ corresponds to the spectral density of the translational motion given in Eq. (2.15).

b) Heteronuclear Spins In the case of two different spins with Larmor frequencies $\omega_1 \neq \omega_2$, it is assumed that one spin, for example spin **2**, relaxes much faster than the other spin, spin **1**, due to interaction with the environment and not due to the interaction with the spin **1**. Therefore, it can be assumed that in the time scale of spin **1** relaxation time, spin **2** is already at its equilibrium $\langle \hat{I}_{2\mathrm{z}} \rangle = \langle \hat{I}_{2\mathrm{z}} \rangle^{\mathrm{eq}}$[43]. As a result, the rate of change of the z-component of the angular momentum of spin **1** will be

$$\frac{d\,\langle \hat{I}_{1\mathrm{z}} \rangle}{dt} = -\Big(W_0 + 2W_1^1 + W_2\Big)\Big(\langle \hat{I}_{1\mathrm{z}} \rangle - \langle \hat{I}_{1\mathrm{z}} \rangle^{\mathrm{eq}}\Big), \tag{2.28}$$

and the relaxation rate

$$\frac{1}{T_1^{\mathrm{het}}} = W_0 + 2W_1^1 + W_2. \tag{2.29}$$

By calculating the transition probabilities the heteronuclear rotational relaxation rate for spin-**1** is obtained as below

$$\frac{1}{T_{1,\,\mathrm{R}}^{\mathrm{het}}(\omega_{1,2})} = \frac{1}{20}\left(\frac{\mu_0}{4\pi}\right)^2 \frac{\gamma_1^2\gamma_2^2\hbar^2}{r^6}\Big(J_{\mathrm{R}}(\omega_1-\omega_2)+3J_{\mathrm{R}}(\omega_1)+6J_{\mathrm{R}}(\omega_1+\omega_2)\Big), \quad (2.30)$$

where $J_{\mathrm{R}}(\omega)$ is the given in Eq. (2.11). Considering the intermolecular heteronuclear interaction of nuclei, the relaxation rate is given as

$$\frac{1}{T_{1,\,\mathrm{T}}^{\mathrm{het}}(\omega_{1,2})} = \frac{3\pi}{10}\left(\frac{\mu_0}{4\pi}\right)^2 \gamma_1^2\gamma_2^2\hbar^2\Big(J_{\mathrm{T}}(\omega_1-\omega_2)+3J_{\mathrm{T}}(\omega_1)+6J_{\mathrm{T}}(\omega_1+\omega_2)\Big), \quad (2.31)$$

and the spectral density $J_{\mathrm{T}}(\omega)$ is given in Eq. (2.15).

2.3.2 Transverse Relaxation

The transverse or spin-spin (T_2) relaxation corresponds to the loss of coherence of spin components precessing in the transverse (x–y) plane. The local field fluctuations at about (1× or 2×)Larmor frequency contribute to the transverse relaxation, similar to the longitudinal relaxation studied in Section 2.3.1. This frequency dependent contribution is called the “non-secular” contribution of the local fields to the transverse relaxation. Unlike the longitudinal relaxation, the z-components of the local fields also contribute to the transverse relaxation by adding to the external magnetic field $\mathbf{B}_0$ that cause spins to precess at slightly different frequencies depending on the strength of magnetic fields in the surrounding and hence, an additional effect on the loss of coherence of spin components precessing in x–y plane. This is called the “secular” contribution of the local fields to the transverse relaxation which is independent of the fluctuating frequency of the *local* fields. A practical example of action of secular part on the transverse relaxation is for the molecules with hindered motion where the frequency of fluctuation of local fields is decreased due to immobilization. In such a case, the frequency dependent contribution of the relaxation does not cause an effective relaxation (as the case for longitudinal relaxation), but the secular or frequency independent contribution remains effective and dominant which causes faster transverse relaxation rates.

The equations describing the transverse relaxation can be obtained in terms of population of energy states and transition probabilities. This is similar to the procedure explained for the longitudinal relaxation with a difference that the energy states will be determined by the eigenfunctions and eigenvalues of the transverse component of the angular momentum $\hat{I}_{\mathrm{x}}$ (or $\hat{I}_{\mathrm{y}}$). The two eigenfunctions of $\hat{I}_{\mathrm{x}}$ for a spin-½ are shown by $|+\rangle$ and $|-\rangle$. The eigenfunctions of the two coupled spins-½, $\hat{I}_{1\mathrm{x}}$ and $\hat{I}_{2\mathrm{x}}$, can be shown as linear combinations of their individual eigenfunctions. Figure 2.5b represents the energy levels corresponding to these eigenfunctions and the transition probabilities U between energy states. Similar to Eqs. (2.17)–(2.19), rate of change of transverse magnetization for two spins can be written as

$$\begin{aligned}\frac{d\left\langle\hat{I}_{1\mathrm{x}}\right\rangle}{dt} &= -\Big(U_0 + 2U_1^1 + U_2\Big)\left\langle\hat{I}_{1\mathrm{x}}\right\rangle - \Big(U_2 - U_0\Big)\left\langle\hat{I}_{2\mathrm{x}}\right\rangle, \\ \frac{d\left\langle\hat{I}_{2\mathrm{x}}\right\rangle}{dt} &= -\Big(U_2 - U_0\Big)\left\langle\hat{I}_{1\mathrm{x}}\right\rangle - \Big(U_0 + 2U_1^2 + U_2\Big)\left\langle\hat{I}_{2\mathrm{x}}\right\rangle.\end{aligned} \tag{2.32}$$

Note that, unlike longitudinal magnetization, there is no transverse magnetization at equilibrium $\left(\left\langle\hat{I}_{1\mathrm{x}}\right\rangle^{\mathrm{eq}} = \left\langle\hat{I}_{2\mathrm{x}}\right\rangle^{\mathrm{eq}} = 0\right)$. The solutions of differential equations in Eq. (2.32) lead to more than one exponential function. To reduce them to a single exponential function, two approximation cases of homonuclear and heteronuclear spins can be considered. Below only the homonuclear case will be considered.

a) Homonuclear Spins. From Eq. (2.32) by assuming homonuclear spins, $\omega_1 = \omega_2 = \omega$ and $\gamma_1 = \gamma_2 = \gamma$, the T_2 relaxation rate can be written as

$$\frac{1}{T_2^{\mathrm{homo}}} = 2U_1 + 2U_2. \tag{2.33}$$

By considering the dipolar Hamiltonian as the pertubation Hamiltonian and taking the autocorrelation functions of the second degree spherical harmonics, the transition probabilities can be obtained. Eventually, the transverse relaxation rate for homonuclear spins takes the form

$$\frac{1}{T_2^{\mathrm{homo}}} = \frac{3}{40}\left(\frac{\mu_0}{4\pi}\right)^2 \frac{\gamma^4\hbar^2}{r^6}\Big(3J(0) + 5J(\omega) + 2J(2\omega)\Big), \tag{2.34}$$

where $J(0)$ is the secular contribution of the local fields. The $J(\omega)$ and $J(2\omega)$ terms are the non-secular parts that are dependent on the local field fluctuation frequency which also contribute to the longitudinal relaxation rates.

2.4 Relaxation in Porous Media

Molecular reorientations exist in general for liquids. These motions, however, are rather restricted when the liquid is confined in porous media. Some additional relaxation mechanisms are raised as a result of physical (= non-chemical) interaction of liquid molecules with the surface. Porosities can be brought either by hard stationary surfaces for example porous glasses and rocks, or by soft surfaces of, for example, macromolecules or aggregates which itself contain some dynamic properties.

In general two phases can be recognized for the liquid in pores: The free or bulk-like phase and the surface bound phase. The bulk-like phase molecule is defined as the molecule beyond the Debye screening length which behaves like bulk. Considering a T_1 relaxation time for nuclei of molecules in each phase, only average relaxation times are observed as long as the exchange between phases is fast and during the time $\tau_{\mathrm{ex}} < T_1$ a particle can scan the whole pore volume,

$$\frac{1}{T_1} = \frac{p_{\mathrm{f}}}{T_1^{\mathrm{f}}} + \frac{p_{\mathrm{b}}}{T_1^{\mathrm{b}}}, \qquad (p_{\mathrm{f}} + p_{\mathrm{b}} = 1). \tag{2.35}$$

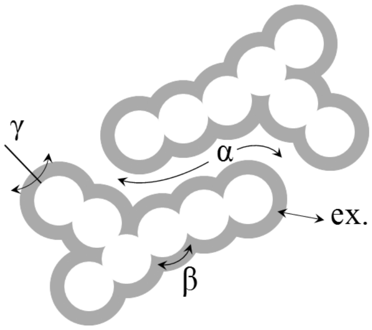

Figure 2.6: A schematic picture of the topological space of the bound phase of molecules in silica fine-particle clusters. The γ-process shows the restricted rotational diffusion about an axis normal to the local surface structure. α- and β-processes show the reorientations mediated by translational displacement (RMTD) for the length scale of the clusters and length scale of a monomer, respectively. The exchange of bound molecules with the free phase is the cut-off limit of the α-process.

If the exchange time $\tau_{\rm ex}$ becomes comparable to the relaxation time T_1, the following average formula applies for the total relaxation time

$$\frac{1}{T_1} = \frac{p_{\rm f}}{T_1^{\rm f}} f_1^{\rm f} + \frac{p_{\rm b}}{T_1^{\rm b}} f_1^{\rm b}, \tag{2.36}$$

with the rate functions defined as

$$f_1^{\rm j} = \frac{\frac{1}{\tau_{\rm ex}^{\rm j}}}{\frac{1}{T_1^{\rm j}} + \frac{1}{\tau_{\rm ex}^{\rm j}}} = \frac{T_1^{\rm j}}{T_1^{\rm j} + \tau_{\rm ex}^{\rm j}}, \qquad (\text{j} = \text{f, b}). \tag{2.37}$$

In complex heterogeneous systems with random pore structures/sizes and non-spherical distribution of pores, a molecule cannot scan all the surface within the T_1 time. Therefore, a distribution of relaxation times will be obtained. By this, one can get information on the pore-size distribution of the system.

Different molecular motions exist in the confined liquid systems. The fast reorientation of a molecule near the surface is restricted to a certain range of solid orientation angles normal to the local surface (γ in Fig. 2.6). This restricted rotational diffusion can be expressed by the following correlation function

$$G_\gamma(t) = a_1 e^{-|t|/\tau_\gamma} + a_2. \tag{2.38}$$

Assuming the liquid molecule to contain protons as the NMR-active nuclei, the proton-proton dipole vector tumbles anisotropically and hence, has a non-spherical symmetric distribution in the space. Ignoring the possibility of (intermolecular) interaction with protons of the neighbouring species in the adsorbed layer, the correlation function $G_\gamma(t)$ of dipole-dipole coupling between these two spins does not average to zero as it would in the isotropic bulk phase. Therefore, the $a_2(= 1 - a_1)$ term in Eq. (2.38) corresponds to the residual correlation in the long-time limit of this process ($t >> \tau_\gamma$)[48]. The residual correlation results splitting of the proton resonance into a doublet with a frequency separation equal to the average dipolar coupling over the non-spherical motion[49]. Here it is assumed that no other process interferes with the γ-process. The coupling depends on the angle between the pore surface and external magnetic field. If there were no exchange between bound and free phases, separate NMR signals would be appeared.

In experimental conditions, the residual correlation is decayed to zero by other processes. One process is the lateral motion of the molecule along the surface. Since the pore surface is curved, the molecule takes relative spatial orientation axis normal to the local surface. The diffusion length ranges from one pore (β) to multiple pore (α) lengths. The displacement can be measured in the topological two dimensional space. The curvature length scales and the probabilities that they contribution to the reorientation of molecules can be analysed via the reorientation structure factor $S(k)$. The correlation function for lateral displacement can be written as

$$G_{\alpha\beta} \approx \int_0^\infty S(k) e^{-|t|/\tau_{\mathrm{k}}}\, dk, \tag{2.39}$$

where $\tau_{\mathrm{k}} = 1/Dk^2$ is the correlation time and k is the wave vector with the unit of a reciprocal length and the τ_{k} is the corresponding correlation time. This is a continuous process and is described as the Reorientations Mediated by Translational Displacements (RMTD).[46]

The other process that can happen independently is the exchange of bound molecules with the bulk phase and the correlation function of this process is given as

$$G_{\mathrm{ex}} = e^{-|t|/\tau_{\mathrm{ex}}}, \tag{2.40}$$

where τ_{ex} is the exchange time. If the isotropic motion of molecule on the surface at $t = \tau_{\mathrm{ex}}$ is not fulfilled by the lateral diffusion process, the remaining correlation is ultimately decayed to zero by the exchange process. Assuming much larger pores than molecule's volume ($r_{\mathrm{pore}} >> r_{\mathrm{molecule}}$) and hence lower population of the bound molecules p_{b} in comparison to the free molecules' population, the exchange time τ_{ex} between phases satisfies the fast exchange limit $\tau_{\mathrm{ex}} << T_{1,\mathrm{f,b}}$[49].

All the three processes in the bound layer are independent and the total correlation function for the adsorbed phase can be obtain as[50]

$$G_{\mathrm{b}}(t) \approx G_\gamma(t) \cdot G_{\alpha,\beta}(t) \cdot G_{\mathrm{ex}}(t),$$

$$G_{\mathrm{b}}(t) \approx a_2 \int_0^{k_{\max}} S(k) e^{-|t|\left[\tau_{\mathrm{k}}^{-1}+\tau_{\mathrm{ex}}^{-1}\right]} dk + a_1 \int_0^{k_{\max}} S(k) e^{-|t|\left[\tau_{\mathrm{k}}^{-1}+\tau_{\mathrm{ex}}^{-1}+\tau_\gamma^{-1}\right]} dk, \tag{2.41}$$

where $k_{\max}$ is the maximum wavelength corresponding to the reciprocal of the molecule size. Assuming that $\tau_\gamma << \tau_{\mathrm{k}} << \tau_{\mathrm{ex}}$ is valid for all k values, the reduced spectral density for the bound phase can be obtained by the Fourier transformation of the correlation function[51,52]

$$J_{\mathrm{b}}(\omega) \approx 2a_1\tau_\gamma + a_2 \int_0^{k_{\max}} S(k) \frac{2k^2 D}{k^4 D^2 + \omega^2} dk, \tag{2.42}$$

where the mode correlation time is defined as $\tau_\mathrm{k} = 1/(Dk^2)$. An analytical formalism for the structure factor is provided in Section 6.2.

In situations where the observed dipolar nuclei is in the vicinity of the surface of a porous media or a macromolecule which contains paramagnetic compounds with unpaired electrons, the relaxation mechanism adopts an additional relaxation mechanism. This case is seen in crude oils where the additional relaxation mechanism is due to the unpaired electrons (radicals) and ions such as vanadyl. The dipolar interaction of the nucleus with the much larger magnetic moment of the electron can have a dominating effect on nuclear spin relaxations. The relaxation rates due to different mechanisms are additive and in such a case can be represented by three main components:

$$\frac{1}{T_1^{\,\mathrm{total}}} = \frac{1}{T_1^{\,\mathrm{rot}}} + \frac{1}{T_1^{\,\mathrm{trans}}} + \frac{1}{T_1^{\,\mathrm{elec}}}. \tag{2.43}$$

where the first term corresponds to the dipolar interactions between spins within the same molecules, Eq. (2.26), second term is the interactions between spins on different molecules, Eq. (2.27), and the third term is the electronic paramagnetic relaxation term[53]. The last term becomes the dominating contribution in the presence of radicals.

2.5 Self-Diffusion

Translational diffusion in a liquid is a result of random thermal motion of molecules. If the liquid is in thermal equilibrium, the random molecular motion is called the self-diffusion and is characterized by a coefficient D ($\mathrm{m^2 s^{-1}}$). At the long-time limit the self-diffusion can be expressed as[54]

$$D = \lim_{t\to\infty} \frac{1}{6t} \left\langle \left[\mathbf{r}_i(t) - \mathbf{r}_i(0)\right]^2 \right\rangle, \tag{2.44}$$

where $\mathbf{r}_i(t)$ is the location of the diffusing particle i at time t, and $\left\langle \left[\mathbf{r}_i(t) - \mathbf{r}_i(0)\right]^2 \right\rangle$ is the mean square displacement (MSD). For isotropic 1D diffusion at, for example, x-axis the MSD can be written

$$\left\langle \left[x(t) - x(0)\right]^2 \right\rangle = \left\langle X^2 \right\rangle = 2Dt. \tag{2.45}$$

Equation (2.45) states the *Fickian* diffusion which is the linear proportionality of MSD to time.

Measurements of the self-diffusion of liquids is possible either by nuclear spin relaxation methods or by magnetic field gradient NMR. The relaxation methods consider the diffusion in microscopic scales since spin relaxations are sensitive to the motions with a timescale of molecular reorientation, i.e. for low-viscose liquids ~ ns to ps. In this case, the correlation time τ_c obtained by relaxation methods is related to the viscosity η of the medium and the radius r of diffusing particle by Debye equation

$$\tau_\mathrm{c} = \frac{4\pi\eta r^3}{3kT}, \tag{2.46}$$

and the diffusion coefficient D is ultimately calculated from Stokes-Einstein equation[54], Eq. (2.8).

Determination of the self-diffusion coefficient by pulsed field gradient (PFG) NMR is done by different standard pulse sequences. In principle, the technique works by generation of a spin echo signal usually in z-direction. Magnetic gradient pulses are applied through the spin echo sequence to decode (label) and encode (read) spin positions. In the presence of the magnetic field gradient G_z the total magnetic field flux is

$$\begin{gathered}\mathbf{B}(t,\mathbf{r}) = B_0 + B(t,z);\\ B(t,z) = g(t)z, \qquad g(t) = \frac{\partial B_\mathrm{z}(t)}{\partial z},\end{gathered} \tag{2.47}$$

where $g(t)$ is the pulsed magnetic field gradient. The total Larmor frequency in this case can be written as

$$\omega(t,z) = \overbrace{\gamma B_0}^{\omega_0} + \overbrace{\gamma g(t) z}^{\omega'}, \tag{2.48}$$

where ω_0 is the Larmor frequency in the absence of the pulsed field gradient and ω' is the additional frequency because of the applied field gradient along-z. It can be taken as the frequency in the rotating frame of reference. ω' causes a space dependent phase change of the magnetization which can be calculated by taking the integral over the length of the gradient pulse δ.

$$\phi(z) = \int_0^\delta \omega' dt = \gamma z \int_0^\delta g(t) dt = \gamma g \delta z. \tag{2.49}$$

Therefore, at the end of the gradient pulse of length δ the spins accumulate a z-dependent phase shift ϕ compared to the case of no pulsed field gradient. This applies a phase modulation of $e^{i\phi}$ on the local magnetization in the rotating frame $M'_\mathrm{x}+iM'_\mathrm{y}$. As a result, the local magnetization is twisted along the gradient direction in a helix form. The spatial dependence of the local magnetization acts as a label and the diffusing particles are encoded via the phase of their spins. Upon diffusion of the particle the phase distribution of local magnetization is smeared out. But since the local magnetizations are functions of sine and cosine, the smearing out will affect the amplitude and not their periods. The second gradient pulse refocuses the phase shift and a spin echo signal as a macroscopic magnetization is recorded. The amplitude of the echo is attenuated by a factor proportional to the gradient strength and diffusion time. The analysis of the echo amplitude for varying gradient strengths (or diffusion times) leads to the diffusion coefficient. The echo attenuation for the case of stimulated-echo pulsed field gradient method is explained in Section 3.4.

Chapter 3

Materials and Methods

3.1 Ionic Liquids

The ionic liquids used in this thesis are:

- Emim Tf2N: 1-ethyl-3-methylimidazolium bis(trifluoromethylsulphonyl) imide
- Bmim Tf2N: 1-butyl-3-methylimidazolium bis(trifluoromethylsulphonyl) imide
- Emim Br: 1-ethyl-3-methylimidazolium bromide
- Bmim Br: 1-butyl-3-methylimidazolium bromide
- Hmim Br: 1-hexyl-3-methylimidazolium bromide

Throughout the text the $[\,]^+$ or $[\,]^-$ signs for cations and anions, respectively, will not be shown for simplicity. The ionic liquids were purchased from Sigma Aldrich (Emim Tf2N, Bmim Tf2N, Emim Br, and Bmim Br), and from Ionic Liquids Technologies (Hmim Br) and used without further purification. The ILs were placed individually in a vacuum oven for at least 24 h at 110 °C under vacuum of 2 mbar to remove the possible water or dissolved gasses. IL samples for different NMR experiments were placed in 5 mm and 10 mm tubes and flame sealed afterwards.

The Vycor Porous glass (VPG, no. 7930, 96% SiO_2, Corning Inc.) was used for the study of confinement effects on Bmim Tf2N. The average pore diameter provided by the manufacturer is 4 nm with a porosity of 28 % and specific surface of $250\,m^2\,g^{-1}$. To remove the adsorbed vapour from Vycor glasses they were boiled in 30 % H_2O_2 for 2 h and then stored in distilled water. These Vycors were then dried in oven at 110 °C and 2 mbar vacuum for at least 48 h to remove the water content. The temperature of the oven was lowered to room temperature and then the vacuum oven was purged with a flow of N_2 gas. The Vycor glasses were dropped in the bulk (oven dried) ionic liquid and left in oven at room temperature and dropped pressure. The full adsorption was estimated by the change of the optical view of Vycor glasses from opaque to transparent. These Vycor glasses were removed from the bulk ionic liquid and the outer surfaces were blotted from the bulk ionic liquid. The ready Vycor glasses were placed in 5 mm and 10 mm NMR tubes and flame sealed at the end.

Table 3.1: The compositions of oils used in this study as weight percent from SARA analysis. The second part of the table shows viscosities of oils.

	A13	A0	W0
		Wt%	
Saturate	38	67	96
Aromatic	32	25	4
Resin	18	8	0
Asphaltene	13	0	0
viscosity (cP)	73	9	11

3.2 Crude Oil

The crude oils as well as pure asphaltenes were provided by the Schlumberger-Doll Research. The SARA analysis for these crude oils are given in Table 3.1. Violanthrone-78 (VO-78) is used as a proposed model for asphaltene molecules and Fig. 3.1 shows its chemical structure. The organic and perfluorinated substances used as solvents or tracers are: benzene (n-benzene), toluene (n-toluene), perdeuteriotoluene (toluene-d8), $CDCl_3$ (chloroform-d), perfluorobenzene (benzene-F6), 1,4-difluorobenzene (benzene-F2), perfluorotoluene (toluene-F8), trifluorotoluene (toluene-F3), pentafluorotoluene (toluene-F5), perfluorooctane (octane-F18), and perfluoropentadecane (pentadecane-F32).

Oil samples were stored in a dark place to protect from light by filling in dark containers. The oils were shaken for several hours before preparing the NMR samples. For all tracers with the exception of perfluoropentadecane, a defined amount of tracer in vol% was added (percent values are given for each experiment in chapter 7). Only in the case of perfluoropentadecane, which is solid at room temperature, a solid sample of about 1 wt % was added and allowed to dissolve in the oil during shaking. The prepared samples were filled into NMR tubes of 10 and 5 mm and kept at ambient temperatures and protected from light. For all oil and asphaltene samples, the solution state and the absence of any non-dissolved bulk solvent were verified by obtaining ^{19}F-NMR spectra at a magnetic field strength of 7.05 T (equivalent to a ^{19}F Larmor frequency of 282 MHz) employing a Bruker Topspin 300 spectrometer with a multinuclear high-resolution probe.

3.3 Instruments

- Differential Scanning Calorimetry (DSC) experiments were carried out on a Perkin-Elmer 7 Series Thermal Analysis System. An empty pan was used as the reference. Evaporated liquid nitrogen served as the cooling agent and a mixture of dry nitrogen and argon gasses (ratio 2:1) was used as the base purge gas for cooling. Dry nitrogen gas was constantly purged through the sample. Oven dried samples with masses between 10 mg and 40 mg were prepared in aluminium pans. Cooling/heating rates of 5 K/min to 20 K/min were used.

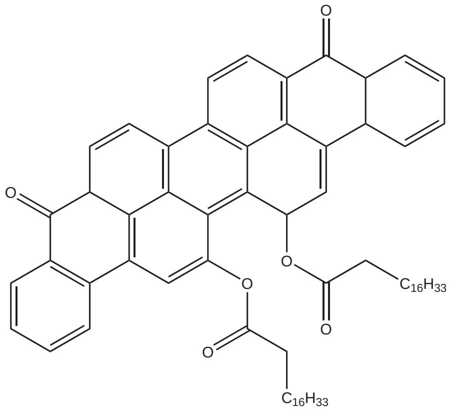

Figure 3.1: The chemical structure of Violanthrone-78

- NMR relaxometry and spectroscopy experiment at room temperatures and for oil samples were done using a Bruker Topspin 300 NMR spectrometer. Dry air was used to control the temperature. The length of the 90° pulse was 8 µs. T_1 relaxation times were obtained using the inversion recovery pulse sequence with typically 16 to 32 time intervals with 32–64 scans. T_2 relaxation times were obtained by the CPMG pulse sequence with a pulse separation of 100 to 200 µs. Sufficient number of echoes were employed to allow the signal to decay below 1%.

- NMR relaxometry and diffusometry experiments on ILs at varying temperatures were done by a Bruker Avance III 300 NMR spectrometer. The temperature regulation was done either by a dry air flow or by the vaporized liquid nitrogen flow. The maximum gradient achievable was $12\,\mathrm{T\,m^{-1}}$ and a 90° pulse length of 6.5 µs was used. T_1 relaxation times were obtained using the inversion recovery pulse sequence with typically 16 to 32 time intervals. T_2 relaxation times were obtained by a CPMG pulse sequence with a pulse separation of 100 to 200 µs. Sufficient number of echoes were employed to allow the signal to decay below 1%. The δ and Δ time intervals for the STE-PFG experiments were between 1 to 2 ms and 100 to 300 ms, respectively. Scan numbers were between 16 and 32.

- Field-cycling experiments were done using a fast field-cycling relaxometer (Stelar s.r.l., Mede, Italy). The Measurement Larmor frequency ranges for ^{1}H and ^{19}F were about 40 kHz to 5 kHz, and for ^{2}Habout 3 kHz to 2 kHz. The pulse lengths used for ^{1}H and ^{19}F experiments were 6 µs while for ^{2}H was 30 µs. Typical number of scans for ionic liquid samples (^{1}H and ^{19}F) were 8 to 16 and for ^{19}F and ^{2}H experiments of oil samples 64.

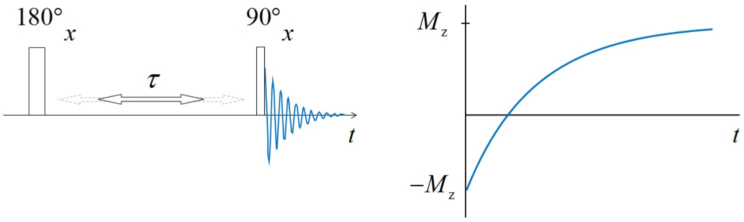

Figure 3.2: Inversion recovery pulse sequence for determination of the T_1 relaxation times of nuclei.

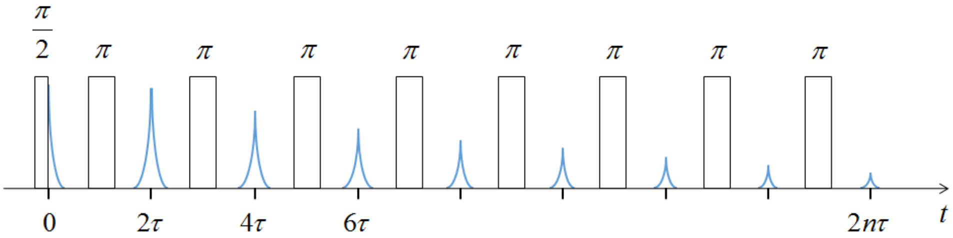

Figure 3.3: CPMG pulse sequence for determination of the T_2 relaxation times of nuclei.

3.4 Experimental Methods

Longitudinal Relaxation Time: To obtain the spin-lattice relaxation times at the high-field (7.05 T) the inversion recovery pulse sequence shown in Fig. 3.2 was used. The delay time τ between the 180° and 90° pulses is variable. Therefore according to Eq. (3.1) a magnetization range from $-M_z$ to M_z is obtained by varying τ from near zero to about five time the T_1 value[41],

$$M(\tau) = M_0(1 - 2e^{-\tau/T_1}). \tag{3.1}$$

Transverse Relaxation Time: The spin-spin relaxation (T_2) time in principle can be measured from the width of the spectral peak. But the magnetic field inhomogeneities in the (liquid) sample broadens the spectral width. To measure the loss of coherences in the transverse plane which is due to fluctuations of the local magnetic fields (microscopic) and not the macroscopic inhomogeneities (instrumental imperfections or susceptibility effects), the spin echo pulse sequence was used. A train of refocusing 180° pulses refocus the spin echoes. This pulse sequence is called CPMG (Carr-Purcell-Meiboom-Gill) and is shown in Fig. 3.3. The T_2 value can be estimated by[46]

$$M_n(\tau) = M_0 e^{-2n\tau/T_2} \tag{3.2}$$

where n is the number of 180° pulses and τ is the time spacing between two 180° pulses.

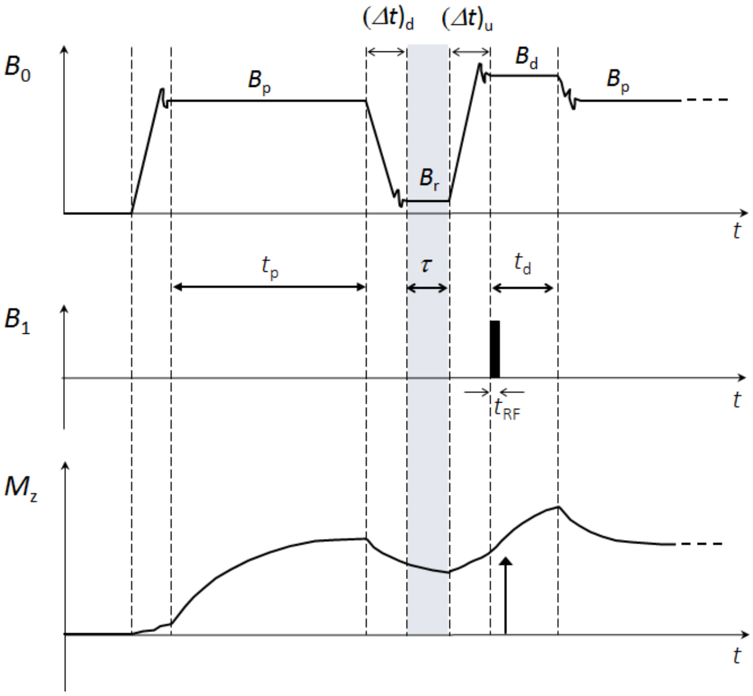

Figure 3.4: The pre-polarization pulse sequence of the field-cycling technique. See text for explanation.

Field-Cycling NMR Relaxometry: The fast field-cycling (FFC) NMR technique is used to obtain a wide frequency map of the spectral density of the fluctuating spin interactions. The field-cycling measurements in this study cover a frequency range from kHz up to 40 MHz for the proton Larmor frequency. The field-cycling NMR probes the molecular dynamics of complex systems through measurement of T_1 relaxation times at a broad range of magnetic field strengths. At low fields the Curie magnetization is small due to the weaker magnetic induction. The FFC overcomes this problem by polarizing and detecting the spin magnetization signal at high fields while allowing the spins to relax at varying magnetic field strengths. The use of a constant detection field for all relaxation fields provides the possibility of optimization of the radio frequency (rf) pulses for the whole experiments. The pre-polarized pulse sequence of the field-cycling technique is shown in Fig. 3.4. The sample is pre-polarized at the polarization field B_p. B_p is chosen to be as high as the cooling apparatus permits. The nuclei in the polarization field reach the Curie equilibrium magnetization ($M_0 \propto B_\mathrm{p}$) after a certain time $t_\mathrm{p} \sim 5 \times T_1$. The magnetic flux B_0 is then switched down to the relaxation field B_r of desire. The field-switching time ($\Delta t = 2.4\,\mathrm{ms}$) and the slew rate ($14\,\mathrm{MHz/ms}$) are selected in a way to avoid the magnetization loss during the switching and at the same time to keep the adiabatic condition at the field changing valid. The nuclei at the relaxation field B_r and immediately after field switching start to relax from the Curie equilibrium magnetization of the polarization field towards the new Curie equilibrium magnetization

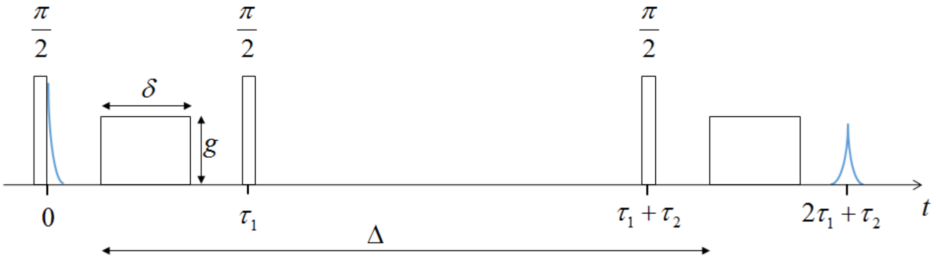

Figure 3.5: The pulse-field gradient (PFG) stimulated echo sequence for the measurement of self-diffusion coefficients.

corresponding to the relaxation field. At different relaxation time intervals τ the field is switched back up to the detection field so that the remaining magnetization from the relaxation process is measured by a 90° read rf pulse[46] during the τ_d. After the detection, the field is switched back to the polarization field and cycle repeats for either different relaxation delays or fields.

Stimulated-Echo Pulsed Field Gradient The stimulated echo pulsed field gradient (STE-PFG) sequence is used for the determination of the diffusion coefficients of ^{1}H and ^{19}F nuclei and is shown in Fig. 3.5. STE-PFG sequence is in particular useful for the self-diffusion measurements of a sample with relatively short T_2 times[54]. Generally ionic liquids are more viscous than common organic solvents. Therefore, strong gradient pulses are used to obtain sufficient echo attenuation and accurate diffusion constants. The echo attenuations are analysed using the formula

$$A(\delta) = \frac{M_0}{2}\, e^{-\gamma^2 g^2 D \delta^2 (\Delta - \frac{\delta}{3})} \cdot e^{-\frac{2\tau_1}{T_2} - \frac{\tau_2}{T_1}}. \tag{3.3}$$

The second exponential term accounts for the relaxation effects during the experiment. During the τ_1 delays, after the first and third pulses, the spins are in the transverse plane and can be affected by T_2 relaxations. After the second $\pi/2$-pulse and during the longer delay time τ_2 the spins are restored to the z-axis and therefore can be affected by the longitudinal relaxations. In cases where T_1 and T_2 are long enough, the second exponential term can be safely ignored[46,54].

Chapter 4

Alkyl Imidazolium Tf2N ILs

Imidazolium based ionic liquids containing the Tf2N as anions are probably the most common ionic liquid in the literature. Various studies on the structure[55], thermal[56,57], transport[58,59], and molecular dynamic properties[60–62] of the neat bulk ionic liquids of this class have been carried out theoretically and experimentally. These studies mostly focused on the ambient and/or higher temperature regions. Some high-field NMR studies revealed that the molecular dynamics of ionic liquids tightly depend on the nature of the counter ions, especially anions[59,63,64].

The accessible self-diffusion coefficient range is limited instrumentally (at stray fields) to values larger than 10^{-14} m^2/s. It was demonstrated that the combination of PFG-NMR and dielectric spectroscopy allowed ion diffusion characterization of substantially slower processes[65]. Even though, molecular dynamics of supercooled ionic liquids remained a question and NMR experiments at lower fields could reveal valuable information. A recent study on Bmim Tf2N showed a dynamic crossover at low temperatures in the structural relaxation process, however, such a crossover was not obvious in the ionic diffusion process[23]. This remains puzzling since the dynamic crossover is expected to appear in all dynamic properties of glass-forming systems.

In this chapter an effort is taken to investigate the dynamics of Emim Tf2N (1-ethyl-3-methylimidazolium bis(trifluoromethylsulphonyl) imide) and Bmim Tf2N (1-butyl-3-methylimidazolium bis(trifluoromethylsulphonyl) imide) ionic liquids at the supercooled temperature region where the molecular tumbling become slower. In the following, the results of DSC, T_1 relaxation dispersion[66], and PFG-NMR self-diffusion experiments[46] are presented and discussed.

4.1 Thermal Studies

The molecular dynamics of ionic liquids in supercooled liquid state is the focus of the current investigation. In order to get an insight into the thermal behaviour and phase transition temperatures of the two ILs, Emim Tf2N and Bmim Tf2N, DSC experiments are performed on each sample. Upon cooling the Emim Tf2N IL from room temperature an exothermic phase transition at 234 K is seen, black line in Fig. 4.1, which corresponds to the crystallization of IL. At a further cooling

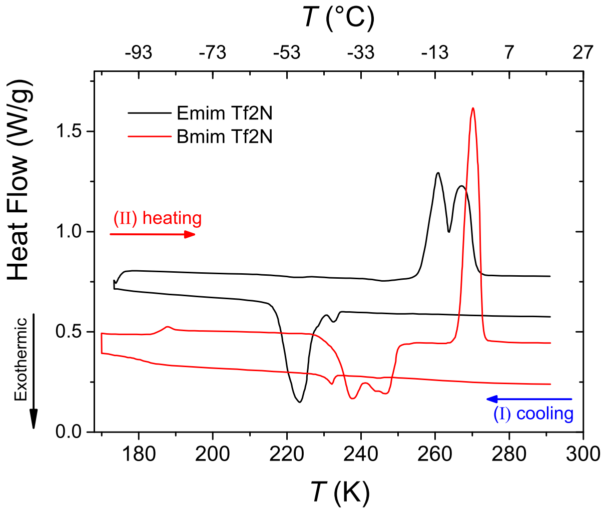

Figure 4.1: Differential scanning calorimetry (DSC) thermograms for Emim Tf2N (black) and Bmim Tf2N (red) during cooling and heating cycles. The exothermic peaks (downward) are related to crystallization and endothermic transitions show melting points and glass transition. The cooling/heating rates: 5 K min^{-1}.

until 173 K no other transition is observed. At the heating cycle, the melting of the crystalline IL is seen with a double step melting that starts at 256 K. The melting occurs at a broad temperature range and finishes at 266 K. At higher temperatures the IL remains liquid. The double melting peaks in Emim Tf2N can have different reasons. The existence of two crystal forms can lead to a two-step melting. But since the crystallization of Emim Tf2N happens in a single step (ignoring the tiny exothermic peak) the idea of two crystal types is unlikely. Alternatively, it can be due to the crystallization of Emim Tf2N at a lower temperature. As a result the crystals may have a less degree of perfection. Such crystals will tend to recrystallize upon heating to form more perfect crystals. In fact, the double melt peaks could be the superposition of an endothermic melting followed by an exothermic recrystallization and lastly an endothermic remelting. The appearance of the melt-crystal-remelt process looks like a double melting peak[67].

The Bmim Tf2N, red thermogram in Fig. 4.1, at cooling cycle from room temperature shows a tiny exothermic transition which is similar to the one observed for Emim Tf2N. However, no crystallization is observed until 184 K and the liquid forms glass below this temperature. Upon heating from 170 K the glass transition $T_g = 184$ K is observed. It is followed by an exothermic transition starting at 233 K. A crystallization that happens in the heating cycle is called the cold-crystallization. The melting of Bmim Tf2N is seen at $T_m = 266$ K.

The small exothermic transitions at 232 K observed for both ILs are reproducible at the same condition. A control DSC experiment was performed with empty pans to check and confirm that it is not a background contamination. It was found that in some cases with higher scan rates the exothermic transition shifts to lower temperatures, Fig. 4.2. These transitions could be due to the partial crystallization

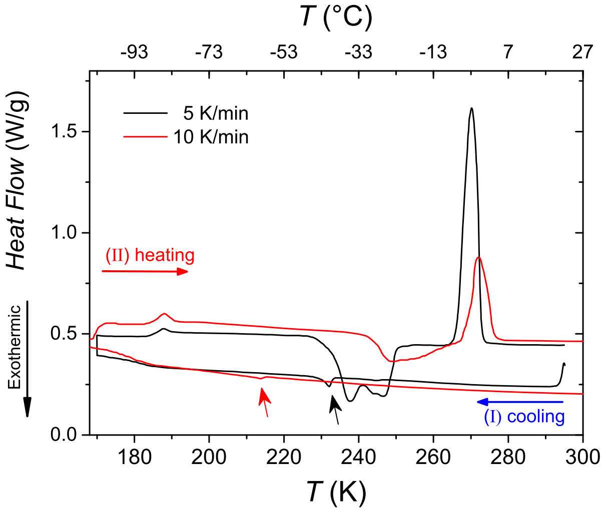

Figure 4.2: DSC thermograms of Bmim Tf2N at the cooling/heating rate of 5 K/min (black) and 10 K/min (red) performed to check the reproducibility of the transition at around 234 K during the cooling process.

of these ILs.

Ionic liquids are generally very sensitive to the lowest impurities. A Bmim Tf2N sample was sent to a different laboratory to perform a DSC experiment. The results show that in some cases at a low scan rate of 5 K/min no cold-crystallization and thus no melting happens (Fig. 4.3). By increasing the scan rate to 10 K/min, the two former transitions are observed. Interestingly, at 5 K/min the small exothermic transition is visible while at rate of 10 K/min there is no sign of it at the cooling process. Although no cold crystallization happens at 5 K/min, a small transition is visible at the melting temperature which could be due to the partial crystallization at the cooling process. The fact that the glassy ionic liquid at the heating cycle experiences no cold-crystallization is interesting. The (ultra-) high viscous glassy state of the supercooled ionic liquid gains mobility by increasing temperature and therefore the viscosity decreases until it reached the room temperature. Possible impurities in the liquid could hinder the crystal formation. However, the investigation of different crystal phases and their formation is not in the scope of this thesis. Some thermodynamical studies have investigated the metastable crystalline phases of Bmim Tf2N[56].

By considering the phase transitions in Fig. 4.1, Emim Tf2N shows a narrower supercooled liquid range (254 K to 230 K) compared with Bmim Tf2N (264 K to 186 K). In the following sections the molecular dynamic studies of these two ionic liquids are presented.

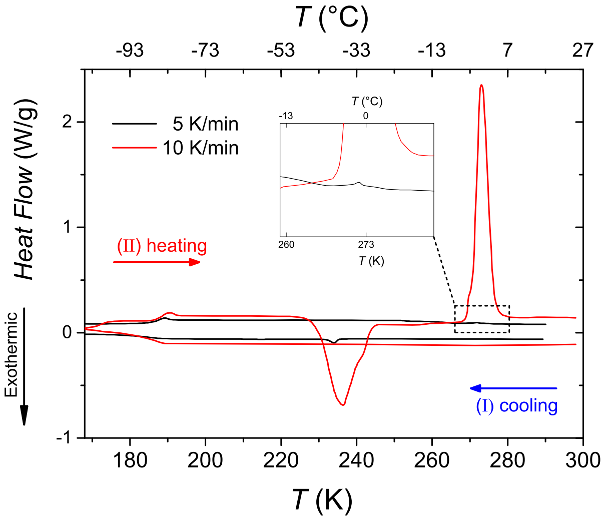

Figure 4.3: Scan rate comparison of DSC thermograms for Bmim Tf2N: black: 10 K/min, red: 5 K/min. Measurements were carried out in IST-Lisbon (by M.T. Viciosa)

4.2 Field-Cycling NMR Relaxometry

The two understudy ionic liquids, Emim Tf2N and Bmim Tf2N, are such that the cations are rich in hydrogen atoms while anions contain high number of fluor atoms and no hydrogen. This is clearly an advantage in NMR studies because it enables to tackle the dynamics of each ionic species individually. Field-cycling NMR relaxometry experiments are done on these ionic liquids covering a broad external magnetic field range. Two series of FFC experiments were carried out on each ionic liquid. First the T_1 relaxation times of ^{1}H nuclei were measured as a function of ^{1}H Larmor frequency at a desired temperature range. Second, ^{19}F-T_1 experiments were carried out as a function of ^{19}F Larmor frequency at the same temperatures. The importance of the measurements at identical temperatures for both nuclei will be cleared later in this chapter.

The temperature ranges used for these two ionic liquids were chosen based on the thermal analysis done by DSC in Section 4.1. Since the main aim of the current study is to investigate the molecular dynamic properties in the supercooled ionic liquids, the focus is on the temperatures below room temperature and down to either a crystallization (for Emim Tf2N) or close to a glass transition (for Bmim Tf2N). The DSC results (Fig. 4.1) showed that the ionic liquids can readily supercool upon cooling from ambient temperatures. The outcome of the field-cycling relaxometry experiments are shown in Figs. 4.4a and 4.4b for Emim Tf2N and Bmim Tf2N, respectively.

At room temperature the relaxation dispersion curves show a weak dependence on the Larmor frequency. Cations and anions of each ionic liquid exhibit similar frequency dependences. Upon decreasing temperature, the ILs exhibit considerable changes in their molecular dynamics reflected by the steeper dispersion of the mea-

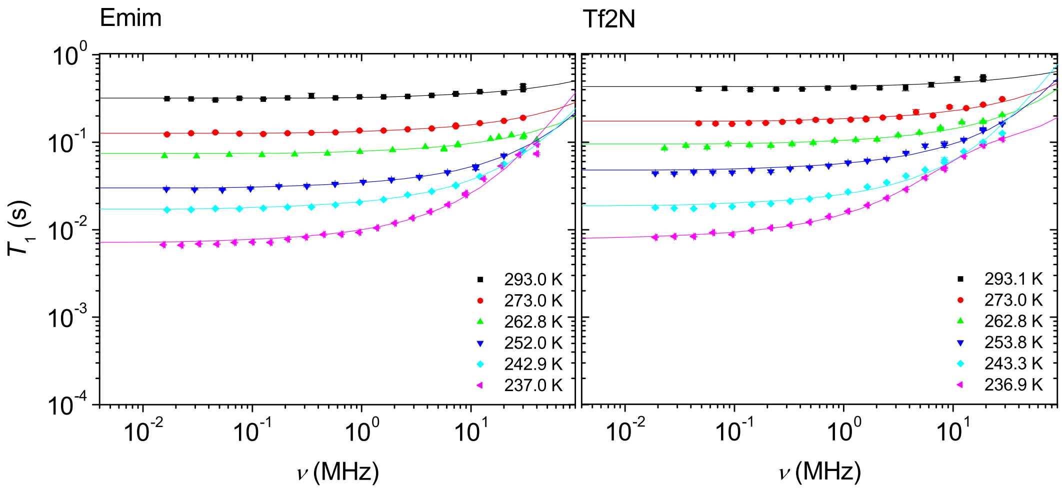

(a) Emim Tf2N

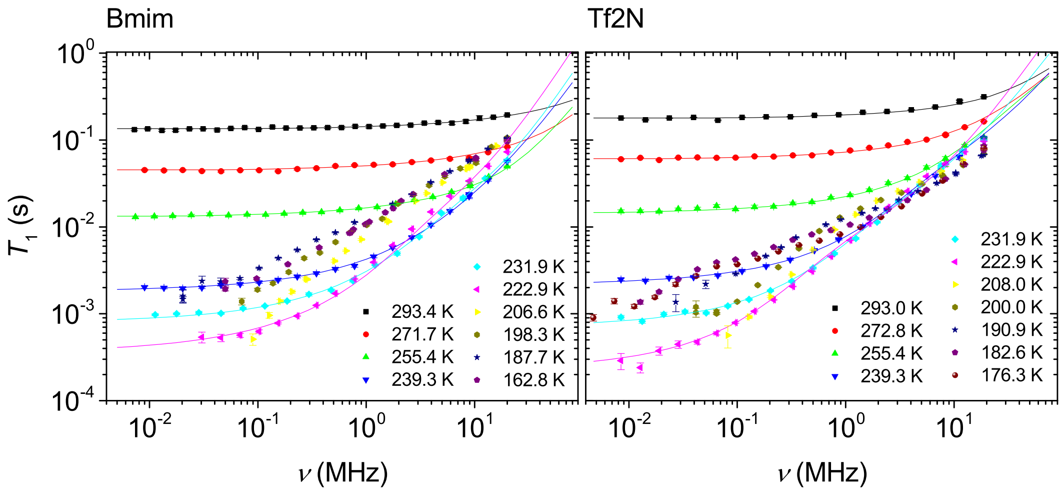

(b) Bmim Tf2N

Figure 4.4: Spin-lattice relaxation times of a) Emim Tf2N and b) Bmim Tf2N as functions of the Larmor frequencies of the measured nuclei obtained by the fast field-cycling technique. The left figures show ^{1}H-T_1 relaxation times and the right ones show ^{19}F-T_1 relaxation times. The solid lines represent the best fits of the experimental data.

sured NMR spin-lattice relaxation times as a function of the external magnetic field.

In order to visualize the temperature dependence of the T_1 relaxation times the relaxation data are represented as a function of the reciprocal temperature for a number of selected Larmor frequencies in Fig 4.5a and Fig 4.5b respectively for Emim Tf2N and Bmim Tf2N.

The T_1-Arrhenius plots for Emim Tf2N cover only the temperatures higher than 237 K below which the IL crystallizes. Cations and anions show similar T_1-temperature dependences where anions show slightly higher relaxation times. No minimum is observed for both ions at the narrow temperature range.

The Arrhenius plots for the T_1 relaxation times of Bmim Tf2N are obtained at a broader temperature range due to the supercooling ability of this ionic liquid. Both ^{1}H- and ^{19}F-relaxation times for Bmim Tf2N are slightly shorter compared to the relaxation times of Emim Tf2N at similar frequencies and temperatures. Since the anions are identical in these two ionic liquids, the reason of different T_1's can be related to the lower viscosity of Emim Tf2N at equal temperatures. Broad T_1 minimums are seen at lower frequencies for Bmim Tf2N and the shape of the curves are generally asymmetric. No indication of a discontinuity is observed which would be a signature of a liquid-solid phase transition process[43]. However, some differences in the temperature dependences of the spin-lattice relaxation times are observed for each ionic species. Above T_g, shown by dotted lines, a minimum in the T_1 values for both ions is found for all the Larmor frequencies shown in Fig. 4.5b. For temperatures lower than T_g for Bmim, the spin-lattice relaxation times do not change for frequencies above 2 MHz. At lower frequencies the T_1 times start to decline as temperature goes down. For the case of anions, the ^{19}F-T_1 relaxation times at slightly above the glass transition temperature show a shallow appearance of a second minimum that shifts to lower temperatures at lower frequencies! This fact emerges as a signature of two different dynamic processes in the anionic molecules for the supercooled ionic liquid. This is, however, surprising that at below T_g the dynamics is not completely frozen.

4.3 Fittings of T_1 Dispersion Profiles

In order to model the T_1 relaxation dispersion curves of Emim Tf2N and Bmim Tf2N ionic liquids and obtain the temperature dependence of dynamical properties, the spin-lattice relaxation equations derived in Section 2.3.1 are used.

Based on the chemical structures of Emim Tf2N and Bmim Tf2N ionic liquids (Fig. 1.2) cations contain protons and anions contain fluor atoms and the spin nuclear dipoles can couple and lead to nuclear spin relaxations. This coupling can be of homonuclear nature (^{1}H-^{1}H and ^{19}F-^{19}F) or heteronuclear (^{1}H-^{19}F). The intramolecular dipolar interactions in these ILs are all of homonuclear type. However, the intermolecular interactions can be of type homo and heteronuclear.

In some previous studies the heteronuclear contributions were somewhat ignored[18]. The T_1 relaxation curves could be satisfactorily explained by only considering the relaxation process due to homonuclear dipolar couplings. This does not mean that heteronuclear dipolar interactions do no exist, rather it suggests that the

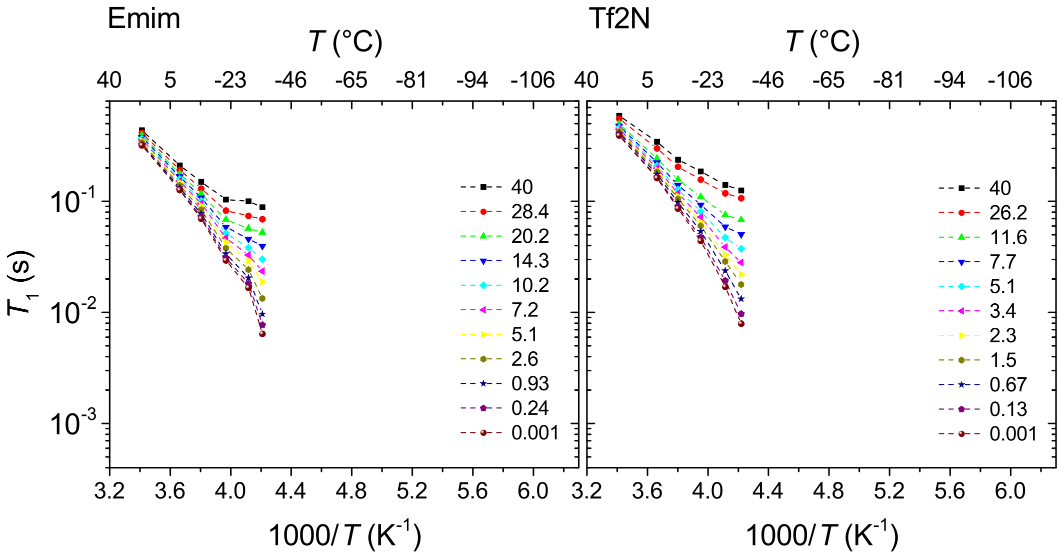

(a) Emim Tf2N

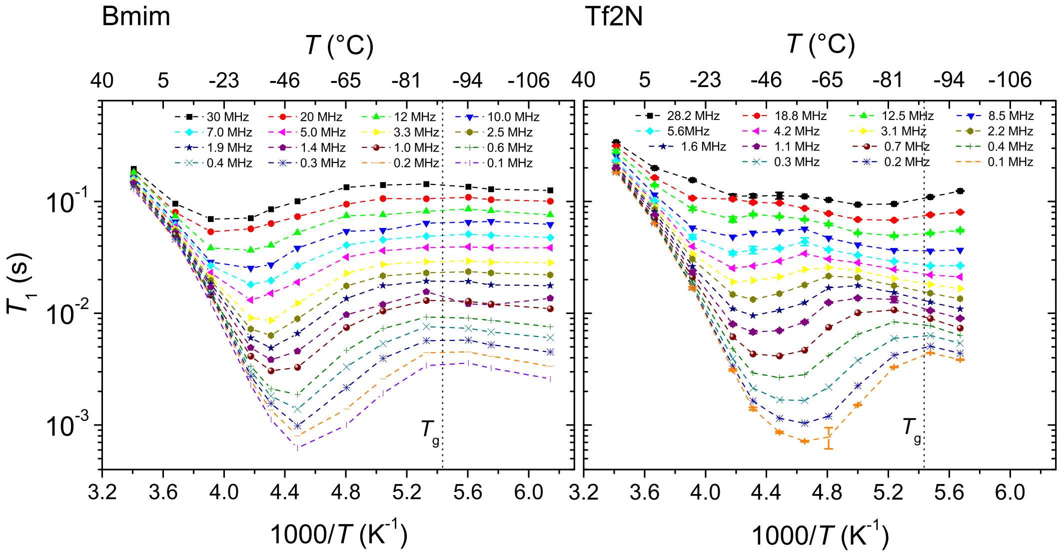

(b) Bmim Tf2N

3

Figure 4.5: Spin-lattice relaxation times as a function of the reciprocal temperature measured by the field-cycling technique. Lines are guide to the eye: a) Emim Tf2N and b) Bmim Tf2N. The left figures show ^{1}H-T_1 relaxation times and the right ones show ^{19}F-T_1 relaxation times. The relaxation and temperature ranges are kept identical for all figures for the sake of comparison.

heteronuclear intermolecular interactions contribute weaker to the total relaxation times compared to the homonuclear interactions. This could be due to differences in gyromagnetic ratios of the interplaying nuclei and their number densities. If the resonance frequencies of two nuclei are so close to each other, the spectral densities of homonuclear and heteronuclear intermolecular dipolar interaction become similar. But the latter is not completely true for ^{1}H and ^{19}F. For each ionic liquid it must be checked whether the simpler model of only homonuclear interactions (intra and inter) can satisfactorily fit the experimental data or inclusion of heteronuclear intermolecular equations are necessary.

4.3.1 Fitting Strategy - 1

Homonuclear dipolar interactions Based on the relaxation equations derived in Section 2.3.1, the physical constants in Eqs. (2.26) and (2.27) are separated from the spectral densities in Eqs. (2.11) and (2.15) for the purpose of fitting. Therefore for intramolecular interactions (rotational diffusion) is written as

$$\frac{1}{T_{1,\mathrm{R}}^{\mathrm{homo}}} = k_{\mathrm{R}}\left[\frac{\tau_R}{1+\omega^2\tau_R^2} + \frac{4\tau_R}{1+4\omega^2\tau_R^2}\right], \tag{4.1}$$

where

$$k_{\mathrm{R}} = \left(\frac{\mu_0}{4\pi}\right)^2 \frac{3}{10}\frac{\gamma^4\hbar^2}{r^6}; \tag{4.2}$$

and for the homonuclear intermolecular dipolar interactions (translational diffusion)

$$\frac{1}{T_{1,\mathrm{T}}^{\mathrm{homo}}} = k_{\mathrm{T}}\left[J'_{\mathrm{T}}(\omega) + 4J_{\mathrm{T}}(2\omega)\right], \tag{4.3}$$

where

$$k_{\mathrm{T}} = \left(\frac{\mu_0}{4\pi}\right)^2 \frac{3}{10}\gamma^4\hbar^2\frac{N}{\zeta^3}. \tag{4.4}$$

The spectral density for the translational diffusion above is shown as J' to indicate that the constants involved in the main spectral density, $2N/\zeta^3$, are included inside k_{T}. The k_{R} and k_{T} will be named as *rotational* and *translational constants.*

Fittings are performed taking the total relaxation rate as

$$\frac{1}{T_1} = \frac{1}{T_{1,\mathrm{R}}^{\mathrm{homo}}} + \frac{1}{T_{1,\mathrm{T}}^{\mathrm{homo}}}. \tag{4.5}$$

A Python code was written to perform the fittings, see Section 8. Therefore four fitting parameters are to be obtained as fitting results: the constants k_{R} and k_{T}, and rotational τ_{R} and translational τ_{T} correlation times. The constant k_{R} contains the molecular radius and therefore it can be considered as temperature independent. But k_{T} can change with temperature. In the fitting, therefore, k_{R} is assumed to be a fixed parameter and the other three parameters are set as free fitting parameters. The value of k_{R} can be calculated if the exact molecular radius is known. Alternatively, this value can be obtained from a single fit to the T_1 relaxation data at a defined

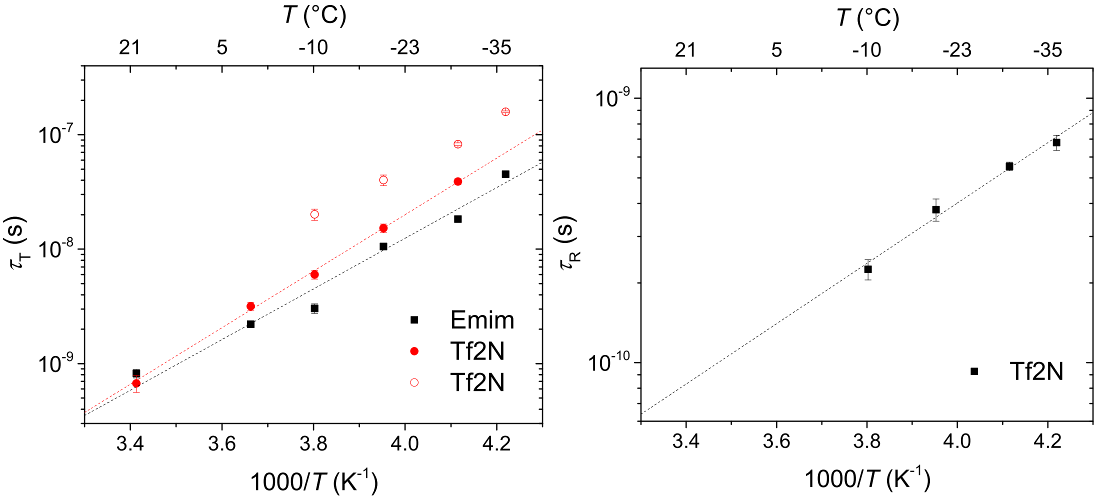

(a) (b)

Figure 4.6: Arrhenius plots of a) translational and b) rotational correlation times obtained from fittings of Emim Tf2N T_1 dispersion data in Section 4.3.1.

temperature – preferably a low temperature where the rotational dynamics is more effective in the frequency windows of the measurement. Then the k_R value is kept as a fixed parameter for the rest of the fittings.

The fitting results for Emim Tf2N are shown in Fig. 4.6. The ^{1}H-T_1 dispersions of Emim Tf2N are fitted only with the intermolecular homonuclear equation. It should be mentioned that the relaxation times of each nuclear at the magnetic field of 7.05 T (300 MHz for ^{1}H and 282 MHz for ^{19}F Larmor frequencies) at all temperatures were also measured and used in the fittings. The correlation time for the intramolecular contribution τ_R is smaller than the time scale of these experiments even at the lowest measured temperature. Therefore, this contribution acts only as an offset factor in the fitting and no correlation time is achieved. The translational correlation times follow a linear temperature dependence from 273 K to 237 K (Fig. 4.6a). Fittings of ^{19}F-T_1 relaxation dispersions for Emim Tf2N show somewhat different results. At temperatures lower than 263 K, the dispersion curves could be fitted with both rotational (Fig. 4.6b) and translational contributions (empty red circles in Fig. 4.6a). Both correlation times show Arrhenius temperature dependences over the narrow temperature range. Almost two orders of magnitude of dynamical range in correlation times is obtained which is usually enough to predict the temperature dependence[68]. The higher temperature range of ^{19}F relaxation dispersions are fitted only by the homonuclear translational relaxation equation since the rotational part plays a role as an offset, as explained above. If these fittings are continued for the lower temperature range of ^{19}F-T_1 by fitting only the translational relaxation equation, where rotational contribution could be actually included, similar temperature dependence is obtained but with smaller τ_T values (full red cycles in Fig. 4.6a). In fact, considering only a single type of dynamics – translational – and ignoring rotational contribution, which is a much faster motion, leads to shorter correlation

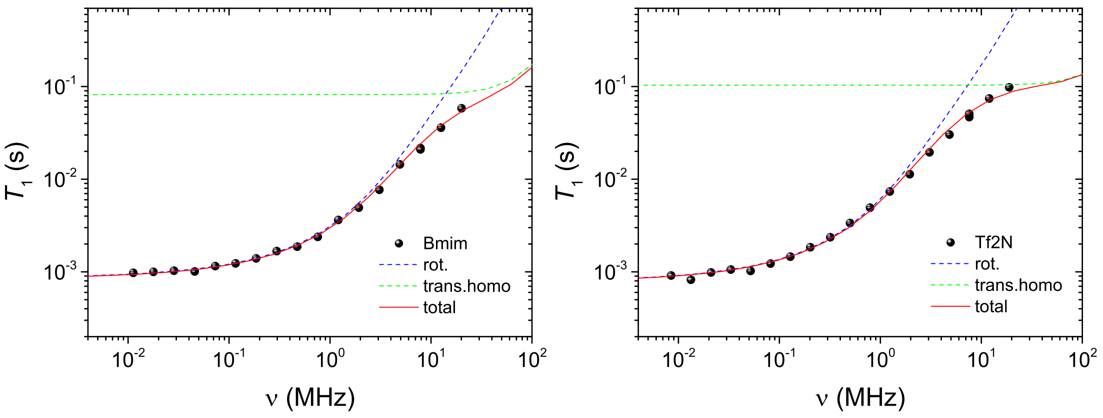

(a) Bmim (^{1}H) (b) Tf2N (^{19}F)

Figure 4.7: Sample fittings of a) Bmim and b) Tf2N T_1 relaxation dispersions considering intramolecular (green) and intermolecular (blue) homonuclear dipolar couplings (Section 4.3.1). The sums of both contributions are shown by red solid lines. The black circles show experimental T_1 times at 293 K. See Fig. 4.4b for results of similar fittings at all temperatures.

times that are averages of slower dynamics/longer correlation times of translational motions and faster motions/shorter correlation times of rotational motions.

The correlations times obtained for Emim Tf2N follow Arrhenius type temperature dependences and activation energies of $45 \pm 3\,\mathrm{kJ\,mol^{-1}}$ for translational and $22\,\mathrm{kJ\,mol^{-1}}$ for the rotational correlation times are obtained. The T_1 fitted curves are shown in Fig. 4.4a as solid lines.

Following Eqs. (4.1)–(4.4) for Bmim Tf2N, both intramolecular and intermolecular contributions are fitted to the T_1 relaxation dispersion data. A sample fit that shows both relaxation contributions is shown in Fig. 4.7. The outcomes of the fit, the translational and rotational correlation times, at the temperature range of 293 K to 223 K show different temperature dependences (Fig. 4.8). The translational correlation times τ_T follow a non Arrhenius temperature dependence. This type of temperature dependence of transport properties is common in glass forming liquids and is usually fitted by the Vogel-Fulcher-Tammann equation: $\tau_\mathrm{T} = \tau_0 e^{\kappa T_0/(T-T_0)}$. The fit parameters are presented in the caption of Fig. 4.8. In comparison to Emim Tf2N ionic liquid, Bmim Tf2N shows to be a *fragile* glass former while Emim Tf2N showed a *strong* behaviour in the narrow supercooled temperature region.

The rotational correlation times, on the contrary to τ_T, follow Arrhenius temperature dependences with activation energies of $8.2 \pm 0.5\,\mathrm{kJ\,mol^{-1}}$ and $13.2 \pm 0.2\,\mathrm{kJ\,mol^{-1}}$ for Bmim and Tf2N, respectively. The differences between the absolute values of $\tau_\mathrm{R}^\mathrm{Bmim}$ and $\tau_\mathrm{R}^\mathrm{Tf2N}$ in Fig. 4.8b can not be interpreted since they vary upon changing the k_R values in Eq. (4.1) while the slopes remain unchanged. Therefore, at this point the shorter rotational correlation times of anions cannot be directly concluded as faster reorientational motions.

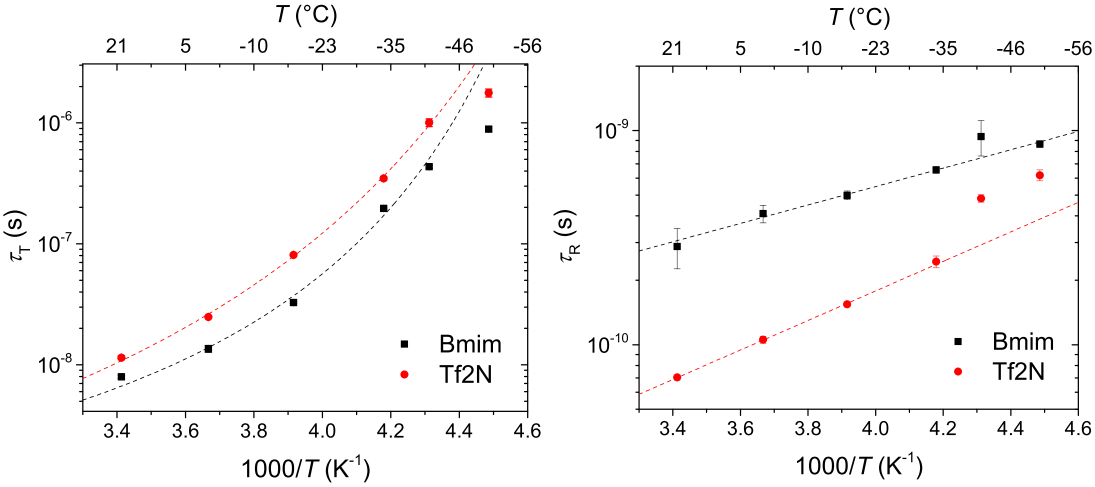

(a) (b)

Figure 4.8: Arrhenius plots of fitting parameters (Section 4.3.1), a) translational and b) rotational correlation times for Bmim Tf2N ionic liquid considering homonuclear intra and intermolecular interactions. The dashed lines show a) VFT fits b) Arrhenius fits. The VFT fit parameters are: $\tau_0^{\mathrm{Bmim}} = 3.28 \pm 0.49 \times 10^{-10}\,\mathrm{s}$, $\kappa^{\mathrm{Bmim}} = 1.65 \pm 0.99$, and $T_0^{\mathrm{Bmim}} = 189.4 \pm 13.0\,\mathrm{K}$; $\tau_0^{\mathrm{Tf2N}} = 1.29 \pm 0.95 \times 10^{-10}\,\mathrm{s}$, $\kappa^{\mathrm{Tf2N}} = 3.13 \pm 0.83$, and $T_0^{\mathrm{Tf2N}} = 171.6 \pm 8.0\,\mathrm{K}$.

4.3.2 Fitting Strategy - 2

Homonuclear and heteronuclear dipolar interactions The following fitting strategy again assumes the model that the total dipolar relaxation is a sum of translational and rotational tumbling of the involved species, but also includes T_1 relaxations due to heteronuclear dipolar interactions,

$$\frac{1}{T_1} = \frac{1}{T_{1,\mathrm{R}}^{\mathrm{homo}}} + \frac{1}{T_{1,\mathrm{T}}^{\mathrm{homo}}} + \frac{1}{T_{1,\mathrm{T}}^{\mathrm{het.}}}. \tag{4.6}$$

Therefore, there will be three correlation times as fitting parameters for each nuclear: $\tau_{\mathrm{T}}^{\mathrm{HH}}$, $\tau_{\mathrm{T}}^{\mathrm{HF}}$ and $\tau_{\mathrm{R}}^{\mathrm{H}}$ for ^{1}H, and $\tau_{\mathrm{T}}^{\mathrm{FF}}$, $\tau_{\mathrm{T}}^{\mathrm{FH}}$ and $\tau_{\mathrm{R}}^{\mathrm{F}}$ for ^{19}F. This gives six correlation times as fitting parameters at every temperature. Taking $\tau_{\mathrm{T}}^{\mathrm{HF}}$ equal to $\tau_{\mathrm{T}}^{\mathrm{FH}}$, since they both represent the correlation time for translational motions of one nuclear with respect to the other, the actual number of fitting correlation times reduces to five being one shared between the two nuclei.

The homo intramolecular and intermolecular coupling constants are given respectively in Eqs. (4.2) and (4.4). The heteronuclear intermolecular coupling constant for ^{1}H can be similarly written from Eq. (2.31) as

$$k_{\mathrm{T}}^{\mathrm{HF}} = \left(\frac{\mu_0}{4\pi}\right)^2 \frac{1}{10}\gamma_{\mathrm{H}}^2\gamma_{\mathrm{F}}^2\hbar^2\frac{N_{\mathrm{F}}}{\zeta_{\mathrm{HF}}^3}. \tag{4.7}$$

By exchanging the scripts ‘H’ with ‘F’ in Eq. (4.7) the corresponding dipolar coupling constant for ^{19}F can also be obtained ($k_{\mathrm{T}}^{\mathrm{FH}}$). It should be mentioned that

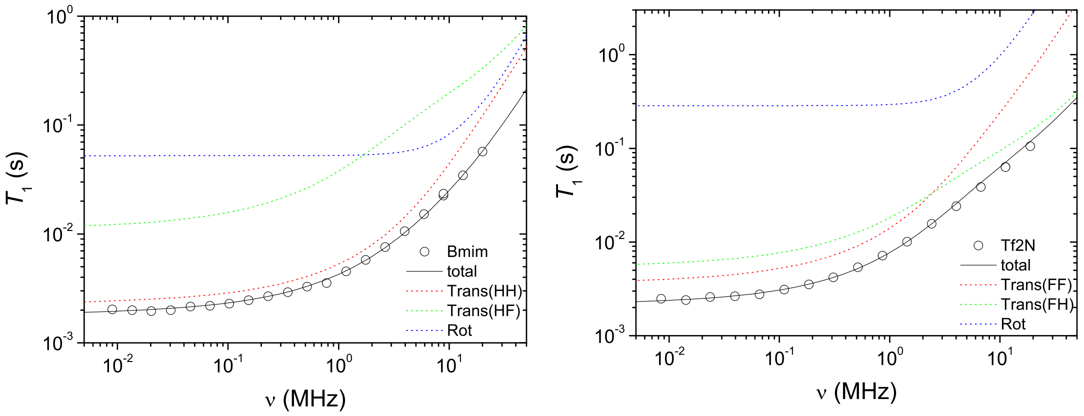

(a) Bmim (^{1}H)

(b) Tf2N (^{19}F)

Figure 4.9: Fitting of T_1 relaxation dispersion data (○) for 239 K for the a) cation and b) anion following Section 4.3.2. The red, green, and blue dashed lines show contributions of homonuclear translational, heteronuclear translational, and rotational diffusion to the T_1 relaxation times, respectively. The black solid lines display the sums of all contributions.

this fitting strategy is applied only on Bmim Tf2N data since Emim Tf2N experiments do not extend to deeper temperatures and the T_1 dispersions could be well fitted in Section 4.3.1.

It is found that for lower temperatures e.g. below 239 K, the dipolar coupling constants get similar values while they tend to vary at higher temperatures. The possible temperature dependent parameters in the dipolar coupling constants are the minimum distance of approach (ζ) and the molecular radius (r). The temperature dependent density measurements have shown a very weak dependence of ILs on temperature[59]. Therefore, the dipolar coupling constants are treated as fixed fitting parameters only at low temperatures. At high temperatures they are allowed to change within few percent of the corresponding values at low temperatures.

The fittings are done using the Python code given in Section 8 and by initially fitting the translational contributions in Eq. (4.6) and then finalizing the fit by introducing the rotational function. Since the translational contributions contain an inter-connected correlation time ($\tau_{\mathrm{T}}^{\mathrm{HF}} = \tau_{\mathrm{T}}^{\mathrm{FH}}$), it is essential to fit the homo- and heteronuclear contributions simultaneously for ^{1}H and ^{19}F relaxation times. This necessitates the existence of T_1 relaxation data at exactly identical frequencies for ^{1}H- and ^{19}F-T_1's. The effort was taken to fulfil this requirement either by matching frequencies at the experimental measurements or by interpolating relaxation times for required frequencies. A sample fit is shown in Fig. 4.9 for a selected temperature of 239 K that shows intramolecular (rotational), and homo- and hetero-intermolecular (translational) contributions to the total relaxation times. It is seen in Fig. 4.9 that the heteronuclear correlation times match with each other ($\tau_{\mathrm{T}}^{\mathrm{HF}}$ and $\tau_{\mathrm{T}}^{\mathrm{FH}}$ shown with green dashed lines) while the corresponding scaling factors are different (more dominant for ^{19}F). The later stems from differences in gyromagnetic ratios and spin densities which influence the coupling constants. This is a clear evidence that the heteronuclear translational relaxation mechanism can be as important as the homonuclear translational mechanism and cannot be ignored specially in the case of spins with lower gyromagnetic ratios and/or lower spin densities than proton's.

The importance of inclusion of heteronuclear spin relaxation mechanism has been also proven clearly in some recent publications. In an investigation on imidazolium based ILs with BF_4 and PF_6 anions, the heteronuclear translational interactions were ignored for ^{1}H-T_1 while taken into account for ^{19}F relaxations[18]. It was further highlighted in a ^{13}C-T_1 NMR relaxation study (at 100 MHz for ^{13}C) on Bmim PF_6[20], where considering the heteronuclear *intramolecular* relaxation contribution of ^{1}H spins on ^{13}C relaxation successfully explained the long standing question of the non-monotonic temperature dependence of the correlation times of the imidazolium ring. Their analysis invalidates, to some extent, the result of several previous investigations[69–75] where other possible relaxation mechanisms were proposed in order to explain the temperature dependence of the correlation times.

This fitting strategy suitably describes the $T_1(\omega)$ dispersion curves of Bmim Tf2N in the range from room temperature until 223 K. Below this temperature deviations in the experimental data and the proposed model become noticeable. The rotational and translational correlation times are obtained as the fit parameters over the mentioned temperature range and are discussed below.

The rotational correlation times τ_R for cations (^{1}H) and anions (^{19}F) are shown in Fig. 4.10b. NMR relaxometry observes an average of all the intramolecular dipolar interactions caused by the internal motions. They follow an Arrhenius temperature dependence in the range from room temperature to 238 K whereas below this temperature, τ_{R} of both ions deviate and apparently become less sensitive to the temperature variation. The Arrhenius regime, above 238 K, are fitted with the Arrhenius equation $\tau_{\mathrm{R}} = \tau_0 e^{E_{\mathrm{a}}/RT}$ and shown with solid lines, where R is the universal gas constant and E_{a} is the activation energy.

The rotational correlation times obtained from the fittings are so much dependent on the rotational dipolar coupling constants, k_{R}'s. That means, acceptable fits are obtainable by using more than one unique rotational coupling constants. Different coupling constants lead to different τ_{R} values. However, the variations of τ_{R} values are found to be within or less than one order of magnitude and the Arrhenius trend is always observed at the same temperature range. Therefore, the error bars shown in Fig. 4.10b show only uncertainties obtained from using a fixed coupling constant and do not include the uncertainties due to the variation of coupling constants. Clearly, including these uncertainties will lead to larger error bars. Therefore, the differences in $\tau_{\mathrm{R}}^{\mathrm{H}}$ and $\tau_{\mathrm{R}}^{\mathrm{F}}$ values at equal temperatures are not discussed here. It is worth mentioning that the van der Waals radii of Bmim cations and Tf2N anions are reported to be equal and 3.30 Å[76].

Unlike rotational dynamics, all three types of translational correlation times do not follow Arrhenius dependences in the same temperature range shown in Fig. 4.10a. The Arrhenius temperature dependence of τ_{R} indicates that the reorientational dynamics is an energy activated process and an activation energy E_{a} can be assigned. The case of non-Arrhenius behaviour of transport phenomena is typical for

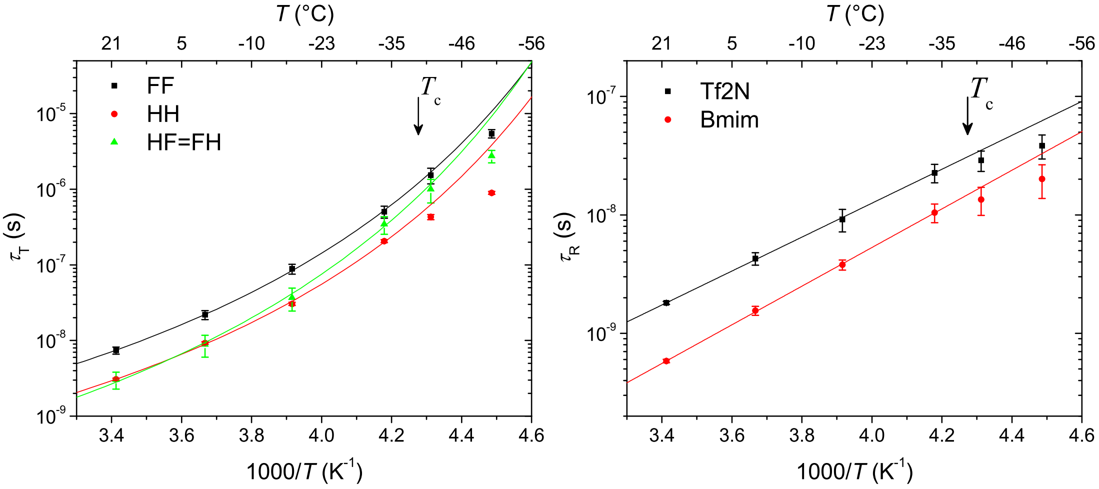

(a) Bmim (^{1}H)

(b) Tf2N (^{19}F)

Figure 4.10: Arrhenius plots. a) Translational correlation times of ^{1}H–^{1}H (red), ^{19}F–^{19}F (black), and ^{1}H–^{19}F (= ^{19}F–^{1}H) (green). b) Rotational correlation times of ^{1}H (red) and ^{19}F (black). The values are obtained from fittings of the T_1 relaxation dispersion curves. The data in (b) are fitted by an Arrhenius temperature dependence (see text) and similar rotational activation energies of $E_R = 29 \pm 2$ kJ/mol are obtained for both ions. The data in (a) are fitted according the VFT law (see text) considering a fixed $T_0 = 170$ K: $\tau_T^{0,\,HH} = 1.42 \times 10^{-11}$ s, $\kappa^{HH} = 3.89$; $\tau_T^{0,\,FF} = 3.09 \times 10^{-11}$ s, $\kappa^{FF} = 3.97$; $\tau_T^{0,\,HF} = 6.24 \times 10^{-11}$ s, $\kappa^{HF} = 4.42$

fragile supercooled liquids. It indicates that the effective activation energy is itself temperature dependent[60], $\tau_{\mathrm{T}} \propto e^{E_{\mathrm{a}}(T)/RT}$. The Vogel-Fulcher-Tammann (VFT) temperature dependence is an empirical formula that is used regularly to fit similar experimental data of supercooled (ionic) liquids,

$$\tau_{\mathrm{T}} = \tau_{\mathrm{T}}^{0} e^{\kappa T_0/T - T_0}. \tag{4.8}$$

In this equation, T_0 is usually denoted as the ideal glass transition temperature, i.e. the theoretical low temperature limit to the liquid state. For molecular and ionic liquids it is around 30 K to 60 K below the calorimetric glass transition temperature T_{g}. In VFT fittings of the cation and anion T_0 must be kept constant. Previously in a high-field NMR study a T_0 of 180 K was found whereas this value can be slightly different depending on the method[60,77]. κ is the fragility parameter constant. Fragility is a phenomenological concept introduced by Angell to characterize how steeply viscosity increases upon cooling. It can be regarded as a measure of degree of cooperative motion[26]. Liquids are called *strong* if Arrhenius behaviour is obeyed while they are called *fragile* in the other case[14]. The fitting parameters are reported in the caption of Fig. 4.10.

As a result of the presented fitting method, the local dynamics of ions of Bmim Tf2N could be achieved. However, no information is obtained on the minimum distances of approach ζ of molecules. In the following, an effort will be made to modify the fitting method in a way to obtain minimum distance of approach parameters out of the T_1-relaxation dispersion data.

4.3.3 Fitting Strategy - 2 (Modified)

The fitting procedure represented here is done similar to Section 4.3.2, with a difference that the ratios of the dipolar coupling constants, k_{T}'s and k_{R}'s, are taken with respect to each other as boundary conditions for fittings. The dipolar coupling constants contain some physical constant parameters as well as the minimum distance of approach ζ values. Therefore, by taking their ratios the physical constant parameters cancel out and leave behind the ratio of minimum distances of approach for different pairs.

By taking the ratio $k_{\mathrm{T}}^{\mathrm{HH}}/k_{\mathrm{T}}^{\mathrm{HF}}$ the coupling constants of homonuclear and heteronuclear intermolecular interactions are bounded together, Eq. (4.9). This is found to be very efficient in the fitting processes, especially in cases where two or more fitting functions exist that the characteristic fitting parameter of these functions lie in the same order of magnitude.

$$\begin{gathered}\frac{k_{\mathrm{T}}^{\mathrm{HH}}}{k_{\mathrm{T}}^{\mathrm{HF}}} = \frac{3\gamma_{\mathrm{H}}^{2} N_{\mathrm{H}} \zeta_{\mathrm{HF}}^{3}}{\gamma_{\mathrm{F}}^{2} N_{\mathrm{F}} \zeta_{\mathrm{HH}}^{3}} = \frac{3\gamma_{\mathrm{H}}^{2} \times 15 \times \zeta_{\mathrm{HF}}^{3}}{(0.9407\gamma_{\mathrm{H}})^{2} \times 6 \times \zeta_{\mathrm{HH}}^{3}} = 8.475 \left(\frac{\zeta_{\mathrm{HF}}}{\zeta_{\mathrm{HH}}}\right)^{3}, \\ k_{\mathrm{T}}^{\mathrm{HH}} = 8.475 \left(\frac{\zeta_{\mathrm{HF}}}{\zeta_{\mathrm{HH}}}\right)^{3} k_{\mathrm{T}}^{\mathrm{HF}} = 8.475\, \zeta_{\mathrm{HF/HH}}^{3}\, k_{\mathrm{T}}^{\mathrm{HF}}.\end{gathered} \tag{4.9}$$

N_{H} and N_{F} represent the number densities or, in this case, equivalently the numbers of each nuclear on one molecule of Bmim Tf2N. Following the same procedure

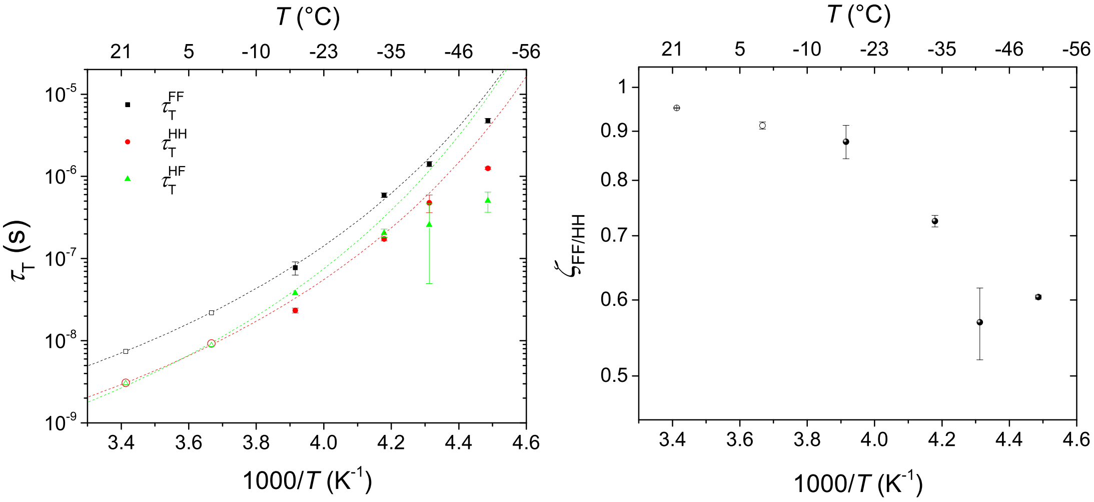

(a) (b)

Figure 4.11: The outcome of approach-2 (modified) fitting in Section 4.3.3 for Bmim Tf2N. a) The correlation times for homonuclear (HH and FF) and heteronuclear (HF) translational motions. The full symbols are obtained from fittings. The VFT fit and empty symbols are taken from Fig. 4.10a. b) The ratios of minimum distances of approach of F–F over H–H at different temperatures. See text for explanation.

similar relation for $k_{\mathrm{T}}^{\mathrm{FF}}/k_{\mathrm{T}}^{\mathrm{FH}}$ is obtained as

$$k_{\mathrm{T}}^{\mathrm{FF}} = 1.062\,\zeta^{3}_{\mathrm{FH/FF}}\,k_{\mathrm{T}}^{\mathrm{FH}}. \tag{4.10}$$

The intramolecular interactions are not considered in this approach since their contribution at low frequencies can be assumed as offsets.

The ratios $\zeta_{\mathrm{HF/HH}}$ and $\zeta_{\mathrm{FH/FF}}$ give information on the relative distances of homo and heteronuclear spins, however, absolute distance values cannot be obtained. At the fitting condition of $\tau_{\mathrm{HF}} = \tau_{\mathrm{FH}}$, the direct distance ratio of H-H and F-F is obtained as

$$\zeta_{\mathrm{FF/HH}} = \frac{\zeta_{\mathrm{HF}}/\zeta_{\mathrm{HH}}}{\zeta_{\mathrm{FH}}/\zeta_{\mathrm{FF}}}. \tag{4.11}$$

By performing the T_1-relaxation dispersion fittings considering the boundary conditions calculated above, correlation times for translational diffusion are obtained (Fig. 4.11a) that match the values reported in Section 4.3.2. Additionally, the ratios of minimum distances of approach are found at different temperatures shown in Fig. 4.11b.

The fittings for temperatures below 263 K are done by leaving the fit parameters free and only the boundary conditions are applied. For the two temperatures above 273 K the correlation times are taken from Section 4.3.2 and set as fix parameters in the fittings, so that the ratios of k's can be calculated to obtain the complete ζ-ratios.

Figure 4.11b shows an interesting behaviour of Bmim Tf2N ionic liquid. At around room temperature, and probably higher, the distances of anion–anion and cation–cation are almost in the same range. In a physical point of, this means homogeneous distribution of charged molecules in the liquid. By decreasing temperature, the anion–anion distance decreases in comparison to the cation-cation distance, or vice versa. This behaviour is magnified below the melting point, $\sim 270\,\mathrm{K}$. At the supercooled region, the anion–anion distance gets almost half of that for cation–cation. This observation suggests the existence of ionic associations in the supercooled Bmim Tf2N ionic liquid. However, more evidences probably from other techniques or simulations are required to confirm this phenomena.

4.4 Self-Diffusion

Independent measurements of the translational diffusion coefficient were carried out covering the same temperature range of relaxometry experiments in order to validate the theoretical NMR relaxation model and the fittings performed in Section 4.2. The translational correlation times obtained from fittings of the relaxation data can be converted to the self-diffusion values. This is done using the relation $\tau_{\mathrm{T,eff}} = \zeta^2/2D$ assuming $\zeta = 3.3\,\text{Å}$, where $\tau_{\mathrm{T,eff}}$ is the effective translational correlation time which is calculated from the equation below and then compared with the stimulated echo PFG-NMR experiments in Fig. 4.12.

$$(\tau^{\mathrm{H}}_{\mathrm{T,\,eff}})^{-1} = (\tau^{\mathrm{HH}}_{\mathrm{T}})^{-1} + (\tau^{\mathrm{HF}}_{\mathrm{T}})^{-1}. \tag{4.12}$$

An excellent agreement is found between the diffusion coefficients obtained directly from the PFG-NMR technique and indirectly from the relaxation data for the whole temperature range that could be covered by both methods. The Diffusion experiments are carrier out only on ^{1}H nuclei (cations). The ^{19}F (anions) self-diffusion coefficients include only the calculated values from ^{19}F-T_1 relaxation data following the same procedure and using Eq. (4.12). The literature self-diffusion data only exist at high temperatures for this ionic liquid[59] whose anion diffusions are in agreement with the values obtained from NMR relaxation in the current study.

Comparison of the anion (Tf2N) and cation (Bmim) transport properties depicted in Fig. 4.10a and Fig. 4.12 show faster translations (shorter τ_{T}) for cations than anions. The Stokes-Einstein (SE) relation correlates the diffusion of rigid spherical particles (microscopic) with the hydrodynamic radius a_0 of the diffusing particles through a medium of viscosity η (macroscopic) at temperature T

$$D = \frac{k_{\mathrm{B}}T}{c\pi\eta a_0}, \tag{4.13}$$

where k_{B} is the Boltzmann constant and c is an empirical constant theoretically between 4 and 6, respectively representing slip and stick boundary conditions[54]. Hayamizu and Handy showed that the fitting of SE equation to the experimental NMR diffusion coefficients and viscosity data for several ionic liquids at temperatures above 273 K result c values even smaller than the theoretical minimum value of $c = 4$[78]. The ionic self-diffusion and viscosity of Bmim Tf2N have been measured in Watanabe's group for temperatures above 283 K. Their analysis proved the case for this ionic liquid that by following SE relation the c value obtained for cations

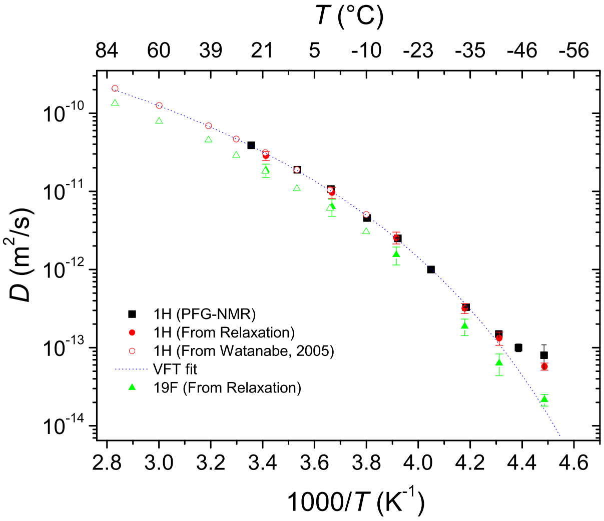

Figure 4.12: Temperature dependence of self-diffusion coefficients for Bmim Tf2N, obtained from the stimulated echo PFG-NMR experiments (black squares) and from the T_1 relaxation data (red circles and green triangles), compared to the results from ref.[59] (empty circles and triangles). The diffusion times in the stimulated echo PFG experiment were chosen to be between 100 ms and 400 ms in order to obtain at one order of magnitude dynamic range. No time dependent diffusion was observed. The dotted line shows the VFT fit to the PFG-NMR data between 298 K and 238 K.

was smaller than for anions, 3.4 vs. 4.3[58,59]. At an equal van der Waals radii for cations and anions in Bmim Tf2N, the smaller c value of the Bmim cation means higher self-diffusion, which is consistent with the self-diffusion values in Fig. 4.12.

Furthermore, interesting information is observed by considering the κ values of the VFT fit in Fig. 4.10a. As mentioned before, the κ values indicate a measure of the of cooperative motion: $\kappa^{\mathrm{HF}} > \kappa^{\mathrm{FF}} >\approx \kappa^{\mathrm{HH}}$. The larger κ^{HF} means that the translational motion of oppositely charged ions are more cooperative than the motion of equi-charged ions. Meanwhile, the motions of anions with respect to neighbouring anions are slightly more cooperative than that of cations. Also remembering the fact that the VFT equation is an empirical relation to explain the temperature dependent effective activation energy; κ can be related to the effective activation energy.

Considering the κ value for anion-anion motion that is slightly larger than the value for cation-cation, this small difference cannot be easily explained. The van der Waals radii of these ions are the same while the molecular weight of anions are almost double of cations (280.15 g/mol vs. 139.2 g/mol). By considering the relation between the molecular weight M_{w} and diffusion D[79]

$$D \propto (M_{\mathrm{w}})^{-1/3}, \tag{4.14}$$

smaller diffusions are expected for anions. On the other hand, the same ionic size of cations and anions leads to equal coulombic forces. However, stronger van der Waals forces are expected for cations than anions because Bmim molecule, due to the aromatic ring, is more polarizable than the anions with fluorine atoms which are small in size and dense in electron.

4.5 Discussion

The thermal analysis of the two ILs, Emim Tf2N and Bmim Tf2N, revealed significantly different thermal behaviour although they differed in the alkyl chain length by only two carbons. Bmim Tf2N IL can easily be supercooled while Emim Tf2N crystallizes just 20 degrees below the melting point. In general, the bulky Tf2N anion makes the molecular ordering and hence crystallization of the liquid more hindered. This is shown in Emim Tf2N as a delayed crystallization and in Bmim Tf2N as completely hindered crystallization at the cooling cycle.

The correlation times obtained from the T_1 relaxation times of Emim Tf2N show Arrhenius-like temperature dependences. Since Emim Tf2N experiences a supercooled liquid state, although at a narrow temperature range, this type of temperature dependence could be associated with the "strong" behaviour of this IL. Even though, the studied temperature range for Emim Tf2N is narrow and the dynamic properties in this temperature range do not change significantly. This makes the conclusion on the type of temperature dependence of these properties uncertain if they are Arrhenius or strong-VFT type.

ILs, as glass forming liquids, undergo viscose slow down on dynamics upon cooling from their melting points. Approximately at $^2/_3\, T_\mathrm{m}$ the liquid enters the glassy state[68]. This behaviour was clearly observed for Bmim Tf2N. In the current study, the dynamics of the supercooled ILs were always studied at the cooling cycle. Emim Tf2N ionic liquid crystallized before reaching a glass transition. The non-crystallizing and glass forming liquids above the glass transition temperature are in equilibrium state and the transport properties deviate from the Arrhenius behaviour which is clearly observable for Bmim Tf2N. Such a behaviour is usually fitted by the VFT equation. But VFT equation best fits for liquids which show only small deviations from Arrhenius behaviour[80]. Therefore, the application of VFT equation for Bmim Tf2N data in this study is only to give a measure of curvature or deviation from the Arrhenius plots. On the other hand, VFT fits still give reasonable physical values for T_0 and the pre-exponent τ_T^0. T_0 is the theoretical glass transition temperature and according to the VFT law, it should be smaller than the measured T_g by calorimetric methods (see caption of Fig. 4.10a). The τ_0 values of $\sim 10^{-14}\,\mathrm{s}$ are reported to be of physical meaning that is the vibrational period of the quasilattice. But this value is found for the structural relaxation studies where much faster (α and β) relaxation times are probed. VFT fits for Bmim Tf2N in the current study give values in the order of $10^{-11}\,\mathrm{s}$. The best procedure in VFT fit would be to keep T_0 and the pre-exponent τ_T^0 fixed for all dynamic properties and turn the VFT to a single parameter equation. Bmim Tf2N shows a fragile behaviour and the single parameter VFT approach usually fits well when there are slight deviations from the Arrhenius behaviours[68]. Contrary to the translational correlation times, the rotational correlation times for Bmim Tf2N show Arrhenius behaviour.

A common feature is observed for the dynamical and transport properties (τ_T,

τ_{R}, D) and that is: at a temperature point between T_{m} and T_{g} there is a breakdown of the temperature dependence trend. This temperature can be defined as the crossover temperature, $T_{\mathrm{c}} \sim 1.2\ T_{\mathrm{g}}$, which is a normal phenomenon reported in supercooled molecular liquids and its observation in supercooled ionic liquids is interesting[60,68,81,82].

Such a crossover has been reported by Griffin et al. for Bmim Tf2N by probing the structural $\alpha-$relaxation process[23,83]. However, these authors observed no sign of a dynamic crossover in the ionic diffusion process. In fact, these authors calculated the ionic self-diffusion coefficients from ionic conductivity measurements using the Nernst-Einstein (NE) equation. The NE relation, $\Lambda = zF^2/RT(D_+ + D_-)$, assumes a complete dissociation of ions[84]. However in cases where some degrees of ion association is present or ionic concentration is high (increased viscosity effect), the original form of the NE relation does not apply and modified versions of the NE relation must be used instead with an empirical constant which is dependent on the ion-ion interaction and hence, different for every ionic liquid. The ideality of an ionic liquid defines the validity of obtaining self-diffusion coefficients from the ionic conductivity data using any of the equations of Nernst-Einstein or Einstein-Smoluchowski. The non-ideal behaviour of Bmim Tf2N has been already shown in Figs. 4.10 and 4.11 (the VFT dependence with large κ and the $\zeta_{\mathrm{FF/HH}}$ values). Furthermore, NMR diffusion measurements reflect average values for diffusion of species in both free and associated forms, thus calculating NMR molar conductivity (Λ_{NMR}) from NE equation is always overestimated[78]. These calculations are plausible when enough knowledge on ion association is available. There are on-going debates about the degree of ion association (ion pairing) in ionic liquids and its temperature dependence[64,78,85–89]. However, in the present study the self-diffusion coefficients measured directly by PFG-NMR, as well as the one derived from the NMR relaxation times show deviations from the VFT behaviour at temperatures below T_{c}.

A possible explanation is that the liquid crossing the T_{c} towards lower temperatures undergoes a kinetic transition from liquid-like to solid-like dynamics[90]. The dynamics at T_{c} and below becomes more spatially heterogeneous and clusters of dynamically correlated regions start to grow[81,91,92]. A crossover temperature has been also reported for similar ionic liquids of the current study using low-frequency Raman spectroscopy and optical Kerr effect studies[60] which propose a cooperative rearrangement in ionic liquids with a correlation length of about 20 Å. Also it is known that in complex liquids where there are more than one type of particle in the liquid, like ions in ionic liquids or small molecules doped into molecular liquids, the motion of small particles decouple from the motion of the bulky particles. For these systems and over a limited temperature range the fractional Stokes-Einstein equation could be applied[68]. But larger deviation and violation of Stokes-Einstein are seen at temperatures approaching T_{c}. Several hypothesis approach the question of crossover temperature feature of glass forming liquids[82,83]. However, a clear understanding of this feature has not been achieved so far.

Chapter 5

Alkyl Imidazolium Bromide ILs

Three ionic liquids with imidazolium based cations and bromide anion are chosen to study in this chapter: 1-ethyl-3-methyl imidazolium bromide (Emim Br), 1-butyl-3-methyl imidazolium bromide (Bmim Br), and 1-hexyl-3-methyl imidazolium bromide (Hmim Br). Understanding the molecular dynamics and transport properties of these ILs are essential in development of the molecular models that will ultimately help predicting the behaviours of these ILs in different application areas.

5.1 Thermal Studies

Room temperature ionic liquids normally show supercooling properties. In order to investigate the supercooling temperature regime as well as the glass transition temperature, the differential scanning calorimetry (DSC) technique is applied on the three alkyl imidazolium bromide ionic liquids: Emim Br, Bmim Br, and Hmim Br. Results of DSC experiments are shown in Fig. 5.1. On the cooling cycle Emim Br and Bmim Br remain liquid below their melting points. Emim Br, however, crystallizes about 70 degrees below the melting point while Bmim Br resists crystallization and forms glass at $T_\mathrm{g} = 218\,\mathrm{K}$. At the heating cycle, the crystals of Emim Br (formed at cooling) start melting at 348 K. Bmim Br, on the other hand, undergoes a cold-crystallization process between T_g and T_m and then it experiences a melting at $T_\mathrm{m} = 333\,\mathrm{K}$. Hmim Br, interestingly, remains supercooled at cooling and heating cycles and only shows a glass transition at $T_\mathrm{g} = 216\,\mathrm{K}$.

Since the main aim of this study is to investigate the dynamics of IL molecules at the supercooled state, the glass forming ILs, Bmim Br and Hmim Br, are chosen for the NMR studies. The NMR studies in the following sections are performed on Bmim Br and Hmim Br only in the supercooled regime and always in the cooling cycles.

5.2 Field-Cycling NMR Relaxometry

Field-cycling relaxometry gives longitudinal nuclear spin relaxation times as a function of the target nuclei's Larmor frequency. The T_1 relaxation dispersion curves for Bmim Br and Hmim Br are shown in Fig. 5.2.

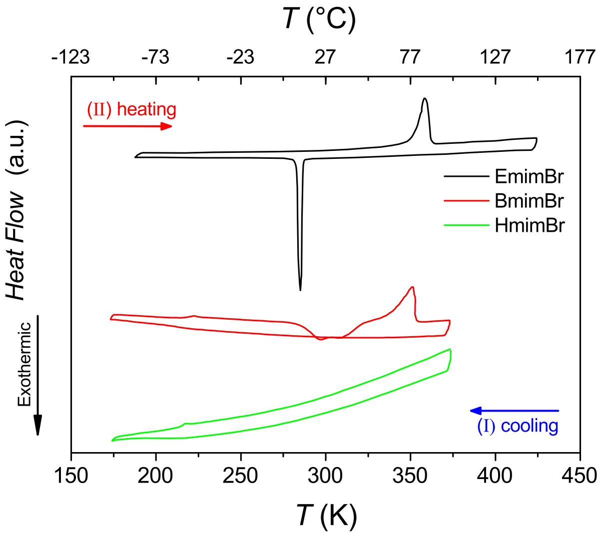

Figure 5.1: DSC thermograms of Emim Br, Bmim Br, and Hmim Br at cooling and heating cycles with the scan rate of 5 K/min

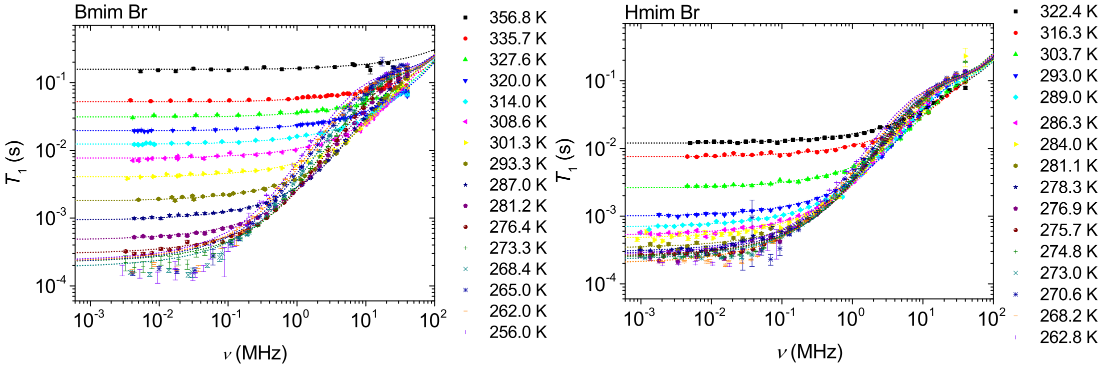

(a) (b)

Figure 5.2: ^{1}H-T_1 relaxation dispersion curves of a) Bmim Br and b) Hmim Br. The dashed lines are the fitting results. See the text.

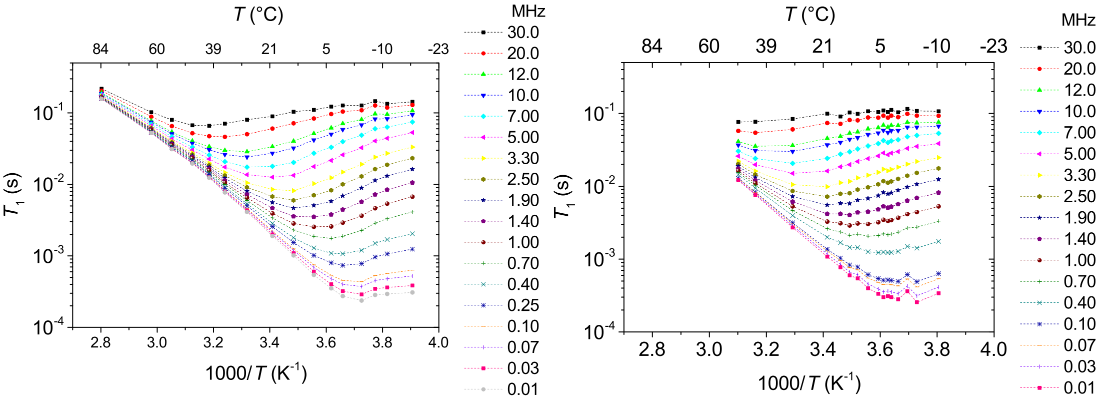

(a) (b)

Figure 5.3: ^{1}H-T_1 Arrhenius plots of a) Bmim Br and b) Hmim Br from proton Larmor frequencies of 30 MHz to 0.01 MHz. The dashed lines are eye guides.

The measurements for Bmim Br are done from above its melting point (≈ 350 K). At high temperatures the relaxation curves show almost no dispersion. The dynamics of molecules at such temperatures are much faster than the dynamic time scale of the field-cycling NMR technique. By lowering the temperature from the melting temperature Bmim Br remains in liquid phase and it is considered as the supercooled state. Slight dispersions start to appear from high frequency regime and are shifted to lower Larmor frequencies by decreasing temperature. This indicates that the characteristic dynamic times of molecules systematically become shorter by decreasing temperature. A decay of three orders of magnitude in the frequency dependent T_1 relaxation times is observed for the temperature range between T_m and 256 K. It should be mentioned here that, although Bmim Br does not show any crystallization upon cooling until T_g in the DSC thermograms in Fig. 5.1 under the experimental condition and using 10 mm NMR tubes, the crystal formation starts during the long measurement times at temperatures below 268 K. Therefore, Bmim Br samples were prepared in capillary tubes (1 mm ID) for low temperature measurements.

Hmim Br remains in liquid phase at the measurement conditions and experiences no crystallization and hence, no melting transition. The field-cycling T_1 measurements are done from temperature 322 K down to 263 K. The $T_1(\omega)$ decay ranges of these ILs are similar with a difference that Hmim Br shows slightly more dispersion at equal temperatures than Bmim Br. At low frequencies ($\omega\tau < 1$ limit) for all temperatures for Hmim Br and Bmim Br, T_1 relaxations become almost field independent and the T_1 plateau values decrease by lowering temperature, Fig. 5.2.

The temperature dependence of T_1 relaxation times are depicted in the Arrhenius plots in Fig. 5.3. Bmim Br shows a shallow minimum at 30 MHz that shifts to lower temperatures at lower fields. Similar behaviour is observed for Hmim Br although the minimum at 30 MHz is not clear due to the lack of measurement data at higher temperatures. The minimum in T_1 is clearly seen for lower fields. These minimums are broad and somewhat symmetric with no discontinuity. The T_1 values below 1 ms (for low fields) follow the tendency well and this supports the validity of measurements of the fast relaxation rates. The measurements at much lower temperatures were not performed because of the low signal-to-noise ratio of the recorded magnetization at fields where the plateau of the $T_1(\omega)$ appears.

5.3 Fittings of T_1 Dispersion Profiles

To understand the molecular dynamic properties of Bmim Br and Hmim Br from their relaxation dispersion data it is necessary to fit the profiles with an appropriate model. Cations in these ILs contain the NMR active nuclei, ^{1}H, that have dipolar moments and in the absence of paramagnetic relaxing agents the most dominant mechanism for proton relaxation is the dipole-dipole interaction. The Br anions do not contribute to the dipolar relaxation of protons. Therefore, cations will interact with each other and this is the main relaxation mechanism. In such a case, both intra- (rotational) and intermolecular (translational) dipolar interactions will be of homonuclear type.

Taking the homonuclear rotational and translational relaxation contributions from Eqs. (2.26) and (2.27) it is possible to fit the experimental T_1 relaxation dispersion profiles. The findings of the modified strategy-2 in Section 4.3.3 will be used here in a different way. The dipolar coupling constants of rotational k_R and translational k_T type, Eqs. (4.2) and (4.4) respectively, can be correlated to each other and the result can be considered as the boundary condition in the fitting program (Section 8). Defining suitable boundary conditions make fittings easier, faster, and yield to an additional parameter which will be presented in the following.

By dividing the k_R to k_T and knowing the number densities of proton in Bmim Br and Hmim Br, the condition by which the coupling constants are bounded to each other is found as following

$$\frac{k_\mathrm{T}}{k_\mathrm{R}} = \frac{\gamma_\mathrm{H}^4 \hbar^2 \frac{3}{10} \frac{N_\mathrm{H}}{\zeta_\mathrm{HH}^3}}{\gamma_\mathrm{H}^4 \hbar^2 \frac{3}{10 r_\mathrm{H}^6}} = 6\pi N_\mathrm{H} \frac{r_\mathrm{H}^6}{\zeta_\mathrm{HH}^3}, \qquad \begin{cases} N_{\mathrm{H,\ 20^\circ C}}^{\mathrm{Bmim\ Br}} = 5.360 \times 10^{28}\ \left({}^{1\mathrm{H}}/_{\mathrm{m}^3}\right) \\ N_{\mathrm{H,\ 20^\circ C}}^{\mathrm{Hmim\ Br}} = 5.592 \times 10^{28}\ \left({}^{1\mathrm{H}}/_{\mathrm{m}^3}\right) \end{cases} \tag{5.1}$$

The ratio $r_\mathrm{H}^6/\zeta_\mathrm{HH}^3$ becomes a new fitting parameter for each IL. Therefore, by assuming radius values r for cations, the minimum distance of approach values ζ can be calculated for the cations of both ILs. Figures 5.4 and 5.5 show the translational and rotational correlation times of Bmim Br and Hmim Br, respectively, obtained from fittings. The translational correlation times for both ILs from room temperature down to around 273 K show a temperature dependence that could be considered as Arrhenius type. Since these ILs are glass forming liquids and they are in the metastable phase, it is possible to also consider this kind of temperature dependence as a weak VFT behaviour that is usual for strong glass formers/ILs. The solid lines on figures show the linear fit for Bmim Br which is also included in the Hmim Br figure as a comparison of the slope differences. It is seen that the τ_T of Hmim Br has a slightly weaker temperature dependence. In the τ_T Arrhenius plots of both ILs deviations from higher temperature trends are seen at around a temperature between 278 K and 273 K. Below this temperature τ_T values take shallower temperature dependences.

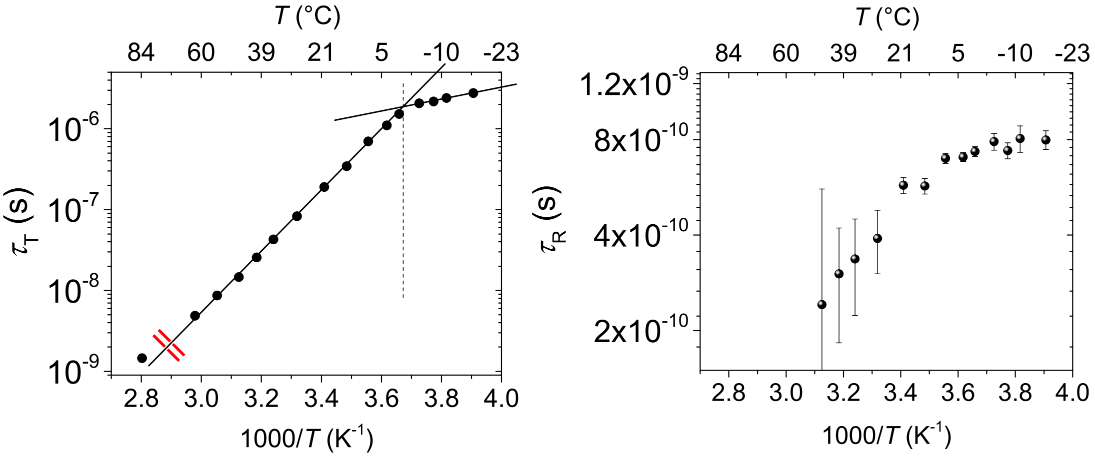

(a) (b)

Figure 5.4: Fitting results of the T_1 relaxation dispersion curves of Bmim Br: a) translational and b) rotational correlation times. The lines are linear fits to the data as eye guides. The vertical line shows the change of tendency temperature.

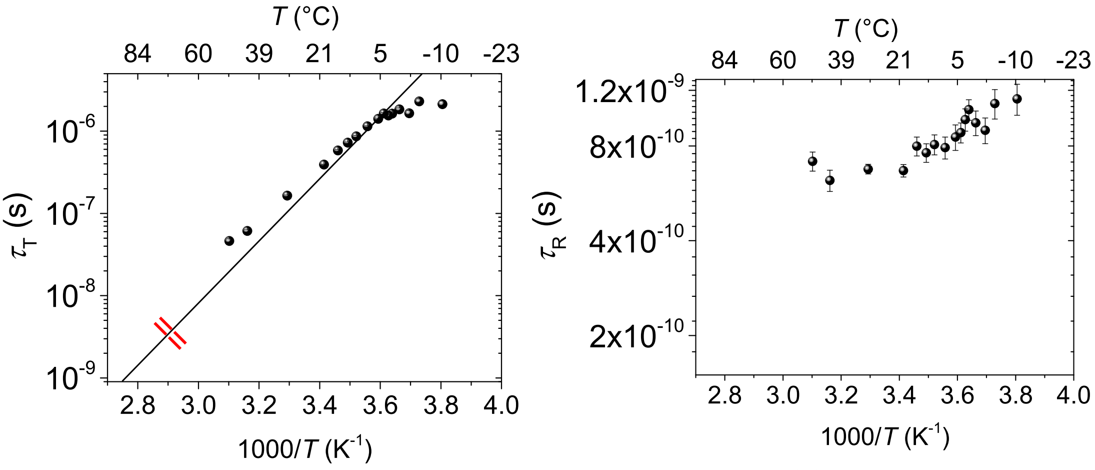

(a) (b)

Figure 5.5: Fitting results of the T_1 relaxation dispersion curves of Hmim Br: a) translational and b) rotational correlation times. The solid line on (a) is the linear fit for the Bmim Br data shown on Fig. 5.4a used here as a comparison of the temperature dependence slope.

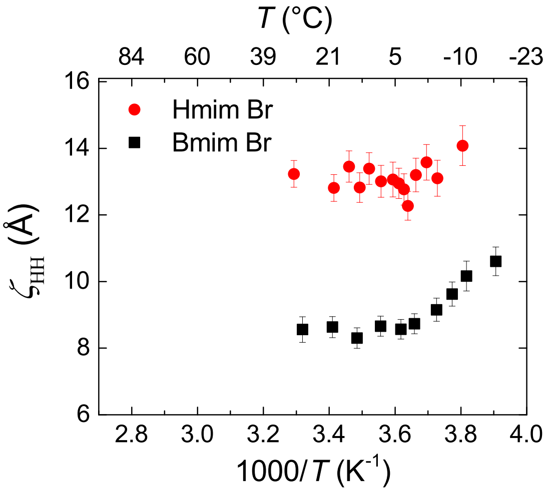

Figure 5.6: The minimum distance of approach values of cation-cation obtained from the fittings of T_1 dispersion curves for Bmim Br (black) and Hmim Br (red).

Rotational dynamics of these ILs, unlike the translational dynamics, could not be obtained much satisfactorily from fittings. That means, only at low temperatures the contribution of intramolecular interactions to the total T_1 relaxation could be fitted while at higher temperatures this contribution was found to play a weaker role. As a result, τ_R values either could not be obtained, or obtained with large uncertainties. However, the τ_R values of low temperature regime show very weak temperature dependences and they do not show any deviation at low temperatures as is seen for τ_T. Still the relatively larger error bars below the cross over temperature might be related to the deviation in the temperature dependence of the rotational dynamics.

Besides the τ_T and τ_R parameters obtained directly by applying the translational and rotational model of molecular motion, an additional parameter, the minimum distance of approach ζ, can be obtained as a result of Eq. (5.1). By assuming r to be equal to the van der Waals radii of Bmim and Hmim molecules 3.03 Å and 3.53 Å[76], respectively, the ζ values are calculated and shown in Fig. 5.6.

The minimum distance of approach value obtained for Bmim Br at room temperature is about 8.3 Å, and increases to 10 Å at 256 K. The increase of ζ can be interpreted as the increase of size of the mobile species at decreased temperatures, i.e. cooperative motion of molecules. Interestingly, the ζ_{HH} values calculated for Hmim Br are found to be independent of temperature and show to be approximately 13 Å for the temperature range between 323 K and 263 K.

5.4 Self-Diffusion

Translational motions of cation molecules in Bmim Br and Hmim Br are investigated by different techniques. First the direct measurements of the self-diffusion of the proton carrying species in the ILs will be presented. Next the transport prop-

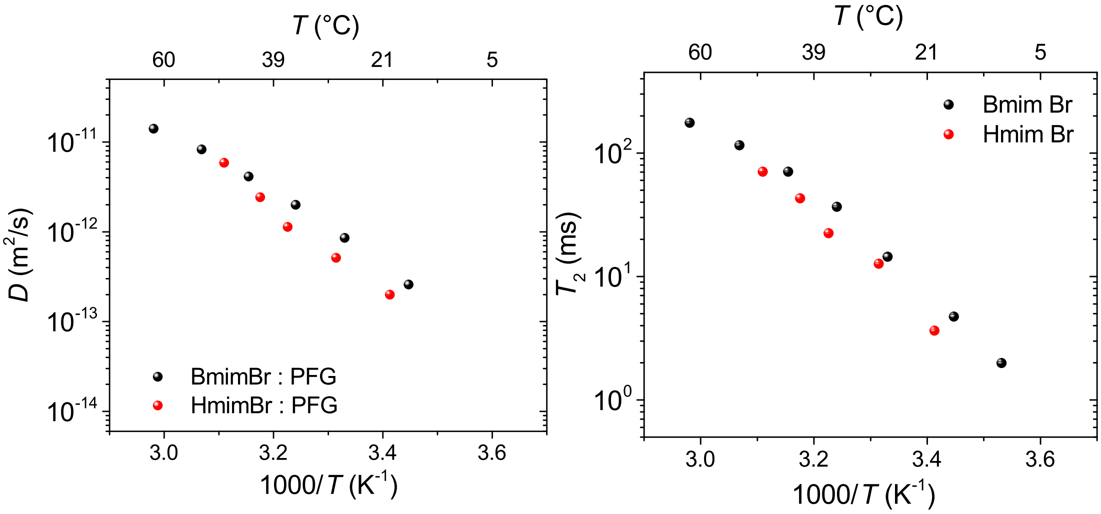

(a)

(b)

Figure 5.7: Arrhenius plots of a) self-diffusion coefficients obtained from PFG-NMR and b) T_2 times of the supercooled Bmim Br and Hmim Br ILs.

erties calculated from the T_1 relaxation profile fits will be provided and at last, the self-diffusion constants calculated from the frequency dependence of the spin-lattice relaxation rates at the low frequency limit will be given.

Pulsed field gradient NMR enables the direct self-diffusion coefficient measurements. The effort was taken to perform these experiments covering the same temperature ranges of the field-cycling relaxation measurements. The results are shown in Fig. 5.7a

Bmim cations are smaller in size than Hmim (by two carbons). Based on the Stokes-Einstein equation, larger particles diffuse slower. As seen in Fig. 5.7a Bmim molecules diffuse slightly faster than Hmim cations. However, at a high temperature of 322 K the self-diffusion values approach to similar values.

At the lowest measured temperatures for Bmim Br and Hmim Br the diffusion measurements are limited not only because of the hardware (gradient strength) limitations, but also due to the sharp decrease of the spin-spin relaxation times T_2 of the deeply supercooled ILs.

At the low temperature limit of the self-diffusion experiments, Bmim Br reaches a diffusion constant of $9.5 \times 10^{-14}\,\mathrm{m^2\,s^{-1}}$ at 283 K and this is the low limit of the diffusion probe gradient used in this experiment. The lowest temperature and diffusion constant for Hmim Br does not reach the low limit of the diffusion probe and is limited by the rapid decrease of T_2 of the bulk sample at low temperatures. Figure 5.7b shows the proton T_2 data at different temperatures for ILs measured at 300 MHz (proton Larmor frequency).

The second method to obtain the diffusion coefficients is to use the translational correlation times obtained from fittings of the T_1 relaxation profiles. This method can be seen as a check-of-validity of the theoretical NMR relaxation model used in

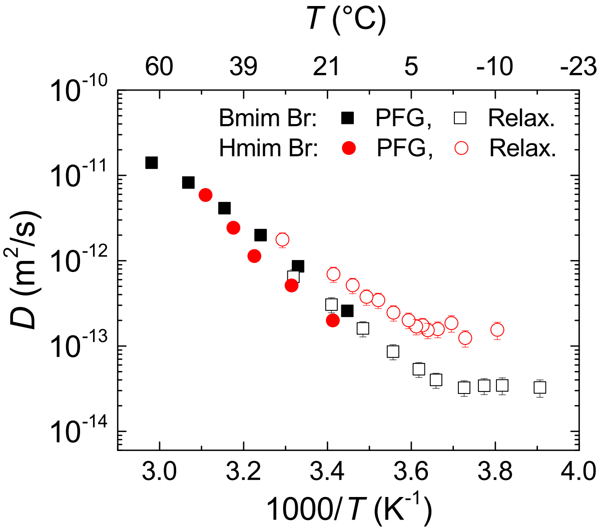

Figure 5.8: Comparison of the self-diffusion coefficients obtained directly from PFG-NMR (solid symbols) and calculated from the translational correlation times (empty symbols) – using the data of Figs. 5.4 to 5.6 – for Bmim Br (black) and Hmim Br (red).

Section 5.3. Using the relation $D = \zeta^2/2\tau_\mathrm{T}$ and by taking the minimum distance of approach values from Fig. 5.6 and τ_T values from Figs. 5.4a and 5.5a the diffusion constants are calculable.

Figure 5.8 compares the result of these calculations with the direct self-diffusion measurement data for Bmim Br and Hmim Br. The temperature range available from the relaxation data is broader and the calculated diffusion values reach lower temperatures where the PFG experiments fail due to the apparatus limitations and/or fast transverse relaxations. The diffusion values obtained from relaxation dispersion match with the PFG-NMR results within the orders of magnitude. The temperature dependence of the self-diffusion data for Bmim Br in Fig. 5.8 show a slight deviation from the Arrhenius behaviour. However, transport properties of Hmim Br show more Arrhenius-like temperature dependence (Fig. 5.8). The diffusion range is well extended to lower temperatures (and $D < 10^{-13}\,\mathrm{m}^2\,\mathrm{s}^{-1}$) by the relaxation method for both ILs. Therefore, the crossover temperature that was seen in the translational correlation times in Fig. 5.4 show up again. Below this temperature deviations from the high temperature diffusion trends are visible.

The third method of estimating the self-diffusion constants is based on the fact that at low-frequency limit the rotational spectral density gets frequency independent. Therefore, assuming that no other relaxation mechanism plays a significant role, the spin lattice relaxation is controlled by the intermolecular interactions. Some theoretical models of liquids have been developed in the classical literature for the interpretation of the experimental data at this limit although some inevitable approximations have been considered by each model which introduce uncertainties[93–96]. At low frequency limit (usually $\omega\tau < 1$ and $\omega\tau > 10^{-4}$)[95] the intermolecular relaxation contribution is not frequency independent. The intermolecular correlation function takes the form of a power law ($\propto t^{-3/2}$) and the spectral density obtained by each of these models is in the form of

$$J(\omega) = J(0) - f(D, \sqrt{\omega}), \tag{5.2}$$

where the $J(0)$ term is model dependent while the second term is not and is used to interpret the spin lattice relaxation data[94]. The frequency range condition for the validity of these theories can be easily assessed from relaxation dispersion curve fittings. Following Harmon[95,96], if the spin-lattice relaxation rate is plotted as a function of $\sqrt{\omega}$, the slope of the linear fit will be diffusion dependent

$$R_1(\omega) = R(0) - \overbrace{\left(\frac{\mu_0}{4\pi}\right)^2 \frac{8\pi N\gamma^4\hbar^2 I(I+1)0.555}{15\, D^{3/2}}}^{\text{Slope}} \sqrt{\omega}. \tag{5.3}$$

The low frequency fits are shown for Bmim Br and Hmim Br in Fig. 5.9. The higher temperature spin-lattice relaxation rates R_1 (bottom plots) show clear linear behaviours at low frequencies while the error values of the measured data at low temperature R_1 curves (top plots) increase. The diffusion coefficients are calculated by taking the slopes of the linear fittings and substituting in Eq. (5.3). The outcome diffusion constants are shown in Fig. 5.10 and compared with the diffusion constants obtained previously. These diffusion constants show good agreements with the direct diffusion measurements (PFG) and the relaxation dispersion model. The small differences could correspond to different assumptions and approximations used in each of the fitting methods.

5.5 Crystallized Bmim Br

From the DSC thermogram of Fig 5.1 it is seen that Hmim Br does not crystallize in the mentioned experimental condition. Bmim Br, however, upon heating from glass transition temperature goes under cold-crystallization. Bmim Br crystals were prepared by quenching the Bmim Br (in a 10 mm NMR tube) in liquid nitrogen and bringing it back to room temperature and repeating until complete crystals were formed. The NMR spectra confirms the line broadening and no existence of liquid phase (at least macroscopic).

The crystal sample then is used for the diffusion measurements from slightly below T_m down to 252 K. The results are shown in Fig. 5.11b. Surprisingly, the diffusion coefficients of the solid sample are seen to be significantly higher than the supercooled liquid and the differences increase rapidly at lower temperatures. The T_1 and T_2 data for the solid sample are given in Fig. 5.11a. T_1 values at temperatures near the melting point are one order of magnitude longer than the T_2. T_1 times show a broad minimum at 272 K while T_2 times continuously decrease towards low temperatures. The decreasing trend of the T_2 relaxation times is changed to be stronger starting from about 263 K and reaches about 4.3 ms at 233 K (data not shown on the figure).

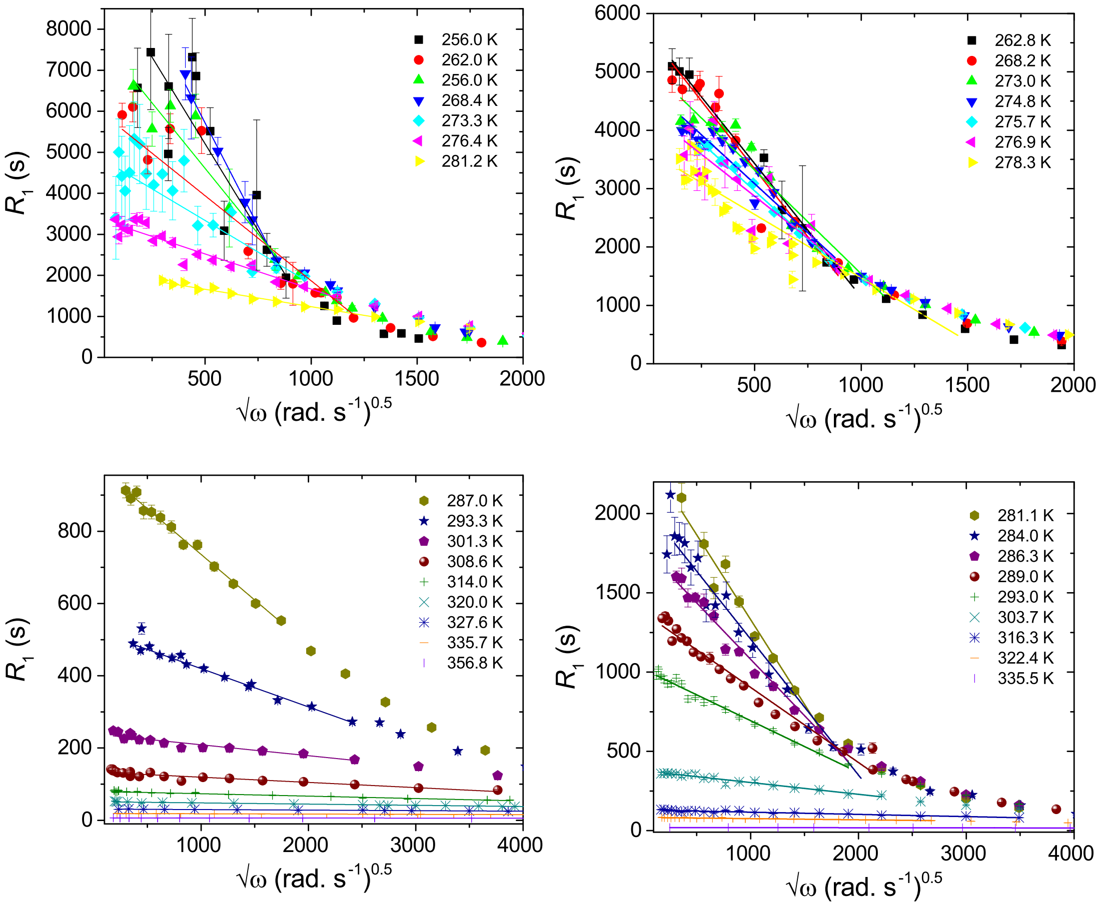

(a) Bmim Br

(b) Hmim Br

Figure 5.9: ^{1}H spin-lattice relaxation rates R_1 as a function of $\sqrt{\omega}$ for a) Bmim Br and b) Hmim Br at low temperatures (top plots) and high temperatures (bottom plots). The solid lines are linear fits based on Eq. (5.3)

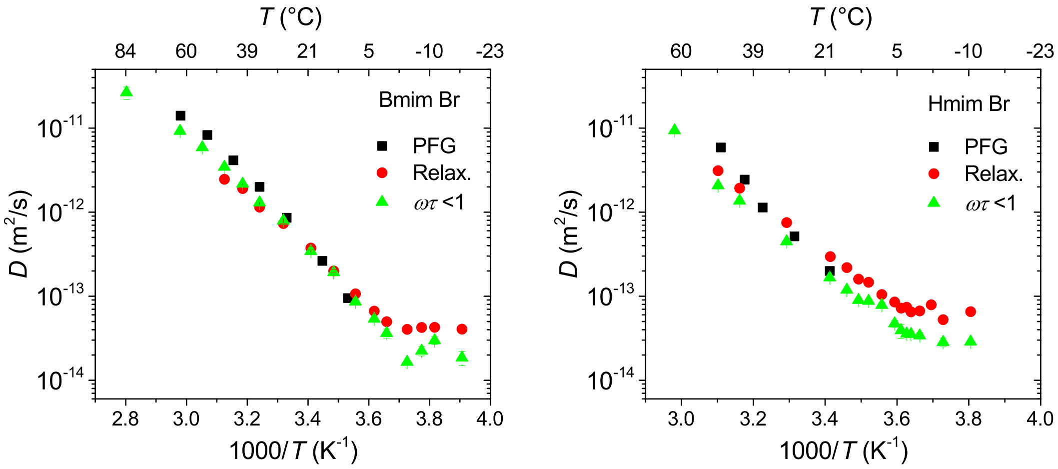

Figure 5.10: Comparison of the self-diffusion coefficients estimated from three different methods for a) Bmim Br and b) Hmim Br.

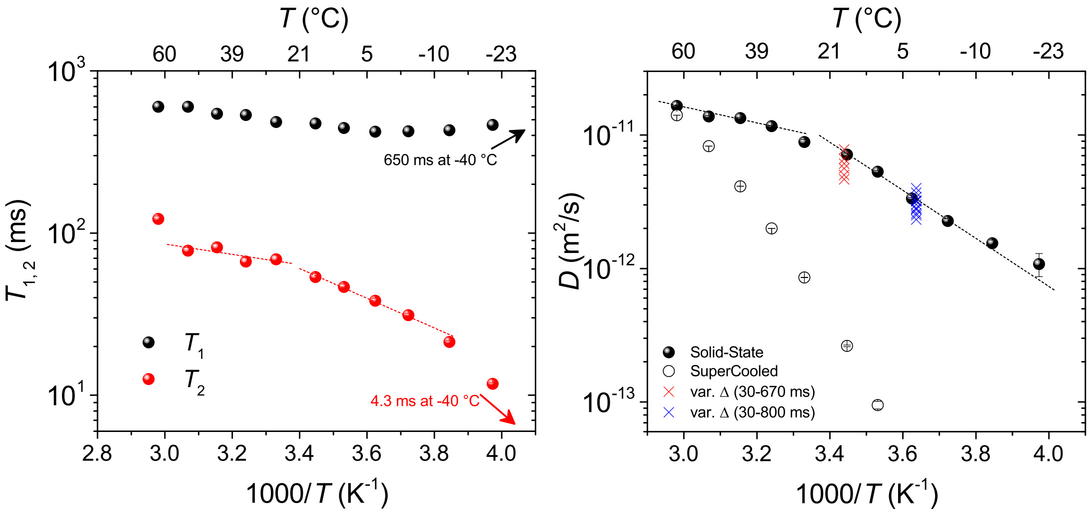

(a) (b)

Figure 5.11: a) T_1 and T_2 Arrhenius plots of the crystallized Bmim Br sample, b) self-diffusion values of Bmim Br in supercooled state (empty circles) and crystallized (full circles). The red and blue crosses show the variations of diffusion coefficients by varying the diffusion time Δ. The range of variation of Δ times are given in the legend. The lines on both plots are guides to the eye.

Comparing the Arrhenius plots of the T_2 relaxation times and self-diffusion constants in Fig. 5.11 a similar change of temperature-dependence is seen around 295 K for both. The time dependence of the diffusion coefficients in the solid-state sample was checked with different diffusion times (Δ time in STE-PFG pulse sequence) at 290 K (red crosses) and 271 K (blue crosses) in Fig. 5.11b.

5.6 Discussion

The three imidazolium based ILs with bromide anions that were used for the thermal analysis differ only at the alkyl chain length each by two carbons stepwise (ethyl, butyl, and hexyl). However, each of them show distinct thermal behaviours, e.g. supercooling ability and crystallization process. The reason of such behaviour can be explained as following. Melting is a one-step process that is controlled thermodynamically. Crystallization, however, is more complicated and is a two-step process controlled kinetically and thermodynamically. Liquids that are cooled below their melting points are not anymore considered as homogeneous molecular systems, but they are in the metastable phase. The local molecular fluctuations of the macroscopic properties of the system, e.g. density, are more likely to yield to the formation of stable clusters in the metastable phase which can grow subsequently if they reach a certain critical size. In homogeneous liquids, however, the clusters which are formed as a result of density fluctuations are instantaneously dissociated. At sufficient undercooling, the rate of association is larger that the rate of dissociation and therefore nucleation, which is the first step of crystallization, takes place. Thermodynamically speaking, nucleation is favoured at low temperatures since the critical cluster size (the minimum molecular aggregation to form stable clusters) is smaller and therefore, the Gibbs energy barrier for nucleation is smaller. However, at low temperatures and approaching the glass transition the molecular motion is extremely slow due to the high viscosity. Therefore, cluster formation is kinetically unfavoured. In principle, there should be a certain range of temperature between T_g and T_m that nucleation can be favoured by both thermodynamics and kinetics. The second step of crystallization is the crystal growth that should be followed by nucleation. This process as well requires a certain temperature range to act efficiently[97].

The crystallization condition for Emim Br is met at about 70 degrees below its T_m. This is the point where the possibility of the nucleation and crystal growth processes overlap and lead to a sharp exothermic transition. Bmim Br sample experiences no crystallization at cooling cycle and only goes under a cold-crystallization at heating process. One possible explanation could be that the crystal growth process is favoured at a temperature range higher than the nucleation step. Therefore, upon cooling the sample from the melting point the crystal growth temperature range is reached before the nucleation and clearly no crystal formation happens. At lower temperatures, however, the nucleation begins but the crystal growth at this point is kinetically not plausible and consequently the liquid quenches to glass at lower temperatures. Upon heating from T_g, the previously formed nuclei survive and reach the temperature where crystal growth can efficiently occur. This leads to the exothermic transition seen in Fig. 5.1, the cold-crystallization. At higher temperatures the formed crystals melt (T_m).

For the case of Hmim Br where no crystallization is observed, two scenarios are possible. First: nucleation takes place at cooling (like Bmim Br), but at the heating cycle the nuclei can not resist to reach the crystal growing temperature and hence, dissociate. Second: due to the longer alkyl chain of the Hmim Br, some restrictive stereochemical requirements make crystallization inefficient. In simple words, the packing of Hmim Br is spatially hindered.

The molecular dynamics properties of Bmim and Hmim molecules lie in the same time scale range over the measured temperatures. The transport properties (τ_T) obtained from the relaxation time analysis follow Arrhenius temperature dependences for both ILs (Figs. 5.4a and 5.5a) while the self-diffusion coefficients show to be of shallow VFT type for Bmim Br (Fig. 5.7a). Interestingly, by considering the minimum distance of approach ζ_HH values for the calculation of diffusion constants from τ_T in Bmim Br, the Arrhenius temperatures dependence of τ_T turns to a VFT type dependence in the diffusion constants. Hmim Br shows Arrhenius type behaviours both in $\tau_\mathrm{T}(T)$ and $D(T)$, and the minimum distance of approach values do no show any noticeable temperature dependence.

Weak deviations from Arrhenius behaviour is a key property of the so-called “strong” glass former liquids that is clearly seen in Bmim Br. However, although the diffusion constants by two methods of T_1 relaxation and PFG-NMR show good agreements in the narrow temperature range (Fig. 5.8), they cannot be fitted by the VFT equation using a single set of parameters. The PFG-NMR and spin-lattice NMR relaxation methods give information on the transport properties of the liquid but relaxation methods provide microscopic details of the translational motion which is not determined by the pure self-diffusion techniques. It is already known that the VFT fitting parameters are technique and temperature-range dependent[68]. The temperature range is important in defining the type of temperature dependence. For Hmim Br, although there is a two-decade diffusion coefficient change in the PFG-NMR data, the temperature variation range is small and it makes the definition of type of dependence difficult. In other words, there might be a strong VFT dependence, but due to the shorter temperature range it is seen to be Arrhenius like. The analysis of the low frequency limit of the relaxation rates R_1 for both ILs can also successfully estimate the diffusion constants.

The self-diffusion data are well extended to lower temperatures by the NMR relaxation methods where PFG-NMR cannot reach due to the apparatus limitations. The diffusion coefficients calculated from the relaxation time analysis for both ILs at low temperatures show deviations from the high temperature trends and become less temperature dependent. It is necessary to check the T_1 dispersion data and the fitting qualities at low frequencies. The T_1 relaxation times, Fig. 5.2, at frequencies lower than 100 kHz for temperatures below 265 K and 293 K, respectively for Bmim Br and Hmim Br, fall below 1 ms range. At much lower temperatures the T_1 times reach even much lower values of about 100 µs. That means, the relaxation times at low fields are smaller than the field switching times of the field-cycling technique, see Section 3.4. The T_1 measurement in such condition is not usual in the routine field-cycling experiments where T_1 relaxation times are at least larger than several milliseconds.

The barrier of T_1values smaller than 1 ms brings up the question of reliability and reproducibility of the measured relaxation times. Previous investigations by Ferrante and Sykora has tackled the challenging case where the field-switching times become close-to or longer than the relaxation times[98]. They found that for samples which show strong dispersions in the T_1 relaxation profiles, the measurement of T_1 times as low as 100 µs is easily achievable by the automation in the field-cycling instrument, i.e. no slew-rate optimization for each relaxing field is required. In fact, samples that relax fast at low frequencies, e.g. 1 MHz, are not subject to the problem of relaxation during the switching interval. Moreover, even if the field switching involves very low fields, the sample is exposed to the low-field relaxation only for a small fraction of the switching time, i.e. 10 % or less[98,99]. In such cases, the main problem arises from the loss of sensitivity due to the high spin-lattice relaxation rates especially at low frequency region and it does not cause any systematic experimental errors[46].

The relaxation times that lie below 1 ms in Fig. 5.2 were measured using a shorter switching time (2 ms instead of 2.4 ms). This considerably increased the quality of the magnetization build-up curve. The magnetization recovery curves for the relaxation times less than a millisecond are analysed individually to assure the mono-exponential decay quality. Although the magnetization decays less than one order of magnitude, the mono-exponential decay quality is satisfactory. Even though, relatively large uncertainties exist in T_1 estimation at this range due to the low signal-to-noise ratio and small decay range. Also the Arrhenius plots of T_1 in Fig. 5.3 show reasonable tendencies of T_1 at low temperature/frequencies. Therefore, the fitting results for low temperatures are reliable and the deviation of the transport properties of both ILs can be associated to the crossover temperature T_c which is generally reported for the molecular glass forming liquids. Such a crossover temperature has not been reported for these ILs to the best of our knowledge. Direct self-diffusion measurements have been reported by Kremer's group for Bmim Br in the range of 310 K to 250 K[100], which are similar to the results in the current study. But the lower temperature diffusion values were only calculated from the broadband dielectric spectroscopy measurements using the Einstein-Smoluchowski equation, $\sigma_0 = (nq^2/kT)D = (nq^2/kT)(\lambda^2/2\tau_\mathrm{h})$, assuming an effective number density of ions n contributing in the ion conduction, a hopping length λ and time τ_h. The dc conductivity σ_0 observes the micrometer scale motions of ions and assumes a fraction of ions contributing in the conduction. Although the dielectric spectroscopic methods can give information on the shorter dynamic time scales of the molecular motion and conduction mechanism at high frequencies where the complex conductivity becomes dispersive, the dc conductivity does not contain any molecular scale dynamics but a micrometer or longer scale. Furthermore, the conductivity methods do not differentiate between different molecular aggregations and considers only the charged ions/aggregates. The aggregation behaviour is temperature dependent and might not follow an Arrhenius behaviour. The calculation of diffusion coefficients by these authors is based on the assumption of the ideal behaviour of ILs at a broad temperature range while the NMR relaxation results in the current study show that ILs do not behave ideally at deeply supercooled temperatures. The crossover dynamic temperature T_c happens at a temperature around $1.2\,T_\mathrm{g}$ for Bmim Br and

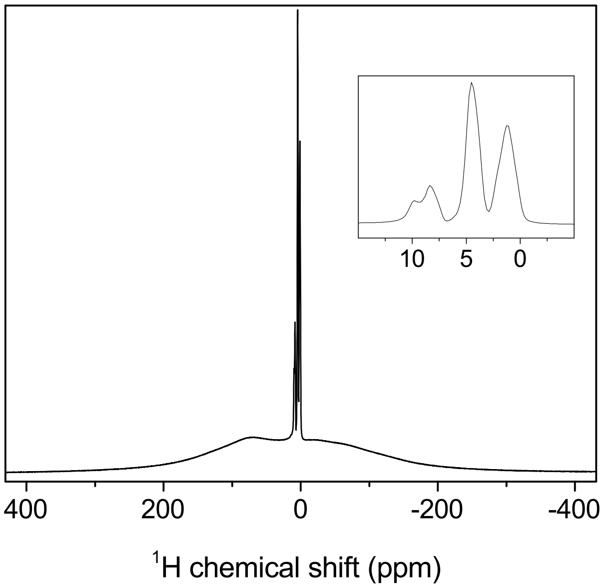

Figure 5.12: ^{1}H-NMR spectrum of Bmim Br in solid-states at 275 K. The inset shows the sharper peaks on top of the broad solid signal.

Hmim Br, which is a well known behaviour of the glass forming molecular liquids.

The faster self-diffusion coefficient of Bmim Br in the crystalline state than the supercooled liquid is controversial, Fig. 5.11. Similar observations were reported before by Every et al. for Emim Br and Emim I[101]. By comparison of the PFG-NMR and conductivity results, these authors concluded that the fast cation diffusion in crystals are a result of the vacancy diffusion process facilitated by the cation's rotational motion similar to molecular plastic crystals. Although they also did not measure directly the diffusion of the bromide anions, they assumed that the cations are the only mobile species responsible for the ion conduction. But a recent study by Endo et al. revealed completely different results[102]. It was proposed that very low water content (200 ppm) in the Bmim Br is responsible for the fast cation diffusion in the crystal form. This amount of water in the hygroscopic room temperature IL samples is not observable by the high resolution NMR spectroscopy and the IL sample, in most cases, is regarded as pure enough. Based on Endo's study, the fast cation diffusion in the solid-states (Fig. 5.11b) can be explained as following. The ^{1}H-NMR spectrum of the solid sample is shown in Fig. 5.12. The broad peak is the overlap of proton signals in the solid that are broadened by the strong dipole-dipole interactions. The small sharp peaks at top of the broad peak were found to be proportional to the water content of Bmim Br while the chemical shift pattern of these peaks corresponds to the proton spectrum of Bmim Br. The narrow lines in the spectrum show that a small fraction of Bmim Br molecules are in a liquid-like phase that are relatively mobile and can average out dipolar couplings. In fact, the concentration of water in the tiny liquid-like phase is much higher and this provides the higher mobility in this phase. At higher temperatures and approaching the melting point of Bmim Br, the area ratio of the sharp peaks increase and after the T_m no broad peak exists anymore. This discussion of Endo et al. should be examined employing ultra-high vacuum drying ovens, Carl-Fischer experiments, and NMR spectroscopy.

Chapter 6

Ionic Liquids in Porous Media

In this chapter the Bmim Tf2N ionic liquid is selected to study the confinement effects on the dynamics. Although the nano-confinement brings extra complexities, emerging applications of ionic liquids in composites and porous media necessitates more understanding of their dynamics in restricted geometries. Here the results and analysis of the stimulated echo PFG diffusometry and field-cycling relaxometry experiments are presented.

6.1 Self-Diffusion

The translational dynamics of cations in Bmim Tf2N confined in porous Vycor glass were measured at a broad temperature range from 308 K to 248 K, Fig. 6.1a. The self-diffusion values in confinement are about one order of magnitude smaller than the values in bulk. Considering the diffusion time (Δ) which was selected to be between 100 ms and 350 ms, the diffusion length – taking the mean square displacement in Eq. (2.45) – of the cation molecule in the bulk phase at room temperature is obtained as $x = 2.8\,\mu\mathrm{m}$ to $5.2\,\mu\mathrm{m}$. At the lowest measured temperature for the bulk the MSD is calculated to be $x = 120\,\mathrm{nm}$ to $235\,\mathrm{nm}$. Therefore, at all the measured temperatures the MSD is much larger than the pore diameter of the porous media (4 nm) and the diffusion of the IL inside Vycor is restricted. Figure 6.1b shows the logarithmic echo attenuation decays for all the measurements which show monotonic exponential behaviours although for lower temperatures complete decays could not be obtained.

Figure 6.2 shows the ^{1}H-NMR spectra of confined Bmim Tf2N at different temperatures. Wide NMR lines even at room temperature are observed which correspond to the non-averaged effect of the dipole-dipole interactions of nuclei as a result of confinement. At lower temperatures the lines get broader while no chemical shift change is observed.

6.2 Field-Cycling NMR Relaxometry

The T_1 relaxation times at varying magnetic field strengths were measured by the field-cycling relaxometer at a temperature range from room temperature to 208 K. All T_1 magnetization recovery curves could be well expressed by the monoexponential

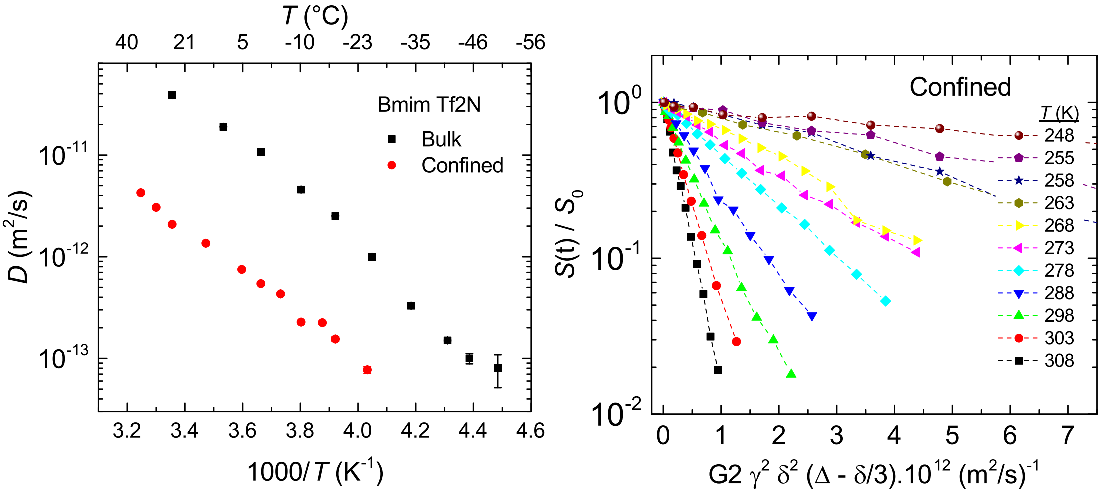

(a) (b)

Figure 6.1: a) Self-diffusion coefficients of bulk (black) and confined (red) Bmim Tf2N. b) Echo attenuation decays of the confined IL obtained from the stimulated echo PFG-NMR experiments.

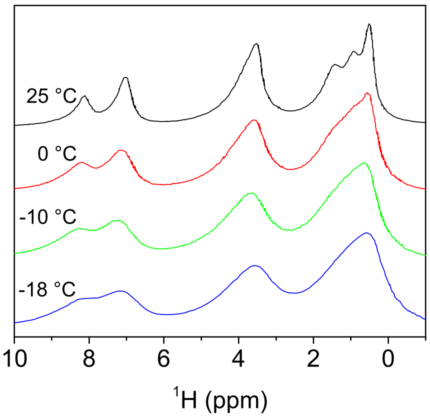

Figure 6.2: ^{1}H-NMR spectra of the Bmim Tf2N IL confined in Vycor glass measured from room temperature down to 255 K.

function. Figures 6.3a and 6.3b show the ^{1}H- and ^{19}F-$T_1(\omega)$ of Bmim Tf2N confined in Vycor. Strong dispersions are seen for both nuclei at all temperatures. The $T_1(\omega)$ curves follow a power law tendency of $T_1 \propto \nu^{\gamma}$ whereas the T_1 values at a fixed frequency, for example at 1 MHz, decrease slightly by decreasing temperature. This trend is broken starting from and below 223 K where the T_1 values start to increase.

Before rushing to further interpretations, one should recall that this ionic liquid in bulk, Bmim Tf2N in Chapter 4, showed relatively strong T_1 dispersions especially at supercooled temperatures. Therefore, the extreme narrowing condition, which applies to low-viscosity liquids at all conventional magnetic field strengths, is not completely true for the bulk Bmim Tf2N. For this reason, the analysis of $T_1(\omega)$ of Bmim Tf2N confined in Vycor cannot be done without considering the bulk contribution in dispersions. This is contrary to the case of simpler liquids like water or ethanol[51,103,104] where bulk liquids are always in the fast motional limit within the measured magnetic field strengths. The temperature dependence of the T_1 relaxation times of confined Bmim Tf2N can be better seen in the Arrhenius plots shown in Figs. 6.3c and 6.3d. The very broad minimums observed for both nuclei reveal the complex dynamics of cations and anions in the porous media. This means the dynamics of molecules are governed by more than one correlation time. However, the general trend of the $T_1(T)$ for cation and anion looks similar, proposing that the dynamics of these ions, in spite of their different electric charges, might not differ tremendously from each other.

To understand the confinement effects on the dynamics of Bmim Tf2N it is important to consider the results of the bulk Bmim Tf2N in Chapter 4. The first step is to find a frequency-temperature regime that the bulk Bmim Tf2N falls into the fast motion limit $\omega\tau << 1$. The minimums observed in the T_1 Arrhenius plots of bulk Bmim Tf2N (Fig. 4.5b) appear at $\omega\tau \approx 0.6$ (following BPP theory and assuming an average correlation time). Therefore, it is possible to find temperature and relaxation field ranges where the motional narrowing condition holds for bulk Bmim Tf2N (the negative slopes of Arrhenius plots).

The highlighted areas in Fig. 6.4 show the ranges where $\omega\tau << 1$ hold for Bmim (grey) and Tf2N (red). A cross check can be done with the higher relaxation field of 300 MHz (for proton Larmor frequency). From Fig. 6.4 and assuming a single activation energy for the whole temperature range, one would expect that the motional narrowing condition for the relaxation field of 300 MHz should apply at $T > 268$ K. An alternative check method is by calculating the ratio of longitudinal relaxation times to the transverse relaxation times. For an isotropic liquid where the fast motional limit is true, T_1 and T_2 relaxation times should lie within the same range. The T_1, T_2, and the ratio T_1/T_2 values for the bulk and confined Bmim Tf2N at $B_{\text{relax.}} = 300$ MHz are shown in Fig. 6.5 for a wide temperature range. The T_1/T_2 ratio for the bulk IL approaches to about unity at around $T > 293$ K while the confined IL shows much larger ratios even at elevated temperatures. The frequency and temperature ranges where the motional narrowing condition applies for the free IL phase inside the Vycor can be concluded from Figs. 6.4 and 6.5c. Taking the maximum relaxation field of the field-cycling measurements to be 20 MHz (for ^{1}H), from Fig. 6.4 it is safely estimated that for all temperatures above 248 K (and all

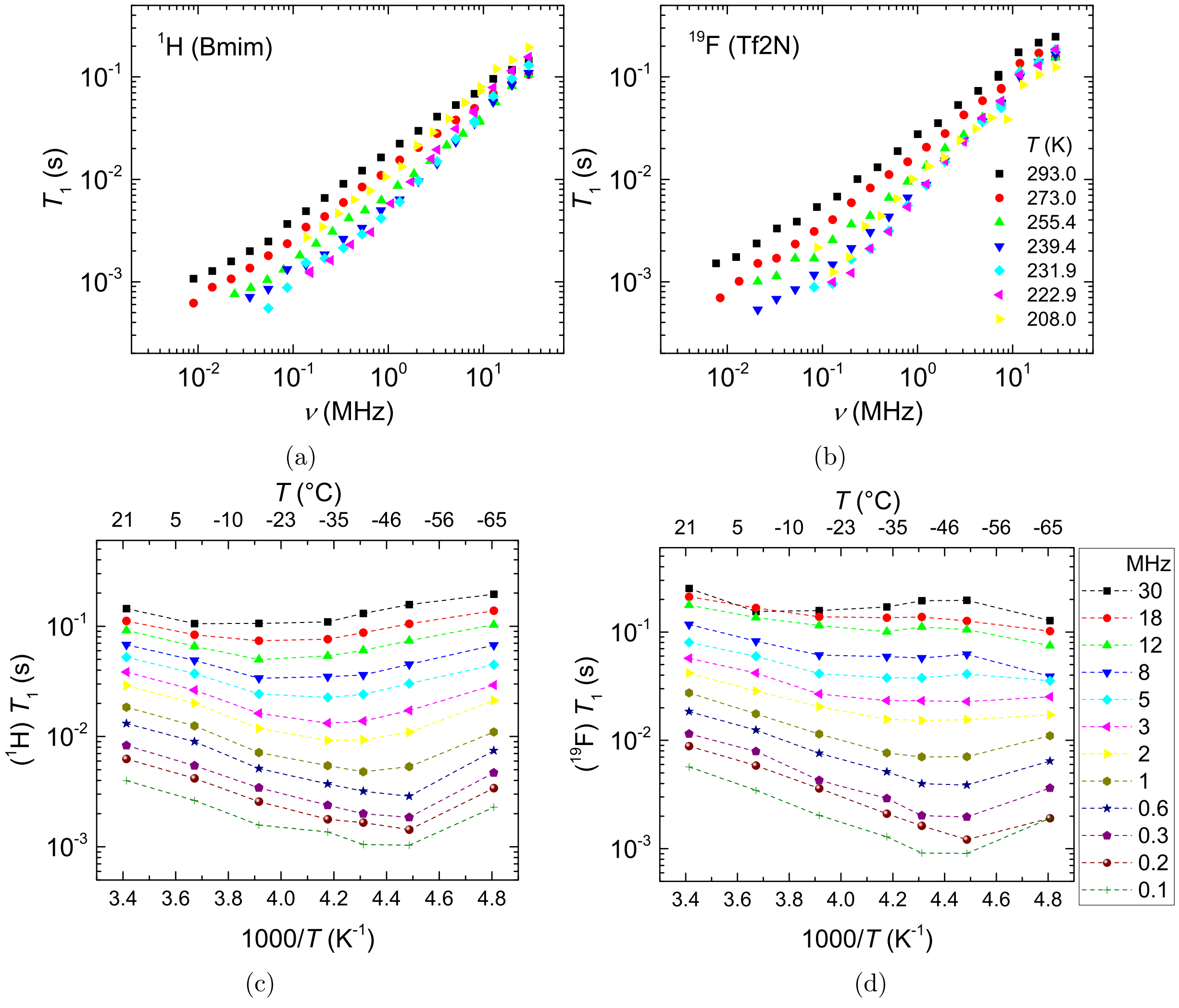

(a)

(b)

(c)

(d)

Figure 6.3: T_1 dispersions of a)^{1}H- and b)^{19}F- , T_1-Arrhenius plots of c)^{1}H- and d)^{19}F- of Bmim Tf2N ionic liquid confined in Vycor measured between 293 K and 208 K.

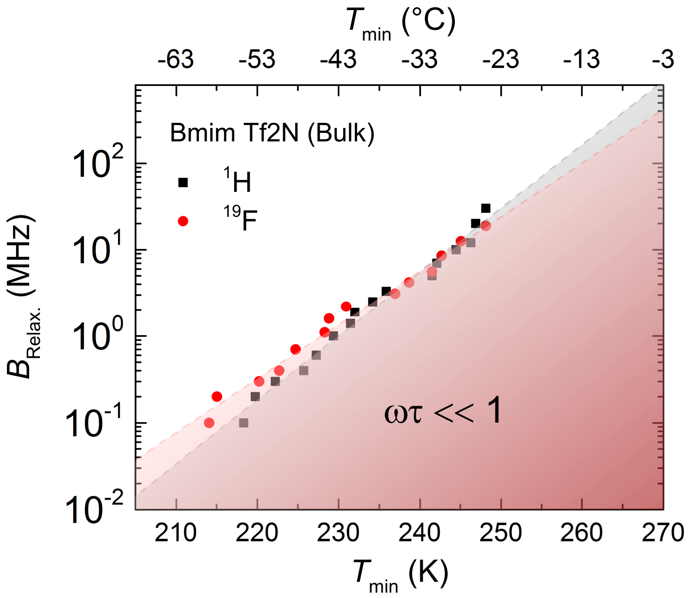

Figure 6.4: The relaxation field vs. temperature plot for the bulk Bmim Tf2N. Each data point on the plot corresponds to the temperature where the T_1 relaxation times at a constant relaxation field reach a minimum in Fig. 4.5b. Black and red symbols represent cations (^{1}H) and anions (^{19}F) and the grey and red highlights respectively show the regions where the motional narrowing condition $\omega\tau << 1$ holds for both nuclei.

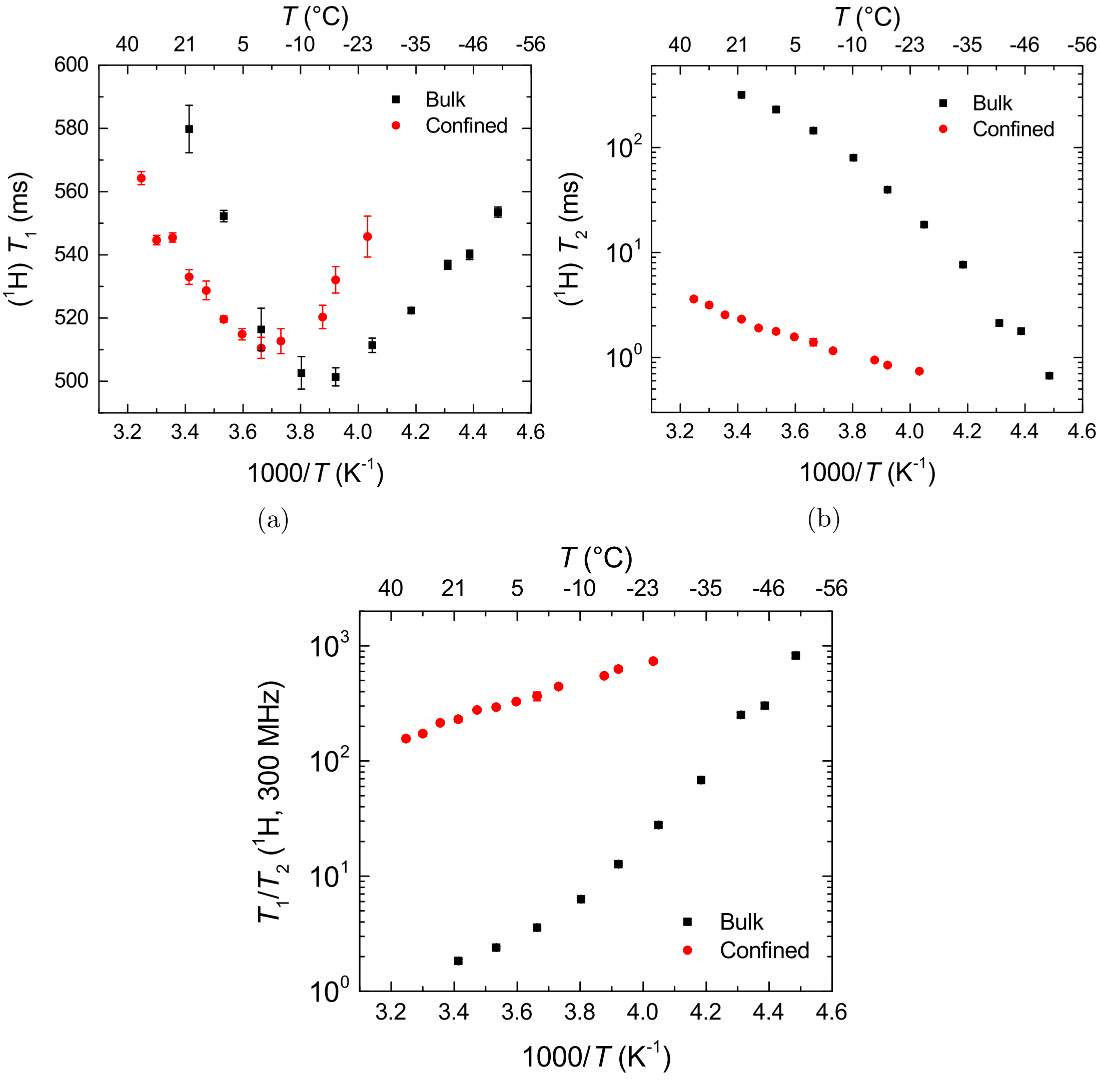

(a)

(b)

(c)

Figure 6.5: Proton a)T_1, b)T_2, and c)T_1/T_2 ratios for the Bmim Tf2N measured at a magnetic field strength of 7.05 T equal to 300 MHz for proton Larmor frequency. Black squared: bulk Bmim Tf2N, red circles: confined Bmim Tf2N in Vycor.

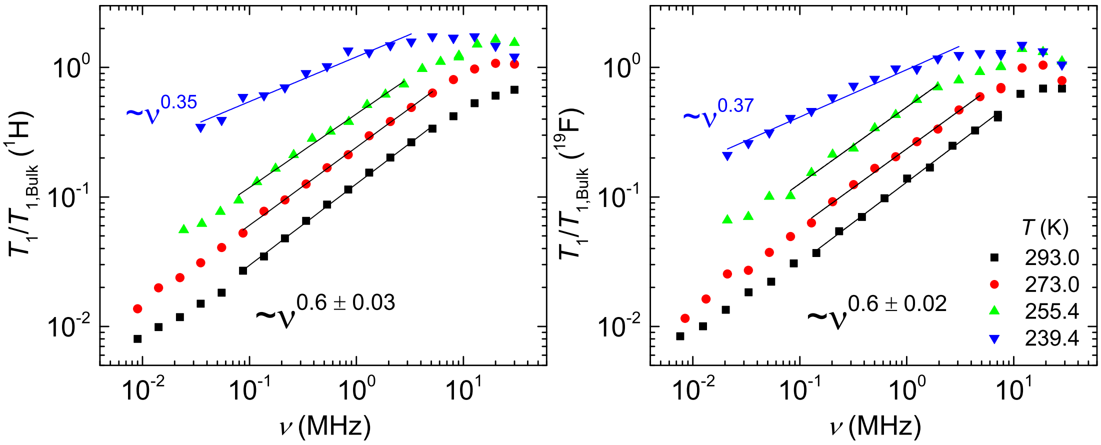

(a) (b)

Figure 6.6: Normalized T_1 relaxation dispersion curves of the bound Bmim Tf2N in Vycor confinement for a) ^{1}H and b)^{19}F following Eqs. (6.1)–(6.4)

frequencies below 20 MHz) the fast motional approximation should be valid for the free IL phase inside Vycor. This finding will be used in the following.

For a confined liquid that the exchange time of its molecules between bound and non-bound phases is shorter than the spin relaxation time $\tau_{\mathrm{ex}} < T_1$, the observed relaxation rate $R_1^{\mathrm{obs.}}$ will be the sum of relaxation rates of liquid in both phases with their population as weighting factors, p_{i}, see Eq. (2.35). The relative population of molecules in the free and bound states are temperature dependent while the relaxation rates are temperature and frequency dependent. Since the free (bulk) IL relaxation rates R_1^{f} are known (Fig. 4.4b), using Eq. (2.35) we can write

$$\left\{R_1^{\mathrm{obs.}}(T,\omega) = p_{\mathrm{f}}(T)\, R_1^{\mathrm{f}}(T,\omega) + [1-p_{\mathrm{f}}(T)]\, R_1^{\mathrm{b}}(T,\omega)\right\} \times \frac{1}{R_1^{\mathrm{f}}(T,\omega)}, \tag{6.1}$$

$$\frac{R_1^{\mathrm{obs.}}(T,\omega)}{R_1^{\mathrm{f}}(T,\omega)} = p_{\mathrm{f}}(T) + [1-p_{\mathrm{f}}(T)]\frac{R_1^{\mathrm{b}}(T,\omega)}{R_1^{\mathrm{f}}(T,\omega)}.$$

The ratio of relaxation rates of bound over free IL can be written considering the two motional limit conditions as following

$$\frac{R_1^{\mathrm{b}}(T,\omega)}{R_1^{\mathrm{f}}(T,\omega)} = \left[\left(\frac{\mu_0}{4\pi}\right)^2 \gamma^4 \hbar^2\right]^{-1} \times \begin{cases} R_1^{\mathrm{b}}(T,\omega)/5\tau_{\mathrm{c}}^{\mathrm{f}}(T) & , \quad \omega\tau_{\mathrm{c}}^{\mathrm{f}} << 1 \\ \frac{1}{2}\,\omega^2 \tau_{\mathrm{c}}^{\mathrm{f}}\, R_1^{\mathrm{b}}(T,\omega) & , \quad \omega\tau_{\mathrm{c}}^{\mathrm{f}} >> 1 \end{cases} \tag{6.2}$$

Physical interpretations of the molecular dynamics can be made if the motional narrowing condition $\omega\tau_{\mathrm{c}} << 1$ is assumed for the free phase of the ionic liquid. Therefore, the only frequency dependent term will be the bound relaxation rate. By substituting Eq. (6.2) in Eq. (6.1) for fast motional limit we get

$$\frac{R_1^{\mathrm{obs.}}(T,\omega)}{R_1^{\mathrm{f}}(T,\omega)} = p_{\mathrm{f}}(T) + \frac{1-p_{\mathrm{f}}(T)}{\left(\frac{\mu_0}{4\pi}\right)^2 \gamma^4 \hbar^2}\,\frac{R_1^{\mathrm{b}}(T,\omega)}{5\tau_{\mathrm{c}}^{\mathrm{f}}(T)}\,, \tag{6.3}$$

in which the only frequency dependent term is the relaxation rate of the bound molecules. The population of the free liquid and its correlation time are only temperature dependent. Equation (6.3) can be written in terms of relaxation times

$$\frac{T_1^{\mathrm{obs.}}(T,\omega)}{T_1^{\mathrm{f}}(T,\omega)} \propto T_1^{\mathrm{b}}(T,\omega). \tag{6.4}$$

Figure 6.6 shows the application of Eq. (6.4) by taking the relaxation data of the confined IL from Fig. 6.3 and bulk from Fig. 4.4b for temperatures higher than 240 K. The normalized values of the relaxation times increase by decreasing temperature. This is because of different frequency dependences of IL in Vycor confinement and in bulk. The Vycor confinement T_1 dispersions are almost similar for all temperatures while the T_1 dispersions for the bulk show stronger dispersions for lower temperatures. This affects the temperature dependent population factor p_{f} and the correlation time $\tau_{\mathrm{c}}^{\mathrm{f}}$ constants in Eq. (6.3) and has no effect on the frequency dependence. Therefore, the frequency dependent relaxation times of the bound IL T_1^{b} ($\propto T_1/T_1^{\mathrm{bulk}}$) can be fitted with a power law of $T_1^{\mathrm{b}} \sim \omega^{0.6}$ for both nuclei for temperatures higher that 255 K. This is in agreement with the above analysis. As Fig. 6.4 expected, at temperatures where the motional narrowing is valid the contributions of the free phase can be successfully cancelled out by the division in Eq. (6.2). Therefore, the power law slope of $\sim \omega^{0.6}$ corresponds to the pure bound IL dynamics on the pore surface. However, at temperatures lower than 248 K the motional narrowing condition does not apply for the whole frequency range of the field-cycling experiment. Therefore, the dispersion curve at 239.4 K in Fig. 6.6 cannot be explained since it includes some extra frequency dependency of the free liquid phase ($\omega\tau >> 1$ in Eq.(6.2))

By having the T_1 relaxation dispersion times which correspond to the Bmim Tf2N molecules in the bound phase (Fig. 6.6) it is time to consider the dynamics of molecules at this phase. As explained in Section 2.4 different dynamics with different timescales are possible in the bound layer. Considering the spectral density for the bound layer in Eq. (2.42), the contribution of the gamma process is frequency independent and can be subtracted. The remaining spectral density accounts for the α and β processes[52]. See Fig. 2.6.

$$J_{\alpha\beta}(\omega) = \int_0^{k_{\max}} S(k) \frac{2\tau_{\mathrm{k}}}{1+\omega^2\tau_{\mathrm{k}}^2} dk. \tag{6.5}$$

The orientational structure factor $S(k)$ can be expressed in an analytical form by a power law[51,52]

$$S(k) = \overbrace{b_\alpha \left(\frac{k_{\mathrm{co}}}{k}\right)^{\chi}}^{\alpha\text{-process}} + \overbrace{b_\beta \delta(k-k_{\mathrm{co}})}^{\beta\text{-process}}, \tag{6.6}$$

where b_α and b_β are the weighting factors and k_{co} is the cut-off wavenumber responsible for the low frequency plateau of the T_1 dispersion curve. The equation is valid for $k > k_{\mathrm{co}}$. This cut-off can be due to either the finite correlation length of the pore cluster or the exchange process with the free liquid phase. The δ-function represents a narrow distribution of wavenumbers and corresponds to the diffusion over the characteristic length of the particle or pore dimension.

The bound molecules on the surface are displaced through α and β processes and, at the same time, reoriented with respect to the local surface of the pores. This process is interpreted as the RMTD mechanism. The α-process accounts for the remote structural properties of the porous system, i.e. longest correlation times of the order of 10^{-4} s, Fig. 2.6. The β-process reflects the surface structure in the vicinity of the starting point of the translating molecule and indicates a correlation time of the order 10^{-9} s which causes the high-frequency plateau. The α-process is usually seen for porous material with different pore sizes while the β-process is seen for relatively larger pores. Therefore the Vycor glass, with pore size of $\sim 4\,\text{nm}$, does not show a clear high-frequency plateau[52]. The T_1 dispersions in Fig. 6.6 show structureless dispersion and dominated α-processes in a wider frequency range. A fractal analogue in the k-space has been suggested[51] for the interpretation of the $S(k) \propto k^{-\chi}$ in Eq. (6.6) where the T_1 dispersion of the α-process can be defined as

$$T_1 \propto \nu^{(1+\chi)/2}, \qquad \chi \geq 0. \tag{6.7}$$

Note that a power law weaker than $\nu^{0.5}$ leads to negative χ values which cannot be explained by this equation. The slope $\gamma \sim 0.6$ observed for the Vycor confined Bmim Tf2N for both ions at the temperature range 293 to 255 K is interesting. It suggests that these ions, despite their different ionic nature, are not distinguished by the RMTD process and behave similarly on the bound layer, what had already been seen for the bulk phase of this IL.

6.3 Discussion

The relaxation studies of the Vycor confined Bmim Tf2N ionic liquid is presented at different temperatures. The bulk water contribution to the relaxation is successfully cancelled by division of the observed relaxation time of confined IL by the bulk relaxation times at temperature-frequency ranges of the motional narrowing condition for bulk IL. The division has an advantage over the subtraction $(R_1^{\text{obs.}} - R_1^{\text{f}})$ because the population of the bound and free phases are not known. Therefore, by division the frequency dependent term is completely cancelled out. The estimation of the temperature-frequency range for the validity of $\omega\tau << 1$ condition for bulk IL predicted the right low-temperature limit. This procedure lead to the pure surface-bound ionic liquid contribution of the relaxation times. Such consideration was not crucial in the previous relaxation studies of confined liquids[51,52] since the bulk liquid, usually water, did not show a frequency dependent relaxation at the bulk phase.

A power law of $\sim \nu^{0.6}$ is fitted to the relaxation dispersion curves between 10 MHz and 0.1 MHz. This constant frequency dependence resembles the α-process of the RMTD process which corresponds to the displacement of molecules in the bound phase at longer length scales which determines the microstructural features of the pore-network. On the other hand, a shallow transition to the β-process at higher frequencies could be assigned to the short-distance displacements which probe the pore structure – a specific property of the porous material. However, a clear plateau at the high-frequency regime is not accessible by the field-cycling technique.

The surface of the Vycor glass, composed of mostly SiO_2, after treatment with H_2O_2 and water is expected to contain $-$SiOH groups. It is know from the studies of water in Vycor[50], where the surface hydroxyls were exchanged by propyl groups, that the polarity of the surface does not change the $T_1(\omega)$ dramatically. Therefore the observation of strong T_1 dispersions of Bmim Tf2N in Vycor cannot be related to the molecular interaction with the the surface. Moreover, if such interactions had dominant contributions on the T_1 relaxation times, then it would be expected that cations and anions would show different $T_1(\omega)$ behaviours. It can be assumed that the ions of the IL which approach to the vicinity of the pore-surface experience restrictions in their reorientational motions regardless of their charges. This is explained in terms of γ motions. However, these ions are not immobilized and tend to obtain a lateral diffusion along the surface. Depending on the length scale of the displacement, α and β processes are defined. Based on the results, the α-process is seen within the accessible frequency range of the apparatus which shows a frequency dependence of $\nu^{0.6}$.

The RMTD mechanism for the relaxation of confined molecules was originally developed for simple and isotropic liquids. This study took the challenge of application of this theory on a more complex ionic system. Studies with several ionic liquids in porous media with different pore sizes are required for a complete understanding of the molecular dynamics of confined ionic liquids.

Chapter 7

Crude Oil

The molecular composition of crude oils have a large impact on the production of the oil. NMR relaxation methods, being noninvasive, have the capability of down-hole and in situ measurements of crude oils. In this chapter, an effort is made to establish a method to characterize the composition of crude oils based on NMR relaxation times. There have been some efforts to model the crude oil composition by using linear alkanes[105,106] based on the fact that NMR relaxation times depend on the rotational diffusion time and hence, the size distribution and composition of molecules could be determined. However, the true composition of crude oils, especially the heavy oils, is much more complicated. Characterization of heavy compounds of oils, larger than around C36 are more difficult by conventional chromatographic methods[107] while the presence of such compounds affect critically the viscosity and phase behaviour of crude oils. Detection of amount of Asphaltene and resins and their aggregates has been the major challenge in the crude oil extraction worldwide. Many techniques have been developed[31] but each of them has its own drawbacks. Asphaltenes and resins present in heavy oils are essentially invisible to the conventional NMR methods due to their solid-like behaviour and short signal lifetime. Therefore, the detection of their existence in the oil is accessible only indirectly by means of the behaviour of the remaining maltene species. Considering the charge distribution of molecules, it can be assumed that aromatic maltenes will interact strongly with the polycyclic asphaltenes than alkanes[53].

In this chapter, the dynamic information of asphaltene molecules in crude oils are investigated indirectly by observing the dynamics of maltene molecules in the oil composition. In order to reduce the complexity of the crude oil system, it is reasonable to investigate similar maltene species with a different nucleus, ^{19}F in this case, that is not abundant in natural crude oil. These molecular species, or tracers, can then be easily distinguished by means of their spectral signatures.

In the first part of this chapter the relaxation studies of three types of crude oils with different compositions are compared at a stationary field strength of 7.05 T. The second part deals with solutions with controlled concentrations of asphaltene and an asphaltene-model molecule, violanthrone-78. The last part will deal with some of the samples of the first part and second to study the frequency dependent T_1 relaxation times.

7.1 Natural Crude Oils: A Comparative Study

Three crude oils are considered here: Asphaltene rich (A13), resin rich without asphaltene (A0), and without asphaltene and resins (W0). The SARA composition analysis of these oils are give in Table 3.1. Fluorinated solvents of aromatic and aliphatic nature are chosen to be used as tracers. These compounds are listed in Section 3.2. NMR spectra of some of the tracers are shown in Fig. 7.1. The fluorinated tracers are added in small concentrations and it is assumed that the tracers are homogeneously dissolved without altering the overall viscosity of the crude oils. It is also assumed that the behaviour of the fluorinated compounds are similar to their protonated counterparts which already exist in the crude oil composition and their molecular dynamics and the relaxation mechanisms are comparable, apart from a scaling factor[108] that accounts for different molecular masses and dipolar moments. And finally it is assumed that the dynamics of tracer molecules can be approximated by a single function and not a distribution of relaxation times. Before the addition of tracers to oils the bulk solutions of tracers as well as 2% dilution in toluene-d8 were studied and the T_1 and T_2 of ^{19}F nuclei were measured at a 7.05 T NMR spectrometer.

The addition of tracers allow the separation of intra- and intermolecular contributions to the relaxation. The results are shown in Table 7.1. The relaxation times in 2% diluted solutions are longer than bulk samples. Because the viscosities of samples are almost identical to the corresponding bulk viscosities, the difference in relaxation times are related to the absence of intermolecular relaxation mechanism in dilute solutions. The T_1/T_2 ratios of bulk and 2% dilution are similar for each tracer and reasonably close to 1, which is usually expected for a low-viscosity liquid ($\omega\tau << 1$). For simple fluids the proton or fluorine NMR relaxation is dominated by dipolar interactions modulated by local motions of the molecules. For small molecules with rapid molecular tumbling the dipolar interactions are averaged out and hence the relaxation times are long. In this case, T_1 and T_2 relaxation times are in the same range. The slight deviations seen in Table 7.1 can be related to some experimental conditions in measurements such as imperfections in the rf pulses which tend to generate shorter apparent T_2 values or presence of other relaxation processes besides dipolar interactions. It can also be attributed to the fact that the samples were not degassed and interaction with oxygen might bring about a further potential relaxation mechanism. The oxygen effect is mostly dominant at long relaxation times. In the relaxation study of the crude oil itself, the relaxation times are short and the paramagnetic relaxation mechanism due to the dissolved oxygen will be negligible[35].

The T_1/T_2 values in Table 7.1 are to be compared with the small amount of tracers dissolved in different oils. Table 7.2 summarizes the results of tracers in asphaltene-free oil A0. The ^{19}F longitudinal relaxation times of tracers in oil A0 are shorter relative to the corresponding bulk values. This is a combined effect of the prolongation of rotational and translational correlation times due to the enhanced viscosity of the oil, as well as a variation of the density of high-γ spins (^{1}H and ^{19}F) in the oil that are available for intermolecular relaxation. The most prominent

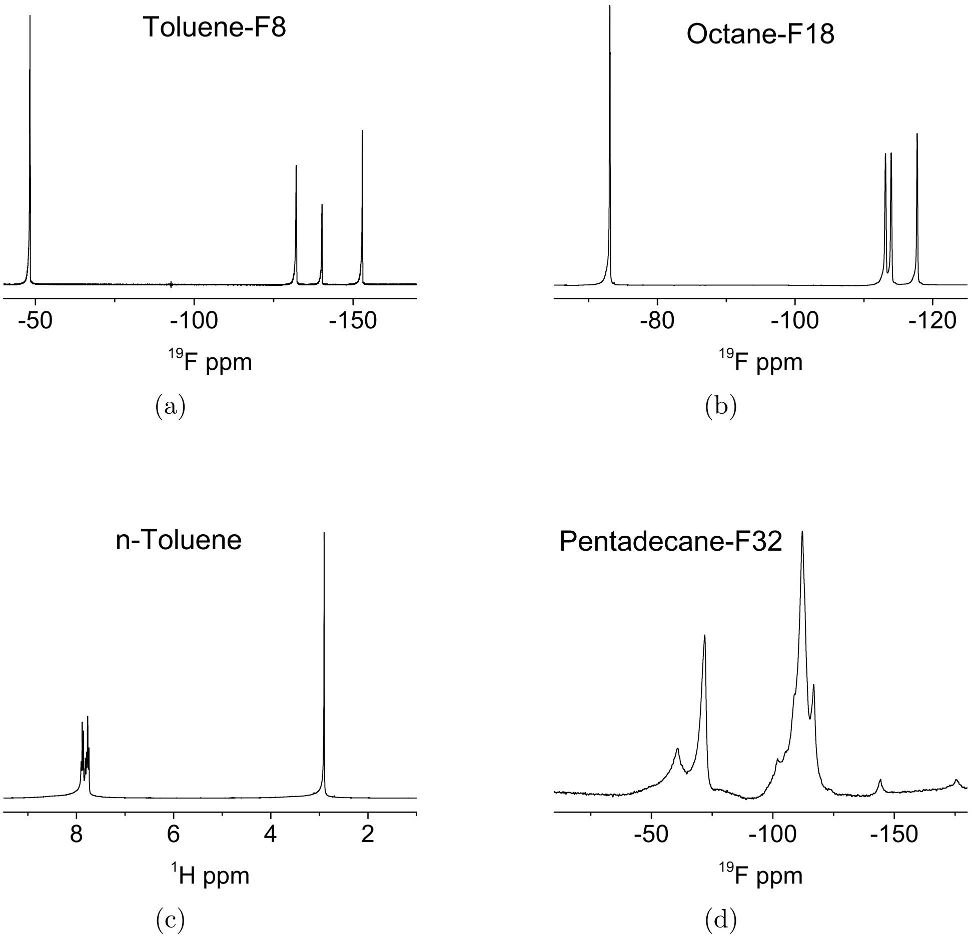

Figure 7.1: ^{19}F- and ^{1}H-NMR spectra of tracer compounds. The right/left limits of the ppm axis correspond to the high/low field. Consider that the relative chemical shift position of nuclei connected to aromatic rings and saturated groups are inverse for ^{19}F-spectra compared to the conventional ^{1}H-spectrum which is due to the electronegativity of F-atoms. That means, the nuclei on aromatic rings appear at right side of the ^{19}F-ppm scale. The three peaks (-125 – -150 ppm) for toluene-F8 correspond to ortho-, meta-, and para- positions. The ($-CF_2-$)'s of octane-F18 also appear at -110 – -120 ppm. The pentadecane-F32 is solid. The NMR measurement was done by dissolving it in toluene-d8, which is only partially dissoluble. The line broadening could be due to the overlap of the undissolved particles or because of the overlap of several $-CF_2$ groups of the dissolved pentadecane-F32.

Table 7.1: ^{19}F-relaxation times of bulk fluorinated tracers and 2% diluted solutions in toluene-d8 (shown in paranthesis when available) at room temperature and a magnetic field strength of 7.05 T †.

tracer	T_1(s)	T_2(s)	T_1/T_2
octane-F18	1.32 (2.50)	1.12 (2.11)	1.17 (1.18)
pentadecane-F32 ‡	1.19	0.97	1.23
benzene-F6	2.20 (3.50)	1.78 (2.77)	1.22 (1.26)
toluene-F8	1.76 (3.02)	1.47 (2.26)	1.19 (1.34)
benzene-F2	4.70	3.76	1.25
toluene-F3	1.91	1.63	1.18
toluene-F5	2.35	1.98	1.18
(-CF_3) octane-F18	1.51 (2.82)	1.23 (2.30)	1.23 (1.23)
(-CF_2-) octane-F18	1.23 (1.28)	1.07 (1.97)	1.15 (1.16)
(-CF_3) toluene-F8	1.61 (2.37)	1.36 (2.06)	1.18 (1.15)
(-C_5F_5) toluene-F8	1.85 (3.44)	1.49 (2.67)	1.18 (1.29)

† Fitting errors are below 1% and 2% for bulks and 2%-solutions, respectively.

‡ Pentadecane-F32 was highly diluted in d-toluene since it is solid in ambient conditions.

contrast, however, is observed not in the absolute values of relaxation times but in the T_1/T_2 ratios. These ratio values typically range from 2 to 6. For fluoroalkanes the results are similar to the corresponding bulk values ($T_1/T_2 \approx 2-3$). Therefore the viscosity effect on the molecular rotation times is negligible and $\omega\tau << 1$ remains generally true. On the other hand, aromatic molecules systematically show more pronounced T_1/T_2 dependences ($\approx 3-7$). This can, again, not be attributed to the viscosity because it can be safely assumed that the addition of 2% of any tracer does not significantly affect the overall viscosity of the bulk oil.

Tables 7.1 and 7.2 also include relaxation times of different ^{19}F carrying groups on toluene-F8 and octane-F18. The tail $-CF_3$ groups on both aromatic and saturated alkane show longer relaxation times than the ^{19}F nuclei on the aromatic ring or -CF_2- of the alkane chain.

For comparison, tracer molecules are investigated in the waxy oil W0 which mostly consists of saturated compounds, Table 7.3. Here, all four tracers, fluoroalkanes and aromatics, show only minimal T_1/T_2 deviations from their bulk values. The main difference between oil W0 and A0 is that W0 contains almost exclusively linear molecules where A0 includes higher content of aromatic maltenes plus some resins (8%). The distinction between asphaltenes and resins is merely a definition by means of solubility classes; resins also contain aromatic cores and can potentially contain radicals. The increased T_1/T_2 ratio of aromatics in A0 may thus tentatively be attributed to the interaction with resins.

In the asphaltene-rich oil A13, the range of T_1/T_2 ratio is much wider, Table 7.4. Aromatic tracers show a rapid increase of T_1/T_2 to about 100 while aliphatic tracers show only slightly more pronounced increase of T_1/T_2 ratios compared with oil A0. The change of relaxation times in oil A13 could be related, to some extent, to the

Table 7.2: ^{19}F-relaxation times of fluorinated tracers in oil A0 at room temperature and a magnetic field strength of 7.05 T. The last row shows ^{1}H-relaxation times of normal benzene. †.

tracer	T_1(s)	T_2(s)	T_1/T_2
octane-F18	1.00	0.40	2.52
pentadecane-F32	0.46	0.22	2.07
benzene-F6	0.95	0.23	4.13
toluene-F8	0.96	0.28	3.38
benzene-F2	2.39	0.35	6.81
toluene-F3	1.38	0.34	4.06
toluene-F5	0.97	0.16	6.26
(-CF_3) octane-F18	1.46	0.55	2.65
(-CF_2-) octane-F18	0.86	0.40	2.15
(-CF_3) toluene-F8	1.49	0.47	3.17
(-C_5F_5) toluene-F8	0.73	0.21	3.48
n-benzene	2.63	0.45	5.84

† Fitting errors are below 1% for T_1, below 3% for T_2, and below 2% for n-benzene.

Table 7.3: ^{19}F-relaxation times of fluorinated tracers in oil W0 at room temperature and a magnetic field strength of 7.05 T †.

tracer	T_1(s)	T_2(s)	T_1/T_2
octane-F18	1.10	0.79	1.39
pentadecane-F32	0.52	0.22	2.37
benzene-F6	1.80	1.15	1.56
toluene-F8	1.42	1.24	1.14
(-CF_3) octane-F18	1.77	1.00	1.77
(-CF_2-) octane-F18	1.15	0.77	1.49
(-CF_3) toluene-F8	1.55	1.17	1.32
(-C_5F_5) toluene-F8	1.32	0.90	1.47

† Fitting errors are below 1% for T_1 and below 3% for T_2.

Table 7.4: ^{19}F-relaxation times of fluorinated tracers in oil A13 at room temperature and a magnetic field strength of 7.05 T. The last row shows ^{1}H-relaxation times of normal benzene †.

tracer	T_1(s)	T_2(s)	T_1/T_2
octane-F18	0.724	0.146	4.96
pentadecane-F32	0.343	0.093	3.69
benzene-F6	0.655	4.40×10^{-3}	149
toluene-F8	0.673	9.15×10^{-3}	74
benzene-F2	1.380	12.7×10^{-3}	109
toluene-F3	1.175	21.2×10^{-3}	55
toluene-F5	0.651	3.50×10^{-3}	186
(-CF_3) octane-F18	1.07	0.21	5.09
(-CF_2-) octane-F18	0.64	0.14	4.57
(-CF_3) toluene-F8	1.02	18.3×10^{-3}	55.7
(-C_5F_5) toluene-F8	0.49	4.64×10^{-3}	105.6
n-benzene	0.79	17.3×10^{-3}	45.7

† Fitting errors are below 1% for T_1, below 3% for T_2. Fitting errors for n-benzene are about 6%.

viscose slow-down of the rotational correlation times (see viscosity data in Table 3.1). However, in a previous study increased T_1/T_2 values were observed systematically for asphaltene-rich oils even when compared to asphaltene-free oils of similar viscosity (oil #9 in[109] corresponds to A13 of this study). The large obtained T_1/T_2 values are mainly because of the rapid decrease of T_2 times, although T_1 times also decreased compared to other oils.

All results are well approximated by exponential relaxation behaviour so that fast averaging between relaxation environments can be assumed; this relates to averaging of tracers between the asphaltene environment and the bulk as well as averaging over possibly existing different geometries and radical concentrations of individual asphaltene aggregates. This causes slower tumbling motion of tracer molecules and at tumbling frequencies smaller than the Larmor frequency of the observed nuclei the two relaxation times T_1 and T_2 differ from each other.

7.2 Artificial Crude Oils: Asphaltene Solutions

So far, the relaxation enhancements observed for the oil with high asphaltene content could be related, but not limited, to either/both the nuclear-electron interaction with the unpaired electrons of asphaltenes or/and geometrical trapping of maltenes within the asphaltene aggregates. In order to simplify the complex crude oil composition, a set of artificial oil samples with controlled asphaltene concentrations were prepared. The asphaltene used here was extracted from crude oilsand the solid powder could be easily dissolved in predefined maltenes, i.e. alkanes and aromatics.

To investigate if and how the observed T_1/T_2 ratios in the previous section depend on the concentration of asphaltenes in oils, several sets of samples with controlled asphaltene concentrations were prepared. This procedure can be a potential probe for determination of asphaltene concentration in unknown oil samples. Two stock solutions of 15% (w/v) asphaltene dissolved in toluene-d8 were prepared. The highest concentration of asphaltene is chosen to be 15% since it is in the range of the highest amount of asphaltene usually found in natural crude oils. By stepwise dilutions of these solutions with toluene-d8 the lower concentrations of 8%, 4%, 2%, and 1% were obtained. 2% (v/v) toluene-F8 was added to all concentrations (1–15%) of the first set and 2% (v/v) n-toluene was added to the second set of samples as tracers. A third set of samples with asphaltene concentrations 15% to 1% were prepared dissolved only in n-toluene.

The spectra of toluene-d8 and n-toluene are presented in Fig. 7.1, where the aromatic and aliphatic signals are explained in the caption. The T_1 and T_2 relaxation times of toluene-d8, shown in Fig. 7.2, for both aliphatic chain ($-CF_3$) and aromatic ring ($-C_5F_5$) decrease by increasing asphaltene concentration. The decrease of T_1 of $-C_5F_5$ is stronger than $-CF_3$ while the variation of T_2 values at different asphaltene concentrations are similar to each other with slightly shorter T_2's for the aromatic ring. The effect is better seen observing the T_1/T_2 ratio variation. For both $-CF_3$ and $-C_5F_5$ increase of asphaltene concentration lead to almost linear increase of T_1/T_2 ratio. This effect is more significant for the aromatic ring-fluorine nuclei than the aliphatic chain, about three folds larger effect. The larger T_1/T_2 ratios for aromatic rings were also observed for the oil A13 in Table 7.4, see ($-CF_3$) toluene-F8 and ($-C_5F_5$) toluene-F8. However, the ratio obtained for oil A13 was, in general, much larger than the ratio of 15% asphaltene solution in toluene-d8 shown in Fig. 7.2. This can be related to the viscosity differences that affect both the asphaltene aggregates' tumbling time and the molecular motions of toluene, both of which may be related by joint maltene/asphaltene reorientations.

Notably, the ^{19}F-T_1 relaxation times, especially at low asphaltene concentrations (Fig. 7.2), for $-CF_3$ group is longer than the $-C_5F_5$. As it was shown in the previous section, the T_1 relaxation times for $-CF_3$ groups of toluene-F8 in all oil samples showed longer T_1 relaxation times than the aromatic $-C_5F_5$. The T_1/T_2 ratio differences between aliphatic and aromatic groups are consistent with previous findings.

The second set of samples with n-toluene as the tracer molecule in the asphaltene solutions of toluene-d8 suffered from overlap of proton signals of asphaltene molecules. In principle, the asphaltene molecules in natural oils are invisible to the liquid-state proton NMR. But due to the relatively rapid motion of asphaltenes in toluene-d8 solutions the broad ^{1}H-NMR signal of asphaltene remains prominent. Figure 7.3 shows the proton spectra of 2% toluene in toluene-d8 without and with addition of asphaltene. The spectrum of 0% asphaltene experiences some line broadening at the base which is due to proton impurities of toluene-d8 that appear with slightly different chemical shifts in the spectrum. By addition of asphaltene a clear broad peak centred at 1.5 ppm grows systematically which overlaps with the $-CH_3$ peak of toluene. At the aromatic region of the spectrum no such significant peak corresponding to the asphaltene is observed except for the shoulders at around 7.8 ppm.

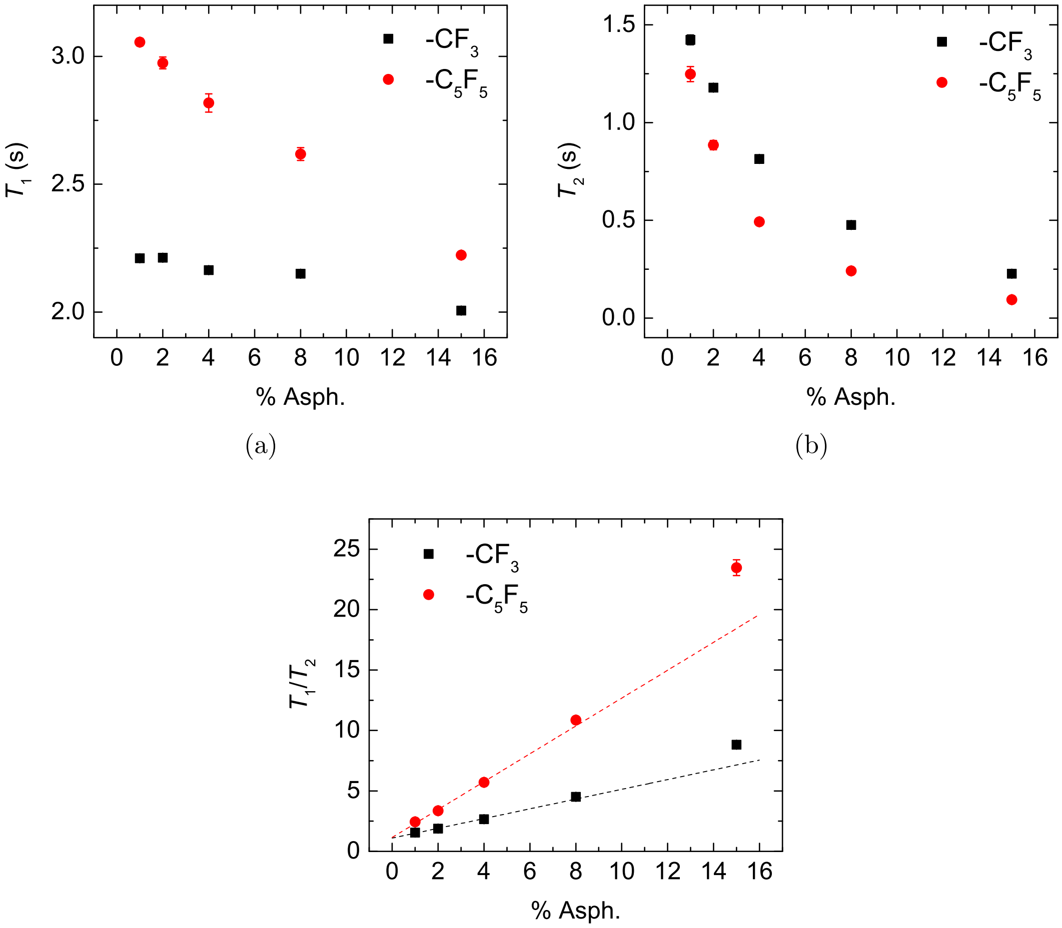

(a)

(b)

(c)

Figure 7.2: a) T_1, b) T_2, and c) T_1/T_2 ratio of ^{19}F nuclei of 2% toluene-F8 solution in toluene-d8 with varying amounts of asphaltene. Each graph shows the aliphatic ($-$CF$_3$) and aromatic ($-$C$_5$F$_5$) parts of toluene-F8.

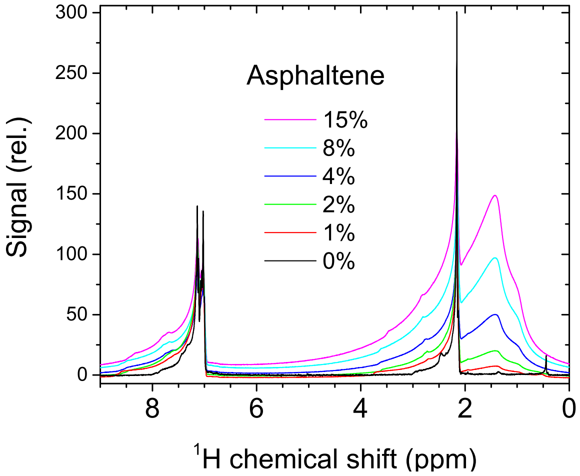

Figure 7.3: ^{1}H-spectra of different concentrations of asphaltene in a solution of 2% toluene in toluene-d8. The chemical shifts are adjusted for toluene peak of 2.2 ppm to be comparable.

Although the peaks of toluene and asphaltene overlap, the NMR relaxation signals of these mixtures could be separated to long and short relaxation components for both aliphatic and aromatic regions. Figure 7.4 shows the results for the aromatic region of the proton NMR signal. The aliphatic region of the spectrum leads to multi-exponential T_2 components (data not shown here) with frequently long T_2 times (for the peak at ~ 1.5 ppm) which correspond to more mobile side chains of asphaltenes.

The longe T_1 and T_2 relaxation components are attributed to the toluene molecules that are concentration dependent, Fig. 7.4a–b. The shorter components, which are concentration independent, are related to the aromatic parts of asphaltene molecules, $T_1 \approx 0.6$ s and $T_2 \approx 5$ ms. Such short T_2 times correspond to the tumbling of the asphaltene aggregates. Assuming a single correlation time and validity of BPP model, a characteristic time of 3.5×10^{-9} s is obtained. The T_1/T_2 ratios of the toluene tracer increase by one order of magnitude by increasing the asphaltene concentration from 1% to 15%, while for asphaltene no change of T_1/T_2 ratio ($\approx$ 100 to 150) is observed which is expected for a system of aggregates in an environment with constant viscosity. Using the Stokes-Einstein relation $\tau_{\mathrm{rot}} = 4\pi r^3 \eta / 3k_{\mathrm{B}}T$ and assuming a viscosity of 0.6 cP at room temperature, the above correlation time corresponds to a hydrodynamic radius of 1.8 nm which is in the range of reported aggregate sizes in oils[110,111]. Additionally as a proof, the relative contribution of the short T_1 relaxation time in the biexponential signal is plotted as a function of concentration of asphaltene in Fig. 7.4d.

The third set of samples were prepared with varying the asphaltene concentration in pure n-toluene. The T_1 and T_2 relaxation curves for the aliphatic and aromatic regions show monoexponential behaviour. The relaxation times and the ratios are shown in Fig. 7.5. The T_1 and T_2 values of the aromatic ring match the values in Fig.

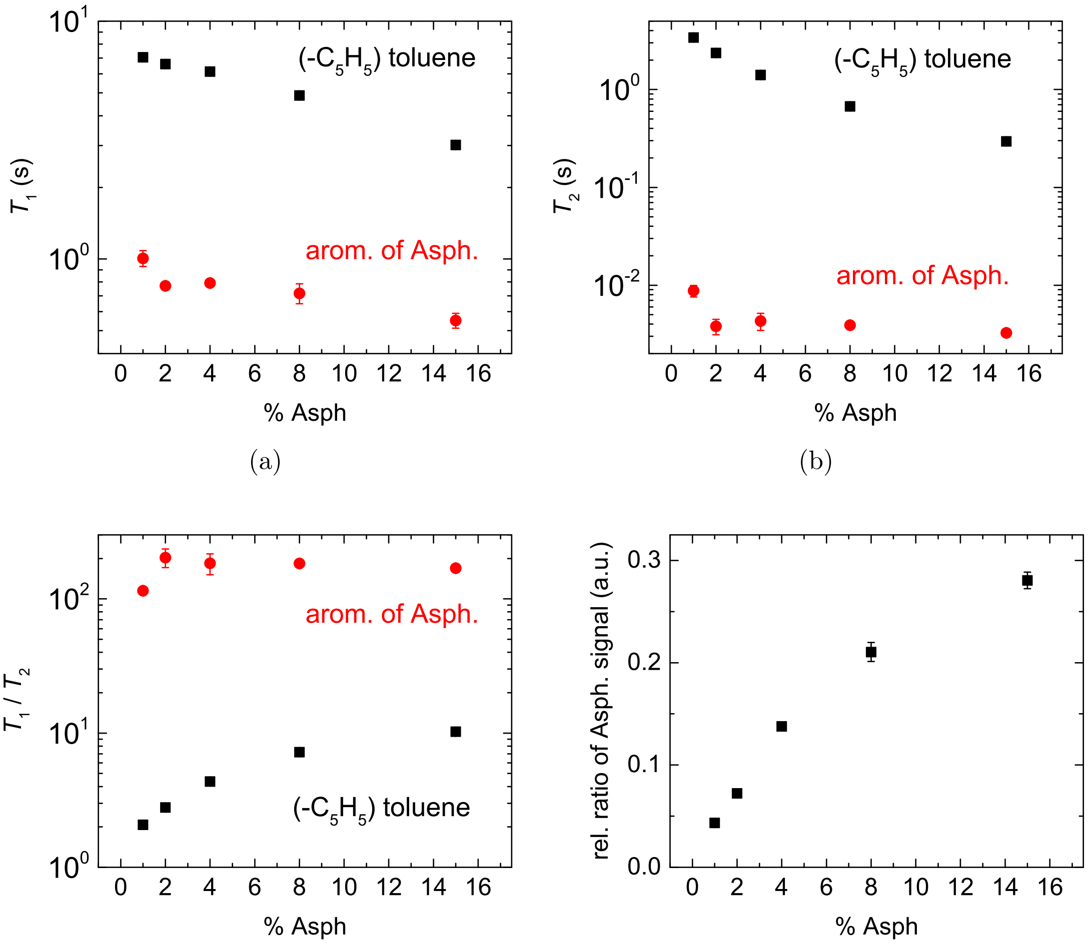

(a) (b)

(c) (d)

Figure 7.4: a) T_1, b) T_2, and c) T_1/T_2 ratio of aromatic ^{1}H nuclei of 2% n-toluene solution in toluene-d8 with varying amounts of asphaltene. Each graph shows aromatic protons stemming from toluene and asphaltene molecules. d) Relative ratios of asphaltene signals as a function of asphaltene concentration.

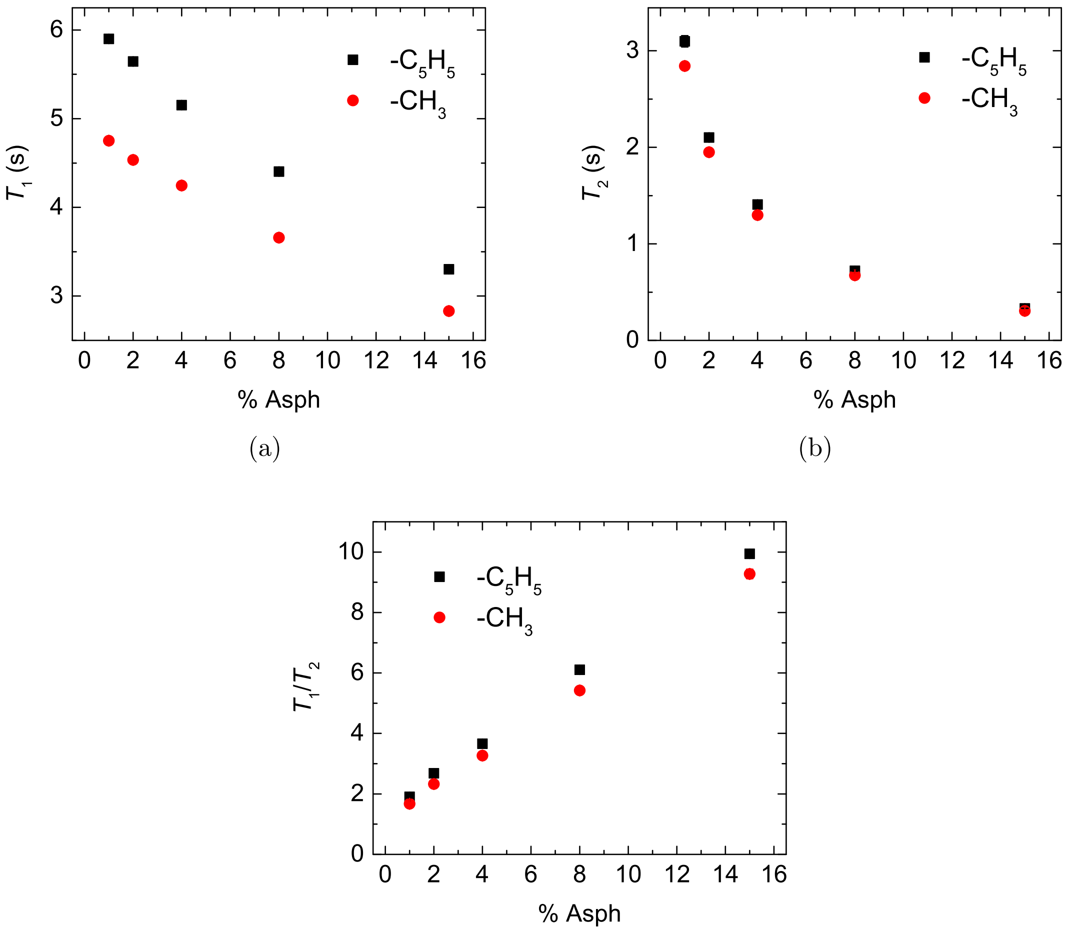

(a)

(b)

(c)

Figure 7.5: a) T_1, b) T_2, and c) T_1/T_2 ratio of aliphatic and aromatic ^{1}H nuclei of n-toluene with varying amounts of dissolved asphaltene.

Table 7.5: ^{19}F relaxation times of fluorinated tracers in 10% solutions of VO-78 and asphaltene in d-chloroform at room temperature and at a magnetization field strength of 7.05 T †.

	VO-78			Asphaltene		
tracer	T_1(s)	T_2(s)	T_1/T_2	T_1(s)	T_2(s)	T_1/T_2
benzene-F6	5.59	3.56	1.57	3.78	0.13	29.2
octane-F18	2.17	1.47	1.48	2.94	1.42	2.07

† Errors are below 1% for T_1 and below 3% for T_2.

7.4. The aliphatic chain of n-toluene, here as well, shows shorter T_1 relaxation times than the aromatic ring. On the other hand, the T_2 values of aromatic and aliphatic groups are similar. This leads to similar T_1/T_2 ratios for different concentrations of asphaltene while having slightly higher ratios for the aromatic part. The difference between ^{19}F- and ^{1}H-T_1/T_2 ratios were observed in the previous section upon doping toluene-F8 and normal toluene to the oil A13 where a weaker asphaltene concentration dependence was also observed for protons (compare Table 7.4 with Figs 7.2 and 7.5).

7.3 Model Asphaltene Molecule: VO-78

The Violanthrone-78 (VO-78) has been proposed to be a possible model molecule for asphaltene. The chemical structure of VO-78 is shown in Fig. 3.1. Apart from the promising applications of polyaromatic hydrocarbons in different scientific areas, the molecular stacking behaviour of VO-78 as a polyaromatic hydrocarbon in different organic solvents can reveal information on the nature of interaction of maltenes with polycyclic aggregates in general, and with asphaltene aggregates in particular. Therefore, the nuclear spin relaxation method is used here to study and compare the maltene interaction of a designed polycyclic molecule VO-78 with natural asphaltenes of not-completely-known structure. Despite the structural similarities between VO-78 and asphaltenes, VO-78 was found to contain much less radicals than natural asphaltenes, which is probably as a result of its synthesis process (140 time less or 1 radical in 5000 VO-78 molecules). Due to the low solubility of VO-78 in toluene, VO-78 was dissolved in chloroform-d to make a 10% (v/w) stock solution. Trace amounts of maltene tracers (benzene-F6 and octane-F18) were added separately to this solution. Similar asphaltene solutions in chloroform-d solvent were prepares for the sake of comparison. The results of ^{19}F relaxation time measurements of these samples are shown in Table 7.5. The VO-78 solution show almost equal T_1/T_2 values for both benzene-F6 and octane-F18 tracers while asphaltene solutions show larger T_1/T_2 ratio for benzene-F6, confirming the previous observations although the solvent (chloroform-d) type is different.

This behaviour can be correlated to the absence of radicals in VO-78. However, the radical content is not the only difference of VO-78 and asphaltene. The aggregation and stacking behaviour of VO-78, to the best of our knowledge, has not been

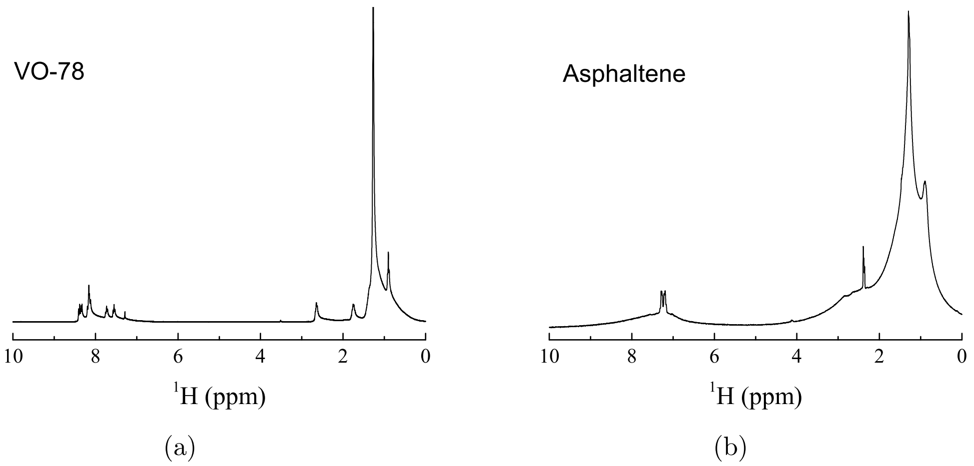

(a) (b)

Figure 7.6: ^{1}H-spectra of 10% solutions of a) VO-78 and b) asphaltene in $CDCl_3$.

Table 7.6: ^{1}H-relaxation times of 10% solutions of VO-78 and asphaltene in chloroform-d that lead to the largest T_1/T_2 ratios measured at room temperature and at a magnetization field strength of 7.05 T †. See Section 8 for detailed relaxation times.

	Aromatics			Aliphatics		
	T_1(s)	T_2(s)	T_1/T_2	T_1(s)	T_2(s)	T_1/T_2
VO-78	1.1	0.27	4.0	0.35	0.16	2.1
Asphaltene	0.75	2.6×10^{-3}	290	0.66	2×10^{-3}	330

† Errors are below 3%.

found and investigated experimentally. Molecular dynamic simulations have shown the possibility of VO-78 stacking at tens of nanosecond scale[112,113]. However, the ^{19}F relaxation results did not reveal such aggregation of VO-78 in chloroform-d.

The ^{1}H spectra and relaxation times of the 10% VO-78 and asphaltene in $CDCl_3$ were also measured and compared with each other (Fig. 7.6). The ^{1}H-spectrum of VO-78 gives NMR lines which are narrower than the asphaltene at the same situation. This could be partially related to the viscosity difference in two samples. But since the viscosities are not significantly different, the broad peaks of asphaltene can stem from wide distribution of polyaromatic hydrocarbons present in the natural asphaltene extracted from crude oils. The relaxation times for each of proton groups in Fig. 7.6 are analysed. The T_1 and T_2 relaxation time distributions of the NMR lines in VO-78 and asphaltene are given in Table 7.6. The detailed relaxation times of each proton group can be found in the Section 8.

The T_1/T_2 ratios of VO-78 are consistently found to be less than 5 while the same for asphaltenes are found to be approximately 300. The corresponding correlation times for the above ratio values of the aromatic parts (backbone) are 5.4×10^{-9} s

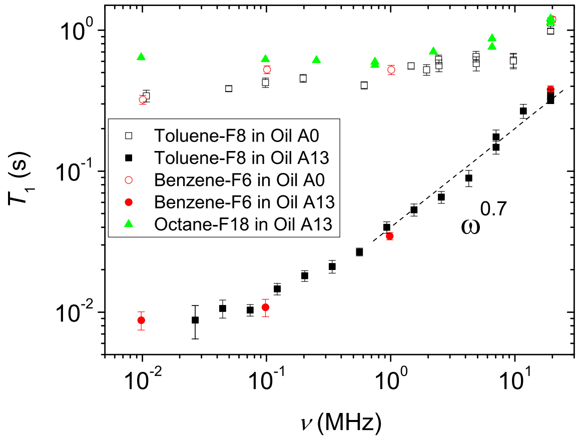

Figure 7.7: ^{19}F relaxation times of fluorinated tracers in oils A0 and A13 at room temperature as a functin of ^{19}F Larmor frequency. The dashed line shows the power law fit of toluene-F8 in A13 data between 1 and 20 MHz.

and 6.5×10^{-8} s, respectively. Addition of 5% fluorinated tracers does not change any of the ^{1}H relaxation times by more than 10% (see Section 8). Although the motional narrowing limit is not fulfilled for any of these solutions ($\omega\tau > 1$) and therefore no quantitative result can be derived, one can, nevertheless, argue that if VO-78 aggregates exist, they must be substantially much smaller than those of asphaltenes.

7.4 Field-Cycling NMR Relaxometry

The T_1/T_2 ratio constitutes an approximate approach to the dynamic properties of a molecule and is rather straightforward to acquire even under borehole conditions. On the other hand, it gives the reorientational information of molecules at a certain frequency. Obtaining the full reorientation spectrum requires the discussion of the frequency dependence of the longitudinal relaxation time, $T_1(\omega)$, over a range of resonance frequencies as wide as possible, a method that is currently available only on the lab scale. In this section, results of the field-cycling experiments on the samples discussed in previous section are presented.

The field dependent longitudinal relaxation experiments were carried out on two oils, A0 and A13, without and with asphaltene content, respectively. Three perfluorinated tracers were dissolved in oils at about 5% (w/v): two aromatics (benzene-F6 and toluene-F8) and one aliphatic (octane-F18). Despite of the low signal-to-noise ratio of the fluorine signal, good quality T_1 dispersion profiles were obtained. All the magnetization signal decays were found to be monoexponential within experimental errors. The $T_1(\omega)$ are shown in Fig. 7.7

Strong frequency dependences are visible for benzene-F6 and toluene-F8 in oil A13 whereas much weaker frequency dependences are seen for all substances in oil

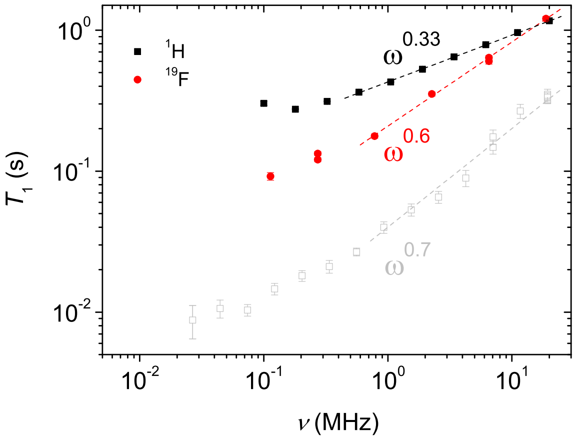

Figure 7.8: ^{1}H- and ^{19}F-$T_1(\omega)$ of 15% asphaltene solution in n-toluene (black) and in toluene-d8 with 5% toluene-F8 (red). The data in grey are ^{19}F-$T_1(\omega)$ of toluene-F8 in oil A13 (from Fig. 7.7) presented for the sake of comparison. Linear fits of $T_1(\omega)$ between 1 and 20 MHz are given for each data set.

A10 and also for the octane-F18 in oil A13. The strong dispersion in the frequency dependence of T_1 values are consistent with the large T_1/T_2 ratios seen previously for aromatic tracers in asphaltene-rich oils since the theory requires that $\lim_{\omega\to 0} T_1(\omega) \propto T_2$.

The dispersion indicates that the reorientational processes in the time range of 10^{-8} s to 10^{-6} s (and possibly longer) are relevant for the relaxation mechanism. Between frequencies of about 1 and 20 MHz the dispersion can tentatively be approximated by a power-law relation $T_1 \propto \omega^{0.7}$. It is known that in the presence of radicals, which are almost always associated with the presence of asphaltenes, the relaxation dispersion becomes more pronounced as the term $1/T_1^{\mathrm{elec}}$ in Eq. (2.43) begins to dominate.

Similar experiments are performed with artificial crude oil samples of 15% asphaltene dissolved in n-toluene and d8-toluene. 5% toluene-F8 was added to the latter solution as tracer. The outcome of the frequency dependent ^{1}H- and ^{19}F-T_1 relaxation experiments are shown in Fig. 7.8. The frequency dependence is much stronger for the case of ^{19}F-$T_1(\omega)$ and a power law fit at the frequency range of 1 MHz to 20 MHz gives $T_(\omega) \propto \omega^{0.6}$, which is consistent with the power law behaviour seen for the toluene-F8 in oil A13 (Fig.7.7). However, the frequency dependence is shallower by almost half for the n-toluene solution of asphaltene. Smaller T_1/T_2 ratios were also observed in the previous section for ^{1}H relaxation times in comparison with ^{19}F (n-benzene vs. benzene-F8 in Table 7.4).

The asphaltene aggregates can be considered as locally flat (2D) geometries. A model developed by Korb[114,115] where adsorbate molecules are allowed to interact with the radical containing asphaltenes at a characteristic residence time τ_{s}, and probe the surface structure by diffusing along the surface for a time τ_{m} where $\tau_{\mathrm{s}} >> \tau_{\mathrm{m}}$. The observed spin-lattice relaxation rate in this case can be written as

$$
\begin{aligned}
1/T_1(\omega_\mathrm{I}) = 1/T_1^\mathrm{bulk}(\omega_\mathrm{I}) + \mathrm{const}\ \tau_\mathrm{m} \Bigg[& 3\ln\left(\frac{1+\omega_\mathrm{I}^2\tau_\mathrm{m}^2}{(\tau_\mathrm{m}^2/\tau_\mathrm{s}^2)+\omega_\mathrm{I}^2\tau_\mathrm{m}^2}\right) \\
& +7\ln\left(\frac{1+\omega_\mathrm{S}^2\tau_\mathrm{s}^2}{(\tau_\mathrm{m}^2/\tau_\mathrm{s}^2)+\omega_\mathrm{I}^2\tau_\mathrm{s}^2}\right)\Bigg],
\end{aligned}
\tag{7.1}
$$

where ω_I and ω_S are the nuclear and electron Larmor frequencies, respectively. T_1^bulk is the relaxation time in the bulk without interaction with the asphaltene surface and generally is frequency dependent and summarizes the contributions of T_1^intra and T_1^inter. Considering the very broad T_1 distribution known from crude oils and particularly from oils with asphaltene[109], a model fit requires consideration of an average T_1[114]. However, this requires to assume that all molecules behave the same way in the presence of asphaltene and the characteristic times τ_s and τ_m are mere functions of the molecular size. However, a previously reported relaxation dispersion by Korb et al.[114] for a crude oil with 9% asphaltene showed a weaker frequency dependence ($T_1 \sim \omega^{0.2}$) compared to our finding in Fig. 7.7 for the oil with 13% asphaltene.

It needs to be remarked that only a small number of asphaltene molecules contain radicals and, thus, contribute to the proposed mechanism. An upper limit of 5% radical was estimated from EPR measurements. Typical concentration of unpaired electrons are as following: 1 to 3 per 100 asphaltene molecules[116] and 1 per 90 bitumen molecules[117]. This explains why, despite the line-broadening effect of radicals, spectral features have been observed clearly in asphaltene solutions, and even line-specific relaxation times of the asphaltenes themselves could be assigned (for instance see Fig. 1).

Similar strong dispersions were also observed for some types of oils by Zielinski et al.[110,118]. The model proposed for asphaltene by these authors assumes loose porous structure for asphaltene aggregates. In fact the existence of fractal structures of dimension $d_\mathrm{f} < 3$ have already been shown for the asphaltene aggregates by neutron and X-ray scattering experiments[32,33,119]. The solvent molecules can diffuse through porosities and are in fast exchange between the bulk and the porous asphaltene aggregates. The solvent molecules which come into contact with asphaltene aggregates get entangled with them but not completely immobilized. At this step, the translational dynamics of solvent molecule become highly correlated and the diffusion of maltene molecules can be modelled as diffusion in restricted dimensions characterized by a timescale τ_M. On the other hand, the whole asphaltene aggregate, together with the confined maltene molecules, experience rotational Brownian motion with a time scale τ_A which is related to the size of aggregate through the Einstein-Stokes equation. Additionally, the nuclear spins of the entangled maltene tracers (^{1}H or ^{19}F) undergo dipolar nuclear spin relaxations enhanced by the electronic spins on paramagnetic centres or free radicals embedded in the asphaltene molecules. This dipolar interaction is modulated by the composite motion of the restricted maltene diffusion and the overall tumbling of the aggregate. If these two motions are assumed as uncorrelated, at long times the correlation function becomes[118]

$$G(t) = (t/\tau_{\mathrm{M}})^{-d/2}\ exp(-t/\tau_{\mathrm{A}}), \tag{7.2}$$

where d is the dimensionality of the diffusive motion of the maltene molecules inside the asphaltene aggregates. For $d = 1$ the corresponding spectral density is computed

$$J(\omega) \propto \mathcal{R}\Big[\tau_{\mathrm{M}}\tau_{\mathrm{A}}/(1 + i\omega\tau_{\mathrm{A}})\Big]^{1/2}, \tag{7.3}$$

where τ_{M} scales with the maltene molecular size. For small molecules with shorter τ_{M} the relaxation induced by asphaltenes is less than for large maltenes with longer τ_{M}. However, this model does not predict frequency dependent relaxation rates for $d > 1$. Additionally, the aromaticity and different shapes of the maltene molecules are not considered in this model[53].

The above theory assumes the molecular tumbling of the aggregate itself. However, strong frequency dependent relaxations ($\sim \omega^{0.3-0.6}$) were also found in a different system of radical containing mesoporous catalyst of coke-covered surface filled with organic fluids[120]. In this system, no tumbling of large molecules or aggregates can occur, thus the apparent power-law behaviour cannot be justified by the same dynamical process.

So far, one relaxation process for the ^{1}H and ^{19}F nuclei of maltene molecules is considered to be the dipolar interaction between nuclei and electrons of possible radicals of asphaltene aggregates. Since the dipolar coupling between a quadrupolar nuclei and electron is too weak, if one can substitute all the protons of the maltene with deuterium, then it will be expected that no effective dipolar relaxation should occur and therefore no ^{2}H-T_1 relaxation dispersion will be expected. Deuterium substitution is achieved by dissolving asphaltene (15% w/v) in toluene-d8. The ^{2}H-T_1 dispersion of this sample is shown in Fig. 7.9. The ^{2}H-T_1 magnetization recovery curves showed a clear bi-exponential behaviour at all measured frequencies. The relative contribution of the short T_1 component being approximately double of the long component implying the number ratio of the aromatic to the aliphatic deuterium nuclei in a toluene-d8 molecule. The longer T_1 components show slightly more dispersion (40 folds) than the short components (10 folds) from 2 MHz to 10^{-3} MHz of ^{2}H-Larmor frequency.

7.5 Discussion

The addition of fluorinated tracer molecules to the natural crude oils made it possible to track the molecular interactions of maltenes with asphaltenes and/or resins. The lack of fluorine nuclei in natural oil compositions facilitates the use of T_1/T_2 ratio of ^{19}F nuclei as a measure of interaction in these natural oils. T_1/T_2 ratios of order of 100 was found for the unsaturated tracer molecules, e.g. benzene-F6 and toluene-F8, in the asphaltene-rich oil A13. However, much shorter ratios of about 5 were obtained for saturated tracers, e.g. octane-F18 and pentadecane-F32, in the same oil.

The measurement of such distinct ratios in crude oils had not been reported previously[53]. This difference is explained by an increased interaction time of the

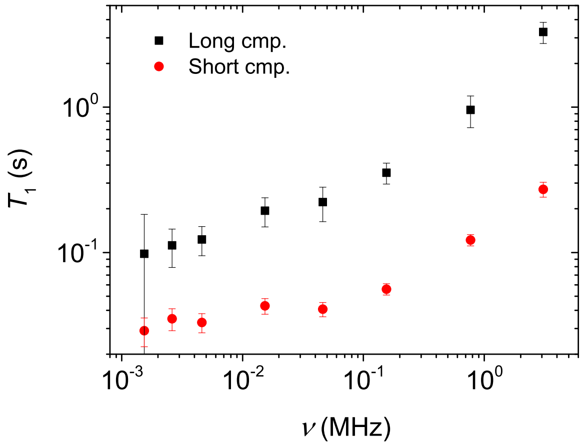

Figure 7.9: ^{2}H-T_1 relaxation dispersion profile for the 15% asphaltene dissolved in toluene-d8. The relative contribution of short component is nearly double of the long component.

aromatics with the polycyclic asphaltene surfaces as a consequence of $\pi - \pi$ stacking mechanism that has been reported before to govern the clustering phenomena of resins and asphaltenes. According to the current models, nuclear spin relaxation is dominated by the presence of radicals being associated with the asphaltene aggregates, and the longer interaction time of the maltenes in the vicinity of these aggregates makes dipolar relaxation of the ^{19}F by the electron spin more efficient. This concept would apply irrespective of the location of the predominant maltene molecules, either on the outer surface or within the voids of the asphaltene aggregates.

The asphaltene-free oil A0 which contains 8% resins showed less pronounced effects comparing with the same aromatic tracer molecules in oil A13. Nevertheless, the ratios of aromatic tracers were double of the aliphatic tracers in oil A0. Based on the relaxation model, the relatively small ratio differences imply that the oil A0 and resins therein should not contain considerable amount of unpaired electrons. This is confirmed by some EPR measurements that resins of oil A0 contain 100 times less radicals than asphaltenes of oil A13. The asphaltene- and resin-free oil W0 showed almost equal ratios for aromatic and aliphatic tracers.

The stronger interaction of aromatic tracers with the polycyclic asphaltene surfaces results high relaxivity and hence, larger T_1/T_2 ratio[53,121]. In such a condition, it is expected that the mobility of the whole tracer molecule is affected, not only the aromatic part. However, the experiments with partially fluorinated toluene tracers toluene-F3 and toluene-F5, with fluorinated methyl group and fluorinated aromatic ring respectively, show longer relaxation times for the $-$CF$_3$ group of toluene-F3. The ring fluorines in toluene-F5, on the other hand, give even higher T_1/T_2 ratio than ring fluorines of toluene-F8. This difference is explainable considering the electronic clouds of the aromatic rings and the resultant $\pi - \pi$ stacking probabilities. Indeed, the fast-rotating methyl group in any molecule is known to maintain its higher mobility down to very low temperatures, and the autocorrelation function of its spin vectors is a sum of contributions of the fast rotation about the C_3 symmetry axis and the overall tumbling of the molecule. It is, thus, less susceptible to an extension of the molecular reorientation correlation time, a fact that has also been proven by measuring the relaxation times of the ring and methyl group moieties of toluene-F8 separately, as shown in Tables 7.2 to 7.4. The same is true for alkanes where, for instance, the fluorine atoms in the terminal ($-CF_3$) groups in octane-F18 possess T_1 and T_2 values slightly longer than those of the ($-CF_2-$) fluorine nuclei. First preliminary results on the ^{1}H-relaxation times of benzene added at a concentration of ca. 5% to oils A0 and A13 are of similar magnitude and confirm the validity of the observations found for ^{19}F nuclei, so that a nucleus-specific effect must be considered unlikely. The slightly larger difference observed in T_1/T_2 of benzene compared with the fluorinated benzene is due to the overlapping of the benzene chemical shift with the aromatic protons of asphaltene.

The T_1/T_2 ratios in the artificial oils made by dissolving controlled amounts of extracted asphaltenes in toluene-d8 showed similarly large ratios for toluene-F8 tracers. The ratios increased linearly with the concentration of asphaltene being stronger for the aromatic part of toluene-F8. The protonated toluene was also used as a tracer which showed as well an asphaltene concentration dependent increase of the ratio while obtaining the ratio values about half of the same for the fluorine tracers. The different interaction nature of the fluorinated and protonated tracers which leads to differences in the T_1/T_2 ratios was also seen in crude oils. The signal of the asphaltene itself led to much larger ratios of around 100.

The violanthrone-78, although known as a model molecule for asphaltenes, did not show similar ratios at equal concentrations compared with the asphaltene solutions[122]. This was related to the weaker aggregating behaviour as well as the absence of unpaired electrons in the structure of VO-78.

Frequency-dependent NMR relaxation time measurements confirm the large difference between aromatic and aliphatic tracers in the asphaltene-containing oil as well as asphaltene solutions. The frequency dependence of the T_1 relaxation times at Larmor frequencies $\omega/2\pi$ between 10^6 and 10^8 Hz showed a strong frequency dependence of approximately $T_1 \sim \omega^{0.6-0.7}$ for the fluorinated tracers while a shallower dependence of about $T_1 \sim \omega^{0.3}$ for the protonated tracer. The explanation of such dependences requires the development of an improved model of molecular reorientation taking into consideration not only the size but also the aromaticity of the tracer molecules, and hence the maltene. The proposed method not only provides a possibility to differentiate between the molecular mechanisms leading to NMR relaxations from a fundamental point of view but also represents a means of selectively addressing the interaction of maltene with asphaltenes and, thus, to identify the presence of asphaltene molecules by addition of small amounts of tracers. These experiments proved the efficiency of benzene-F6 and toluene-F8 in detecting even small concentrations of asphaltene due to the large sensitivity of NMR relaxation times. This approach will allow, on a laboratory scale, to avoid the time-consuming SARA analysis. A downhole application, requiring the injection of tracer substances, can be of potential interest if carried out at specific instants and with small amounts that do not contaminate the reservoir; fluorine-containing drilling mud may be considered as a possible tracer source.

Chapter 8

Summary and Outlook

Since the emerge of the focused research on the room temperature ionic liquids numerous researchers have tackled different aspects of these materials, yet the answers to the most fundamental questions remain blurred. The main reason lies in the facts that ionic liquids can be multi-diverse in behaviour. The large functioning temperature range of them adds to their physicochemical complexity. In the frame of this thesis two main research topics were followed. The first topic had a focus on two groups of ionic liquids in bulk phase and in nano-porous confinement with a special consideration on the supercooled temperature regime. The second topic tackled a long-standing challenge in the crude oil industry to identify and determine the macromolecules and asphaltenes in the heavy oils. The main analytical methods employed were the nuclear magnetic resonance (NMR) relaxometry and diffusometry. The highlights of these studies are summarized below.

The supercooled temperature regimes of each ionic liquid in the bulk state was determined by the differential scanning calorimetry (DSC) method. The thermal behaviour and transitions were discussed from the view points of kinetics and thermodynamics. The NMR frequency dependent relaxation and diffusion measurement were carried out for the supercooled temperature ranges. Nuclear spin relaxation models considering different possibilities of molecular interactions were assumed and detailed fitting procedures were performed on the experimental data. The correlation times for translational and rotational motions of individual ions were resulted from the fittings. The non-Arrhenius behaviours of translational motions were found to be a general property for all of the ionic liquids under study while the rotational dynamics followed Arrhenius temperature dependences. A general trend was seen that cations and anions of same ionic liquid had similar temperature dependent translational behaviour. For the case of Bmim Tf2N ionic liquid the ratio of minimum distance of approaches ζ of (anion-to-anion distance)/(cation-to-cation distance) was calculated from the relaxation times. At above the melting point of Bmim Tf2N this ratio found to be around unity while at temperatures approaching the glass transition it decreases systematically. This observation was interpreted as the transition of Bmim Tf2N from an ideal to a non-ideal behaviour: the motion of anions with respect to the neighbour anions are more cooperative that the motion of cations with respect to the neighbour cations. This observation is confirmed by the Vogel-Fulcher-Tammann fits to the temperature dependence of translational correlation time where a slightly larger κ value – degree of fragility or cooperative dynamics – was found for the anion-anion translational dynamics that for cation-cation. However, the degree of cooperativity between anions-and-cations remained the largest that could correspond to their ionic nature.

The translational correlation times for the case of Bmim Br and Hmim Br were found for the cations and by assuming the radii values for cations the relative minimum distances of approach for cation-cation were calculated from the relaxation times. Although a similar temperature dependences for the translational correlation times were found for Bmim and Hmim, the distances between cation-cation for Bmim Br was found to be larger at temperatures approaching the glass transition while Hmim Br showed almost constant cation-cation distance at the same temperatures. This difference in temperature dependence of cation-cation distance could be justified from the DSC studies. Hmim Br showed no other transition than the glass transition which indicated that the ions in Hmim Br did not tend to obtain a cooperative dynamics even at deeply supercooled temperatures. A unique feature observed in all studied ionic liquids that could supercool until the glass transition was the crossover temperature T_{c}. At this temperature, the temperature dependence of the dynamic properties of ions deviated from their high temperature trend. This had been known for molecular glass forming liquids for a long time and some similar observations for ionic liquids were reported. But no systematic study on ionic liquids had shown this unique crossover transition for the ionic liquids investigated in this study.

The frequency dependent relaxation times of Bmim Tf2N ionic liquid confined in Vycor glass with pore size of 4 nm were obtained. The analysis of these relaxation times were not possible without having the knowledge of the bulk IL behaviour since there is a bulk-like free phase in the porous media. Assuming that IL molecules could be exchanged between the surface-bound phase and the free phase within the time of the longitudinal relaxation time, the contribution of free phase could be removed from the original relaxation data. This assumption could only be valid in the fast motion limit of the bulk IL. Therefore, detailed analysis of the motional limits of bulk Bmim Tf2N was carried out. Different dynamical mechanisms were considered for the molecule in the surface-bound layer in the frame of the RMTD (Reorientations Mediated by Translational Displacements) mechanism. It could be concluded that the power law frequency dependence of $\sim \nu^{0.6}$ for the relaxation dispersions observed in the proton Larmor frequency range of between 10 MHz and 0.1 MHz were resulted from the long-range surface displacements – known as the α process in the RMTD mechanism. Similar power laws were observed for cation and anion of the ionic liquid. This was found to be consistent with previous studies where the strong dispersions were more dependent on the polarity of the liquid and mostly independent on the polarity of the silica surface groups. However, the observation of similar behaviour of cations and anions of ionic liquid at the surface of nano-porosities had not been reported previously.

A comparative study on three types of crude oils with completely different compositions were carried out. The ^{19}F-nuclei on the fluorinated aromatic and aliphatic organic solvents were used to trace the interaction strength with the macromolecules and asphaltenes inside the oils. The relaxation time ratios of T_1/T_2 were used as measures of interaction strength or the prolonged dynamics of tracer molecule in the presence of interactions. It was found that crude oils with a higher content of asphaltene lead to larger relaxation ratio values while the absence of asphaltenes resulted much smaller ratios. Solutions with defined concentrations of asphaltene were prepared in deuterated organic solvents and the concentration dependence of the T_1/T_2 were investigated. Concentration dependent behaviours were found for the aromatic tracers. Similar measurements on a molecule proposed to be a model for asphaltene was carried out and no significant T_1/T_2 ratio was observed at its highest concentration. The frequency dependent relaxation studies revealed strong dispersions with a power law frequency dependences of $\nu^{0.7}$ for the aromatic tracers inside the asphaltene rich oils. The proposed method provided a selective method in identifying and determining the presence and concentration of asphaltene in crude oils. The large sensitivity of this method for small concentrations of the fluorinated solvents in oils could be an easier alternative to the costly SARA analysis and enlightens the possibility of a feature application in the oil fields.

Appendices

Appendix A

Relaxation Times of VO-78 and Asphaltene

The relaxation times represented in Table 7.6 correspond to the proton groups which give the largest T_1/T_2 ratios. Here the detailed relaxation times corresponding to each proton groups (chemical shifts) of 10% VO-78 and asphaltene in $CDCl_3$ solutions are shown in Fig. 7.6.

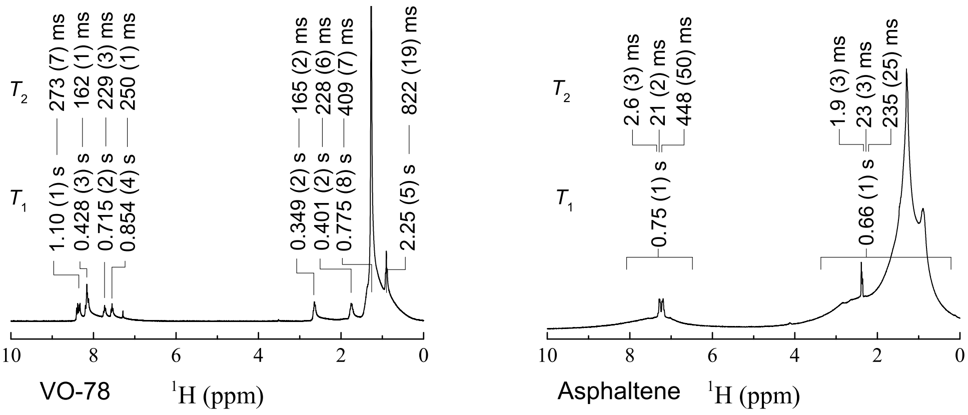

(a) (b)

Figure 1: ^{1}H-spectra of 10% solutions of a) VO-78 and b) asphaltene, in $CDCl_3$

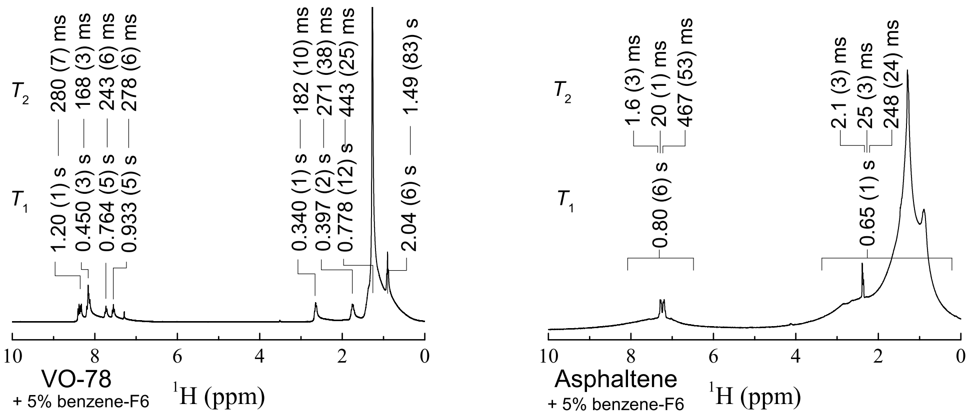

(a) (b)

Figure 2: ^{1}H-spectra of 10% solutions of a) VO-78 and b) asphaltene, in $CDCl_3$ with addition of 5% benzene-F6 tracer.

The addition of 5% tracer solvent (benzene-F6) has a minor effect on the ^{1}H-relaxation times which are shown in Fig. 2

Appendix B

Fitting Procedures by Python

A set of Python 2.7 scripts were written for the data analysis. Below the step by step procedure for the fitting of a T_1 relaxation dispersion profile of Bmim Tf2N will be explained. For the cases of Bmim Br and Hmim Br the procedure will remain the same with a difference that the heteronuclear interaction terms will not be included in the total relaxation function.

The fitting procedure for Bmim Tf2N starts with reading the T_1 relaxation values for different Larmor frequencies for ^{1}H and ^{19}F at every temperature. The frequency values must match for both nuclei (considering the gyromagnetic ratios). The input file takes the Larmor frequencies, relaxation times, and the absolute error values in three columns. The function takes the 'filename' and returns the Larmor frequencies (`omega`), relaxation rates (`R1`) and the error values of the relaxation rates (`R1Err`).

```
import numpy as np
import os.path

def readFile(filename):
    """ Reads data file as 2 or three columns
     separated by space and . as decimal mark """
# ------ Experimental data --------- begin ----
    if os.path.isfile(filename) == False:
        ValueError("Filename not entered or does not exist!")
    else:
        pass

    inFile = open(filename, 'r')
    omega = np.array([])
    T1 = np.array([])
    Err = np.array([])
    for aline in inFile:
        values = aline.split( )
        if len(values) == 2:
            omega = np.append(omega,1e6*np.float(values[0])*2*np.pi )
            T1 = np.append(T1,np.float(values[1]) )

        if len(values) == 3:
            omega = np.append(omega,1e6*np.float(values[0])*2*np.pi )
```

```
            T1 = np.append(T1,np.float(values[1]) )
            T1Err = np.append(Err,np.float(values[2]) )
            R1 = 1.0/T1
            R1Err = T1Err/T1**2

    data = ([omega,R1,R1Err])
    return (data)

    # ------ Experimental data --------- end ----
```

The append approach above allows reading of data files with varying data points. The frequencies in the field-cycling output file are usually expressed in MHz units. The frequencies above are calculated in angular frequency units (rad/s).

The intramolecular and intermolecular spectral density functions can be defined according to Eqs. (2.11) and (2.15), respectively.

```
def J_intra(tau, omega):
    J = tau  / ( 1 + (omega*tau)**2 ) + 4*tau  / ( 1 + (2*omega*tau)**2 )
    return(J)
"""The intermolecular spectral density can be of homonuclear (II)
   or heteronuclear type (IS or SI)"""
def J_inter(tau, omega,lo,hi,iteration_num):
    from scipy.special import jv # jv(v, z), Bessel function
    integ_w = np.zeros(len(omega))

    int_range = np.linspace(lo,hi,iteration_num)
    def func(tau,omega,u):
        f = jv(1.5,u)**2 * u/(u**4 + (omega * tau)**2)
        return(f)

    for io in range(len(omega)):
        f = func(tau, omega[io], int_range)
        value = simps(f, x=int_range)
        integ_w[io] = value
    J = tau * integ_w
    return (J)

def J_II(tau, omega_I,lo,hi,iteration_num):
    J = 1.0*J_inter(tau, omega_I,lo,hi,iteration_num) \
        + 4.0*J_inter(tau,omega_I,lo,hi,iteration_num)
    return (J)

def J_IS(tau, omega_I, omega_S,lo,hi,iteration_num):
    J = J_inter(tau, omega_I - omega_S,lo,hi,iteration_num) \
        + 3.0*J_inter(tau, omega_I,lo,hi,iteration_num)\
        + 6.0*J_inter(tau, omega_I + omega_S,lo,hi,iteration_num)

def J_SI(tau, omega_S, omega_I,lo,hi,iteration_num):
    J = J_inter(tau, omega_I - omega_S,lo,hi,iteration_num) \
        + 3.0*J_inter(tau, omega_S,lo,hi,iteration_num)\
        + 6.0*J_inter(tau, omega_I + omega_S,lo,hi,iteration_num)
```

```
    return (J)
```

The intramolecular spectral density function takes the tau and omega values as input while the intermolecular function J-inter takes also the low and high integration limits and the integral iterations as constants. The Simpson's numerical integration rule is used here.

The relaxation rate functions for intra molecular and intermolecular – homo and hetero – are defined according to Eqs. (2.27) and (2.31) as below. Consider that the dipolar coupling constants are not yet implemented in the relaxation rate functions and will be considered in the total relaxation rate function in the next step.

```
def R1intra(self, w, tau):
    R1 = sd.J_intra(tau, w)
    return R1

def R1II(self, wI, tau):
    R1_II = sd.J_II(tau, wI,self.lo,self.hi,self.niter)
    return( R1_II  )

def R1IS(self, wI, tau):
    R1_IS = sd.J_IS(tau, wI, wI*self.ratioFonH ,\
                        self.lo, self.hi, self.niter)
    return( R1_IS )

def R1SS(self, wI, tau):
    R1_SS = sd.J_II(tau, wI*self.ratioFonH,\
                        self.lo, self.hi, self.niter)
    return( R1_SS  )

def R1SI(self, wI, tau):
    R1_SI = sd.J_IS(tau, wI*self.ratioFonH, wI ,\
                        self.lo, self.hi, self.niter)
    return( R1_SI )
```

By taking all the fitting parameters the total relaxation rate function is given by

```
def R1total_min(self, params,w,data,sig):
    KTII = params['KTII'].value
    tauTII = params['tauTII'].value

    KTIS = params['KTIS'].value
    tauTIS = params['tauTIS'].value

    KRI = params['KRI'].value
    tauRI = params['tauRI'].value

    KTSS = params['KTSS'].value
    tauTSS = params['tauTSS'].value

    KTSI = params['KTSI'].value
    tauTSI = params['tauTSI'].value
```

```
    KRS = params['KRS'].value
    tauRS = params['tauRS'].value

    R1I = KTII * self.R1II(w,tauTII) + \
                KTIS * self.R1IS(w, tauTIS) + \
                KRI * self.R1intra(w, tauRI)
    residsI = R1I - data[0,:]

    R1S = KTSS * self.R1SS(w, tauTSS) + \
                KTSI * self.R1SI(w, tauTSI)  + \
                KRS * self.R1intra(w, tauRS)
    residsS = R1S - data[1,:]
    weighted = 0.0*data[:]
    weighted[0,:] = residsI**2/data[0,:]**2
    weighted[1,:] = residsS**2/data[0,:]**2
    return weighted.flatten()
```

By defining all the relaxation functions as above the fitting procedure can be started. The minimization function of the `scipy.optimization` package using the Levenberg-Marquardt method is used for this purpose.

```
def OnClick_Minimize( self, event ):
# parameter definitions
    params = Parameters()
    params.add('KTII', value = self.KTII)
    params.add('tauTII', value = self.tauTII)

    params.add('KTIS', value = self.KTIS)
    params.add('tauTIS', value = self.tauTIS)

    params.add('KRI', value = self.KRI)
    params.add('tauRI', value = self.tauRI)

    params.add('KTSS', value = self.KTSS)
    params.add('tauTSS', value = self.tauTSS)

    params.add('KTSI', value = self.KTSI)
    params.add('tauTSI', value = self.tauTSI)

    params.add('KRS', value = self.KRS)
    params.add('tauRS', value = self.tauRS)

    params.add('eps1', value = self.eps1, vary=True)
    params.add('eps2', value = self.eps2, vary=True)
    params.add('rr', value = self.rr, vary=False)

    params['tauTIS'].expr ='tauTSI'
    params['KTIS'].expr = 'KTII / (8.475 * eps1**3)'
    params['KTSI'].expr = 'KTSS / (1.062 * eps2**3)'

    data, sig = [], []
```

```
    data.append(self.R1I)
    data.append(self.R1S)
    sig.append(self.ErrI)
    sig.append(self.ErrS)
    self.data = np.array(data)
    self.sig = np.array(sig)
    start = timeit.default_timer()
# minimization step ----------------
    minimize(self.R1total_min, params, \
                args=(self.omegaI, self.data, self.sig),\
                        method=self.sel_method[c] )
    end = timeit.default_timer()
# save fit parameters --------
    self.saveParams = str(params)
```

The function begins with defining the fitting parameters. Some initial values are given for each parameter which reads from the initiator `init` function of the original class (not given here). The boundary conditions above are defined according to Eqs. (4.9) and (4.10).

The above fitting procedure can be implemented in a way to load the experimental relaxation data for all temperatures and do the fit independently for all temperatures. Finally the fitting parameters can be plotted in Arrhenius plots. The rest of the programming is the matter of taste. For the purpose of this thesis a graphical unit interface (GUI) was designed using the `wxPython package` to simplify and increase the usability of the script. A snapshot of the GUI associated with the codes above is shown in Fig. 3.

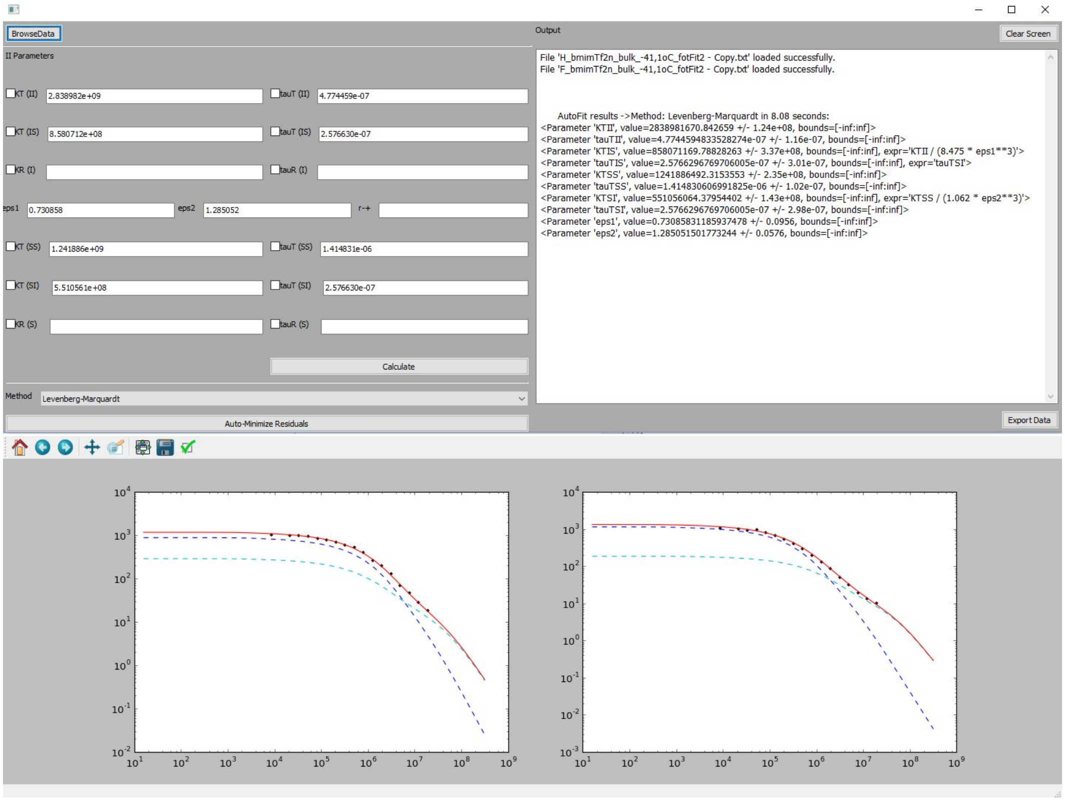

☐ KT (II) 2.838982e+09
☐ tauT (II) 4.774459e-07
☐ KT (IS) 8.580712e+08
☐ tauT (IS) 2.576630e-07
☐ KR (I)
☐ tauR (I)
eps1 0.730858
eps2 1.285052
r-+
☐ KT (SS) 1.241886e+09
☐ tauT (SS) 1.414831e-06
☐ KT (SI) 5.510561e+08
☐ tauT (SI) 2.576630e-07
☐ KR (S)
☐ tauR (S)
Method Levenberg-Marquardt

```
File 'H_bmimTf2n_bulk_-41,1oC_fotFit2 - Copy.txt' loaded successfully.
File 'F_bmimTf2n_bulk_-41,1oC_fotFit2 - Copy.txt' loaded successfully.



    AutoFit results ->Method: Levenberg-Marquardt in 8.08 seconds:
<Parameter 'KTII', value=2838981670.842659 +/- 1.24e+08, bounds=[-inf:inf]>
<Parameter 'tauTII', value=4.7744594833528274e-07 +/- 1.16e-07, bounds=[-inf:inf]>
<Parameter 'KTIS', value=858071169.78828263 +/- 3.37e+08, bounds=[-inf:inf], expr='KTII / (8.475 * eps1**3)'>
<Parameter 'tauTIS', value=2.5766296769706005e-07 +/- 3.01e-07, bounds=[-inf:inf], expr='tauTSI'>
<Parameter 'KTSS', value=1241886492.3153553 +/- 2.35e+08, bounds=[-inf:inf]>
<Parameter 'tauTSS', value=1.414830606991825e-06 +/- 1.02e-07, bounds=[-inf:inf]>
<Parameter 'KTSI', value=551056064.37954402 +/- 1.43e+08, bounds=[-inf:inf], expr='KTSS / (1.062 * eps2**3)'>
<Parameter 'tauTSI', value=2.5766296769706005e-07 +/- 2.98e-07, bounds=[-inf:inf]>
<Parameter 'eps1', value=0.73085831185937478 +/- 0.0956, bounds=[-inf:inf]>
<Parameter 'eps2', value=1.285051501773244 +/- 0.0576, bounds=[-inf:inf]>
```

Figure 3: The graphical interface of the fitting program developed in Python 2.7.

Bibliography

[1] H. Ohno, *Electrochem. Asp. Ion. Liq.*, edited by H. Ohno (John Wiley & Sons, Inc., Hoboken, NJ, USA, 2011).

[2] C. A. Angell, J. Non. Cryst. Solids **131-133**, 13 (1991).

[3] C. A. Angell, in *Molten Salts From Fundam. to Appl.*, edited by M. Gaune-Escard (Springer Netherlands, Dordrecht, 2002).

[4] C. A. Angell, Y. Ansari, and Z. Zhao, Faraday Discuss. **154**, 9 (2012).

[5] N. V. Plechkova and K. R. Seddon, Chem. Soc. Rev. **37**, 123 (2008).

[6] J.-P. Belieres and C. A. Angell, J. Phys. Chem. B **111**, 4926 (2007).

[7] M. N. Kobrak and H. Li, Phys. Chem. Chem. Phys. **12**, 1922 (2010).

[8] C. J. Margulis, H. a. Stern, and B. J. Berne, J. Phys. Chem. B **106**, 12017 (2002).

[9] J. K. Shah, J. F. Brennecke, and E. J. Maginn, Green Chem. **4**, 112 (2002).

[10] Z. Hu and C. J. Margulis, Proc. Natl. Acad. Sci. **103**, 831 (2006).

[11] M. N. Kobrak and V. Znamenskiy, Chem. Phys. Lett. **395**, 127 (2004).

[12] M. N. Kobrak, J. Chem. Phys. **125**, 064502 (2006).

[13] M. N. Kobrak, J. Chem. Phys. **127**, 184507 (2007).

[14] W. Xu, E. I. Cooper, and C. A. Angell, J. Phys. Chem. B **107**, 6170 (2003).

[15] F. Kremer and A. Schönhals, *Broadband Dielectric Spectroscopy* (Springer Berlin Heidelberg, Berlin, Heidelberg, 2003).

[16] U. Tracht, M. Wilhelm, A. Heuer, H. Feng, K. Schmidt-Rohr, and H. Spiess, Phys. Rev. Lett. **81**, 2727 (1998).

[17] A. Wulf, R. Ludwig, P. Sasisanker, and H. Weingärtner, Chem. Phys. Lett. **439**, 323 (2007).

[18] D. Kruk, R. Meier, A. Rachocki, A. Korpala, R. K. Singh, and E. a. Rössler, J. Chem. Phys. **140**, 244509 (2014).

[19] M. Namboodiri, M. M. Kazemi, T. Zeb Khan, A. Materny, and J. Kiefer, J. Am. Chem. Soc. **136**, 6136 (2014).

[20] V. V. Matveev, D. a. Markelov, E. a. Brui, V. I. Chizhik, P. Ingman, and E. Lähderanta, Phys. Chem. Chem. Phys. **16**, 10480 (2014).

[21] S. Gabl, C. Schröder, D. Braun, H. Weingärtner, and O. Steinhauser, J. Chem. Phys. **140**, 184503 (2014).

[22] H. Weingärtner, Angew. Chem. Int. Ed. Engl. **47**, 654 (2008).

[23] P. J. Griffin, A. L. Agapov, A. Kisliuk, X.-G. Sun, S. Dai, V. N. Novikov, and A. P. Sokolov, J. Chem. Phys. **135**, 114509 (2011).

[24] N. Ito, W. Huang, and R. Richert, J. Phys. Chem. B **110**, 4371 (2006).

[25] C. Daguenet, P. J. Dyson, I. Krossing, A. Oleinikova, J. Slattery, C. Wakai, and H. Weingärtner, J. Phys. Chem. B **110**, 12682 (2006).

[26] C. A. Angell, Science **267**, 1924 (1995).

[27] H. Manafi, G. Mansoori, and S. Ghotbi, J. Pet. Sci. Eng. **22**, 67 (1999).

[28] G. Mansoori, "Proceedings" of "OilGasScientificResearchProjects" Institute, SOCAR **2010**, 12 (2010).

[29] G. Mansoori, OPEC Rev. **12**, 103 (1988).

[30] G. Mansoori, D. Vazquez, and M. Shariaty-Niassar, J. Pet. Sci. Eng. **58**, 375 (2007).

[31] O. C. Mullins, E. Sheu, A. Hammami, and A. Marshall, *Asphaltenes, Heavy Oils, and Petroleomics* (Springer New York, New York, NY, 2007).

[32] T. F. Headen, E. S. Boek, J. Stellbrink, and U. M. Scheven, Langmuir **25**, 422 (2009).

[33] J. Eyssautier, P. Levitz, D. Espinat, J. Jestin, J. Gummel, I. Grillo, and L. Barre, J. Phys. Chem. B **115**, 6827 (2011).

[34] K. J. Leontaritis and G. Mansoori, J. Pet. Sci. Eng. **2**, 1 (1989).

[35] A. R. Mutina and M. D. Hürlimann, Appl. Magn. Reson. **29**, 503 (2005).

[36] M. P. Hoepfner, C. Vilas Bôas Fávero, N. Haji-Akbari, and H. S. Fogler, Langmuir **29**, 8799 (2013).

[37] K. J. Leontaritis and G. Mansoori, Soc. Pet. Eng. , 149 (1987).

[38] J. M. Swanson, J. Phys. Chem. **46**, 141 (1942).

[39] T. F. YEN, Energy Sources **1**, 447 (1974).

[40] G. E. Uhlenbeck and S. Goudsmit, Nature **117**, 264 (1926).

[41] M. H. Levitt, *Spin Dynamics: Basics of Nuclear Magnetic Resonance* (Wiley, 2008).

[42] J. Keeler, *Understanding NMR Spectroscopy*, 2nd ed. (Wiley, 2010).

[43] A. Abragam, *The Principles of Nuclear Magnetism* (Oxford University Press, 1961).

[44] A. Gupta, T. Stait-Gardner, M. J. Moghaddam, and W. S. Price, Concepts Magn. Reson. Part A **44**, 74 (2015).

[45] M. Goldman, *Quantum Description of High-Resolution NMR in Liquids* (Oxford University Press, 1991).

[46] R. Kimmich, *NMR-Tomography, Diffusometry, Relaxometry* (Springer Berlin Heidelberg, 1997).

[47] N. Bloembergen, E. Purcell, and R. Pound, Phys. Rev. **73**, 679 (1948).

[48] R. Kimmich, T. Gneiting, K. Kotitschke, and G. Schnur, Biophys. J. **58**, 1183 (1990).

[49] K. Packer, Phil. Trans. Roy. Soc. Lond. **B 278**, 59 (1977).

[50] S. Stapf, *NMR-Untersuchungen zur Relaxations- und Diffusionsdynamik von Flüssigkeiten und Polymeren in Materialien mit eingeschränkter Geometrie*, Ph.D. thesis (1996).

[51] S. Stapf, R. Kimmich, and J. Niess, J. Appl. Phys. **75**, 529 (1994).

[52] R. Kimmich, S. Stapf, P. Callaghan, and A. Coy, Magn. Reson. Imaging **12**, 339 (1994).

[53] S. Stapf, A. Ordikhani-Seyedlar, N. Ryan, C. Mattea, R. Kausik, D. E. Freed, Y.-q. Song, and M. D. Hürlimann, Energy & Fuels **28**, 2395 (2014).

[54] W. S. Price, *NMR Studies of Translational Motion Principles and Applications* (Cambridge University Press, 2009).

[55] O. Russina, A. Triolo, L. Gontrani, and R. Caminiti, J. Phys. Chem. Lett. **3**, 27 (2012).

[56] A. V. Blokhin, Y. U. Paulechka, A. A. Strechan, and G. J. Kabo, J. Phys. Chem. B **112**, 4357 (2008).

[57] Y. Shimizu, Y. Ohte, Y. Yamamura, and K. Saito, Chem. Phys. Lett. **470**, 295 (2009).

[58] A. Noda, K. Hayamizu, and M. Watanabe, J. Phys. Chem. B **105**, 4603 (2001).

[59] H. Tokuda, K. Hayamizu, K. Ishii, M. A. B. H. Susan, and M. Watanabe, J. Phys. Chem. B **109**, 6103 (2005).

[60] M. C. C. Ribeiro, J. Chem. Phys. **134**, 244507 (2011).

[61] T. Endo and S. Sen, J. Phys. Chem. B (2014), 10.1021/jp510672z.

[62] S. R. Prabhu and G. B. Dutt, J. Phys. Chem. B **118**, 13244 (2014).

[63] S. Tsuzuki, W. Shinoda, H. Saito, M. Mikami, H. Tokuda, and M. Watanabe, J. Phys. Chem. B **113**, 10641 (2009).

[64] K. Hayamizu, S. Tsuzuki, S. Seki, and Y. Umebayashi, J. Chem. Phys. **135**, 084505 (2011).

[65] T. Feiweier, O. Isfort, B. Geil, F. Fujara, and H. Weingaertner, J. Chem. Phys. **105**, 5737 (1996).

[66] R. Kimmich and E. Anoardo, Prog. Nucl. Magn. Reson. Spectrosc. **44**, 257 (2004).

[67] E. M. Woo and T. Y. Ko, Colloid Polym. Sci. **274**, 309 (1996).

[68] C. A. Angell, K. L. Ngai, G. B. McKenna, P. F. McMillan, and S. W. Martin, J. Appl. Phys. **88**, 3113 (2000).

[69] J. H. Antony, D. Mertens, A. Dölle, P. Wasserscheid, and W. R. Carper, ChemPhysChem **4**, 588 (2003).

[70] W. R. Carper, P. G. Wahlbeck, J. H. Antony, D. Mertens, A. Dölle, and P. Wasserscheid, Anal. Bioanal. Chem. **378**, 1548 (2004).

[71] W. R. Carper, P. G. Wahlbeck, and A. Dölle, J. Phys. Chem. A **108**, 6096 (2004).

[72] J. H. Antony, A. Dölle, D. Mertens, P. Wasserscheid, W. R. Carper, and P. G. Wahlbeck, J. Phys. Chem. A **109**, 6676 (2005).

[73] N. E. Heimer, J. S. Wilkes, P. G. Wahlbeck, and W. R. Carper, J. Phys. Chem. A **110**, 868 (2006).

[74] J. H. Antony, D. Mertens, T. Breitenstein, A. Dölle, P. Wasserscheid, and W. R. Carper, Pure Appl. Chem. **76**, 255 (2004).

[75] M. Imanari, H. Tsuchiya, H. Seki, K. Nishikawa, and M. Tashiro, Magn. Reson. Chem. **47**, 67 (2009).

[76] H. Tokuda, K. Hayamizu, K. Ishii, M. A. B. H. Susan, and M. Watanabe, J. Phys. Chem. B **108**, 16593 (2004).

[77] A. Ribeiro and S. Vieira, in *Ion. Liq. Theory, Prop. New Approaches*, edited by A. Kokorin (InTech, 2011).

[78] K. Hayamizu and S. Handy, in *Ion. Liq. - Classes Prop.*, edited by S. Handy (InTech, 2011) pp. 210–235.

[79] O. Söderman, W. S. Price, M. Schönhoff, and D. Topgaard, J. Mol. Liq. **156**, 38 (2010).

[80] G. S. Fulcher, J. Am. Ceram. Soc. **8**, 339 (1925).

[81] M. D. Ediger, C. A. Angell, and S. R. Nagel, J. Phys. Chem. **100**, 13200 (1996).

[82] P. J. Griffin, J. R. Sangoro, Y. Wang, A. P. Holt, V. N. Novikov, A. P. Sokolov, Z. Wojnarowska, M. Paluch, and F. Kremer, Soft Matter **9**, 10373 (2013).

[83] P. J. Griffin, A. L. Agapov, and A. P. Sokolov, Phys. Rev. E **86**, 021508 (2012).

[84] J. O. Bockris and A. K. N. Reddy, *Modern Electrochemistry 1*, 2nd ed. (Springer US, 1998).

[85] K. Hayamizu, S. Tsuzuki, and S. Seki, J. Phys. Chem. A **112**, 12027 (2008).

[86] K. Hayamizu, S. Tsuzuki, S. Seki, Y. Ohno, H. Miyashiro, and Y. Kobayashi, J. Phys. Chem. B **112**, 1189 (2008).

[87] K. Hayamizu, S. Tsuzuki, S. Seki, K. Fujii, M. Suenaga, and Y. Umebayashi, J. Chem. Phys. **133**, 194505 (2010).

[88] K. Ueno, H. Tokuda, and M. Watanabe, Phys. Chem. Chem. Phys. **12**, 1649 (2010).

[89] H. Tokuda, S. Tsuzuki, M. A. B. H. Susan, K. Hayamizu, and M. Watanabe, J. Phys. Chem. B **110**, 19593 (2006).

[90] M. Goldstein, J. Chem. Phys. **51**, 3728 (1969).

[91] X. Xia and P. G. Wolynes, Phys. Rev. Lett. **86**, 5526 (2001).

[92] M. D. Ediger, Annu. Rev. Phys. Chem. **51**, 99 (2000).

[93] H. C. Torrey, Phys. Rev. **92**, 962 (1953).

[94] C. a. Sholl, J. Phys. C Solid State Phys. **14**, 447 (1981).

[95] J. Harmon and B. H. Muller, Phys. Rev. **182**, 400 (1969).

[96] J. Harmon, Chem. Phys. Lett. **7** (1970), 10.1016/0009-2614(70)80289-5.

[97] J. J. Moura Ramos and H. P. Diogo, J. Chem. Educ. **83**, 1389 (2006).

[98] S. Sykora, G. Ferrante, and A. Galkin, Poster 3rd Conf. Fast F. Cycl. NMR Relaxometry 10.3247/SL1Nmr03.002.

[99] G. Ferrante and S. Sykora, "Technical Aspects of Fast Field Cycling," (2006).

[100] J. R. Sangoro, A. Serghei, S. Naumov, P. Galvosas, J. Kärger, C. Wespe, F. Bordusa, and F. Kremer, Phys. Rev. E **77**, 051202 (2008).

[101] H. a. Every, A. G. Bishop, D. R. MacFarlane, G. Orädd, and M. Forsyth, J. Mater. Chem. **11**, 3031 (2001).

[102] T. Endo, M. Imanari, H. Seki, S. Sen, and K. Nishikawa, Solid State Ionics **259**, 41 (2014).

[103] S. Stapf, R. Kimmich, and R.-O. Seitter, Phys. Rev. Lett. **75**, 2855 (1995).

[104] S. Stapf, R. Kimmich, and R.-O. Seitter, Magn. Reson. Imaging **14**, 841 (1996).

[105] D. E. Freed, J. Chem. Phys. **126**, 174502 (2007).

[106] D. E. Freed, J. Phys. Chem. B **113**, 4293 (2009).

[107] T. Dutriez, M. Courtiade, D. Thiébaut, H. Dulot, F. Bertoncini, J. Vial, and M.-C. Hennion, J. Chromatogr. A **1216**, 2905 (2009).

[108] D. E. Freed, L. Burcaw, and Y.-Q. Song, Phys. Rev. Lett. **94**, 1 (2005).

[109] A. R. Mutina and M. D. Hürlimann, J. Phys. Chem. A **112**, 3291 (2008).

[110] L. Zielinski and M. D. Hürlimann, Energy & Fuels , 111013133953001 (2011).

[111] O. C. Mullins, H. Sabbah, J. Eyssautier, A. E. Pomerantz, L. Barré, a. B. Andrews, Y. Ruiz-Morales, F. Mostowfi, R. McFarlane, L. Goual, R. Lepkowicz, T. Cooper, J. Orbulescu, R. M. Leblanc, J. Edwards, and R. N. Zare, Energy & Fuels **26**, 3986 (2012).

[112] C. Jian, T. Tang, and S. Bhattacharjee, Energy & Fuels **27**, 2057 (2013).

[113] C. Jian, T. Tang, and S. Bhattacharjee, Energy & Fuels **28**, 3604 (2014).

[114] J.-P. Korb, A. Louis-Joseph, and L. Benamsili, J. Phys. Chem. B **117**, 7002 (2013).

[115] J.-P. Korb, New J. Phys. **13**, 035016 (2011).

[116] O. C. Mullins and E. Y. Sheu, eds., *Structures and Dynamics of Asphaltenes* (Springer US, Boston, MA, 1998).

[117] S. Niizuma, C. Steele, H. E. Gunning, and O. P. Strausz, Fuel **56**, 249 (1977).

[118] L. Zielinski, I. Saha, D. E. Freed, M. D. Hürlimann, and Y. Liu, Langmuir **26**, 5014 (2010).

[119] L. Barré, S. Simon, and T. Palermo, Langmuir **24**, 3709 (2008).

[120] S. Stapf, X. Ren, E. Talnishnikh, and B. Blümich, Magn. Reson. Imaging **23**, 383 (2005).

[121] S. Stapf, A. Ordikhani-Seyedlar, C. Mattea, R. Kausik, D. E. Freed, Y.-Q. Song, and M. D. Hürlimann, Microporous Mesoporous Mater. , 1387 (2014).

[122] A. Ordikhani-Seyedlar, O. Neudert, S. Stapf, C. Mattea, R. Kausik, D. E. Freed, Y.-Q. Song, and M. D. Hürlimann, Energy & Fuels , acs.energyfuels.6b00273 (2016).